Imaging the Crustal and Upper Mantle Structures of the Junggar Terrain in Northwestern China: Implications for Subduction-Collision-Accretion Processes in the Past

By

Shucheng Wu

A thesis submitted to Macquarie University

for the degree of Doctor of Philosophy

Department of Earth and Planetary Sciences

February 2019

MACQUARIE
University
SYDNEY·AUSTRALIA

Typeset in LaTeX 2_ε.

Dedication

I would like to dedicate this thesis to my beloved wife, Qingping Hu, who offered me with unconditional and endless love.

Acknowledgements

First and foremost, I would like to express my sincere gratitude to my supervisor Prof. Yingjie Yang, who has provided me with continuous support, valuable advice and constant encouragement in my three years' PhD project at Macquarie University. His preciseness and persistence in science has, both consciously and unconsciously, enlightened me and trained me from an immature rookie with plenty of impractical thoughts into a relatively 'mature' young seismologist. In the past three years, Yingjie has always made himself available to clarify my doubts and helped to break through all the obstacles I met in my research. More importantly, his rigorous and serious attitude towards science guided me on a right path in research and made him my best role model as a scientist and mentor. This spirit will continuously inspire me in my future academic career. As a non-native English speaker, I am also sincerely grateful for the assistance Yingjie provided me when writing up my first published academic article, preparing for all kinds of presentations, attending international conferences, and revising this PhD thesis. I could not have imagined having a better supervisor and mentor for my PhD study.

Also, I am truly thankful to Prof. Yixian Xu at Zhejiang University (formerly at China University of Geosciences (CUG), Wuhan) for the indispensable assistance in my PhD project. I always remember the first talk with him when I was an undergraduate student at CUG, he sparked my interest in seismology in that conversation and generously offered me an opportunity to be a postgraduate student in his geophysical group. The close collaboration of him and Yingjie then made my oversea PhD dream possible. Apart from that, he also gave me a valuable chance to participate in the seismic fieldwork in northwest China and kindly provided me with all the seismic data used in this thesis. Without his significant support, it would not be possible to conduct this research and complete this thesis.

Special thanks to my colleague and best friend Kai Wang for devoting valuable time in teaching me the body wave tomography technique from the very basics. His kindness and patient assistance in explaining the codes and revising the scripts really helped me out during the final year of my PhD project. I would also like to express my gratitude to Kai Wang, Jinxiang Huang, Guoliang Li, Shilin Li and Yuanyuan Hua for the important contribution and revision in some sections of this thesis. The academic supports they provided me not only improve this thesis greatly but also broaden my view in a wider aspect. Also, I greatly appreciate Chengxin Jiang, Zhen Guo, Kai Wang and Jun Xie for the helpful guidance both in my personal life and research during the early days of my PhD study.

I am truly fortunate to have Qing Xiong, Jinxiang Huang, Fei Wu, Siqi Zhang, Chunfei Chen, Jianggu Lu, Bo Xu and many other geologists/geochemists/geodynamists around me. All the discussions with them benefit me significantly and inspire me to consider scientific problems more comprehensively. Through the daily afternoon coffee time with Jinxiang Huang, Fei Wu and Siqi Zhang, I gained enormous knowledge of tectonics, geochemistry and geodynamics, which has made me realize the importance of collaboration across multiple disciplines. I sincerely appreciate all of them for sharing their time and knowledge with me.

I feel extremely lucky to be one of the members in the big geoscience family of the Department of Earth and Planetary Sciences (EPS), Macquarie University. All the weekend trips and dinners with these lovely friends, including Kai Wang, Shilin Li, Zhen Guo, Chengxin Jiang, Jun Xie, Guoliang Li, Jiayi Ai, Zhongxuan Li, Jun Xie, Ying Chen, Anqi Zhang, Qing Xiong, Jinxiang Huang, Fei Wu, Siqi Zhang, Chunfei Chen, Bo Xu, Huiyuan Xu, Thomas Connell, Alice van Tilburg and many others, have made my three years' PhD life enjoyable and delightful. The tight friendships we built in these years will never fade away. My gratitude also extends to my lovely roommates and friends Yachen Yuan, Yu Yang and Qingfeng Fang, who gave me generous help when I was fresh in Australia back in 2015.

Finally, I am deeply indebted to my family members, especially my parents and beloved wife Qingping Hu. Their unconditional love, constant support, and unhesitating sacrifices have encouraged me to overcome all the difficulties along the way and finally made me who I am right now. This thesis will be the best gift for all of you.

Shucheng Wu

November, 2018, Sydney, Australia.

Abstract

The Junggar terrain of northwestern China is an ideal place to study the complex subduction-collision-accretion processes in the Central Asian Orogenic Belts. Currently, the evolutionary history of the Junggar terrain is still under hot debate, especially the west Junggar region where multiple Paleozoic subduction systems are proposed to explain the tectonic evolution. Previous studies on the Junggar terrain are mostly based on geochemistry, geochronology and geomagnetism, a fine-scale velocity structure model of the Junggar terrain, which can provide vital constraints on the tectonic evolution, is still lacking.

In this thesis, by employing receiver function analysis, ambient noise tomography, two-plane surface wave tomography and teleseismic body wave finite-frequency tomography, I construct high-resolution 3D velocity models of the crust and upper mantle structure of the Junggar terrain using data from two seismic arrays deployed in the Junggar terrain. Because most of the subsurface features in the Junggar terrain are well-preserved since the late Paleozoic, our models help to unveil past tectonic processes in the Junggar region. From the receiver function analysis, I find that significant Moho variations are observed across the study region and a pronounced Moho offset is imaged between the Zaire mountains and the western Junggar basin. From the seismic tomographic models, I image a pronounced high velocity anomaly beneath the Junggar basin at the middle/lower crust and the uppermost mantle. This high velocity body slightly dips northwestward under the west Junggar to ~150 km depth, then appears at ~400 km depth. This high velocity anomaly in the middle/lower crust and uppermost mantle is interpreted as the remnant of fossil subduction slabs by examining its speed and temperature, while the high velocity near the mantle transition zone beneath the west Junggar is considered as either the detached slab or part of the mantle convection system in the Junggar region. Based on these interpretations, I propose a failed northwestward

subduction model with the fossil oceanic lithosphere still trapped beneath the Junggar basin and the western part of Junggar to explain the latest tectonic activities in the west Junggar.

The identification of the fossil slab in the Junggar region is significant because most ancient oceanic slabs in continental collision zones are not well preserved. The fossil slab in the Junggar region not only gives important clues on the evolutionary processes in this region but also provides a nature laboratory to study the ancient subduction systems through the Earth's history.

Contents

List of Figures

List of Tables

List of Publications

- Wu, S., Huang, R., Xu, Y., Yang, Y., Jiang, X., & Zhu, L. *Seismological Evidence for a Remnant Oceanic Slab in the Western Junggar, Northwest China*. Journal of Geophysical Research: Solid Earth, **123**, 4157-4170 (2018).

  Thesis Author Contribution: Concept (70%); Data Collection (100%); Analysis (60%); Writing (80%).

- Wu, S., Yang, Y., Xu, Y., & Zhu, L. *Tracing the Fossil Subduction Slab at uppermost mantle in the Junggar Region, Northwest China*. (to be submitted)

  Thesis Author Contribution: Concept (100%); Data Collection (100%); Analysis (100%); Writing (95%).

- Wu, S., Yang, Y., Wang, K., & Xu, Y. *Mantle Shear Wave Velocity Structure in Junggar Region Revealed by Body-wave Finite-frequency Tomography: Implications for its Mantle Dynamics*. (in preparation for journal submission)

  Thesis Author Contribution: Concept (90%); Data Collection (100%); Analysis (100%); Writing (100%).

Papers not included in this thesis:

- Wu S., Yang, Y. *Refined crustal and upper mantle structures from Ambient Noise Tomography and Two-plane Surface Wave Tomography in Western Tien Shan: Implications in Orogenic mechanisms*. (in preparation for journal submission)

- Wang A., Luo Y., Wu S., Shen C., Jiang X., Xu Y. *Source Analysis of Seismic Ambient Noise in the Western Junggar area*. Chinese Journal of Geophysics, **60(4)**, 1376-1388 (2017).

1

Introduction

1.1 Research background

Orogenic belts are widely distributed on Earth and closely related to dynamic processes such as subduction, collision, metamorphism and magmatism. Unlike the classic orogenic model where continent-continent collisions take place at the termination of a Wilson cycle, accretionary orogens are usually formed at plate margins side by side with the on-going subduction of an oceanic lithosphere [Cawood et al., 2009]. The modern representatives of accretionary orogens are found along the Pacific boundaries [e.g. Hall, 2009, Isozaki, 1996, Isozaki et al., 2010, Saleeby, 1983], while ancient examples are represented by the Central Asian Orogenic Belt (CAOB; or the Altaids tectonic collage) and the Lachlan orogen of eastern Australia [e.g. Cawood et al., 2011, Windley et al., 2007, Xiao et al., 2015b]. These accretionary processes are one of the most significant mechanisms contribute to the continental growth throughout Earth's history. Meanwhile, they have extensive mineral deposits providing indispensable resources for human beings. In the past decades, numerous

studies have been carried out in these orogens to understand their initiation, formation and evolution [e.g. Cawood et al., 2009, Glen, 2013, Glen et al., 2009, Jahn, 2010, Kemp et al., 2009, Wang et al., 2006, Xiao et al., 2010, 2015b]. However, some of the detailed geodynamics such as the duration and orogenic architectures are still poorly constrained due to the lack of a continuous geological record and high-resolution geophysical model. Therefore, building a systematic high-resolution architectural model of the accretionary orogen is vital to constrain the continental growth modes, benefit the economic minerals exploration, and more importantly, reconstruct global tectonics.

Seismic tomography is one of the most effective methods in modern seismology to produce the subsurface velocity structure images. With the concepts emerging from the late 1970s, seismic tomography techniques have shown great advantages in mapping the Earth's internal structures and analyzing the relevant dynamics from global to regional scales [e.g. Aki et al., 1977, Bijwaard et al., 1998, Lanz et al., 1998, Levander et al., 2011, Saygin and Kennett, 2010, van der Hilst et al., 1997, Yamanaka and Kikuchi, 2004, Yang et al., 2007, Yao et al., 2006, Zhang and Toksöz, 1998, Zhao, 2004]. Benefitting from the emergence of large-sale and dense seismic networks and the advancement of high performance computation in recent years, high-resolution 3D velocity models have been built and helped solve various tectonic puzzles. Besides, different types of seismic signals including surface waves, body waves and free oscillations are involved to provide a complementary model of the Earth's interior. In this thesis, by applying different tomographic techniques (including surface wave and body wave traveltime tomography) to two seismic arrays recently deployed in the Junggar terrain, northwestern China (Figure 1.1b), I construct fine-scale crustal and mantle velocity models to investigate the tectonics and orogenic mechanisms in this region.

1.2 General geology and tectonics

1.2.1 An overview of CAOB

The CAOB is one of the largest and longest-lived accretionary orogens in the planet across the central and eastern Asia (Figure 1.1a). As a fully completed accretionary orogen evolved from at least 1Ga to the late Paleozoic [Jahn, 2000, Kröner et al., 2008, Şengör et al., 1993], the CAOB exhibits an extremely complex composition of different accretionary orogens,

Precambrian microcontinents, Neoproterozoic to Permian accretionary complexes and magmatic arcs [Choulet et al., 2016]. The relatively long evolutionary history of the accretionary orogenesis has contributed a large amount of continental growth from the Neoproterozoic to the Phanerozoic. Therefore, it is vital to unfold the complex evolutionary history and understand the orogenic dynamics in the past.

The accretionary growth mechanism, dynamics and the termination time of CAOB are still hotly debated and numerous models have been invoked to explain the puzzle of tectonics in CAOB. These models can be basically divided into two main groups: (1) single long-lived subduction system with the bending and slicing of the Kipchak arc [Şengör et al., 1993]; (2) multiple subduction systems with the amalgamation and accretion of several microcontinents and/or terrains [Kröner et al., 2007, Windley et al., 2007]. Despite these models can explain some common geological observations, these models still have not reached the consensuses about the initial and termination time of the subductions (single or multiple), the relationship between subductions and oroclinal bending, the detailed geometry of subductions and their polarity, and how the orogenic belt develops into its current position.

Geologically, the CAOB can be divided into the eastern and western part [Şengör and Natal'In, 1996, Şengör et al., 1993], the eastern part is developed by the convergence of the Siberian craton, the North China craton and the Mongolia block during the early Mesozoic; whereas the western part is formed by the convergence of the eastern European craton, the Siberian craton and the Tarim craton from the late Proterozoic to the late Paleozoic - early Mesozoic [Xiao et al., 2010]. This thesis focusses on the Junggar terrain (Figure 1.1b,c), which is a representative area to understand the tectonics evolution of western CAOB [Choulet et al., 2012, Windley et al., 2007, Xiao et al., 2015b].

1.2.2 Outlines of Junggar geology and tectonics

The Junggar terrain in northwestern China is regarded as an ideal place to study the CAOB because the exposures of geological characteristics such as ophiolites, intrusions, accretion wedges, etc., and the well-preserved Paleozoic subsurface structures (Figure 1.1b) [Ma et al., 2012, Wu et al., 2018, Xiao et al., 2008, 2015a, Xu et al., 2016, Zhang et al., 2011b]. Situated at the southern margin of the West CAOB, the Junggar terrain is surrounded by the Kazakh terrain (or block) to the west, the Altay (or Altai) mountains to the north and the Tien Shan to the south (Figure 1.1b). The present-day Junggar terrain is a complex tectonic assembly of

Mesozoic-Cenozoic sedimentary basins and the surrounding Paleozoic orogens filled with a variety of granitic rocks, ophiolitic belts and accretion complex.

The Junggar terrain is characterized by a triangle-shaped Junggar basin (~134,000 km^2) in the center with a thick sedimentary cover on top of the basement. The thickness of sediment varies significantly across the basin from ~5 km in the northern part and ~10 km or ever greater in the southern margins based on seismic reflection studies [Li et al., 2016, Zhao et al., 2003]. The Junggar basin is documented as an upper Paleozoic, Mesozoic and Cenozoic superimposed basin [Cao et al., 2012] with the oldest sedimentary rocks of the Carboniferous [XBGMR, 1993]. The nature of Junggar basin basement is a controversial topic since there is no exposure of basement rocks in or around the basin. However, it is crucial to determine the basement property as it plays an important role in rebuilding the tectonic evolutionary history in the whole Junggar terrain. Earlier researches regard the basement of Junggar basin as a small Precambrian continental block [Watson et al., 1987, Zhang et al., 1984] which evolved together with the complex orogenesis in the CAOB, forming the current tectonic mosaic of Junggar terrain, whilst more recent work base on borehole data suggests that the Junggar basin may be underlain by Paleozoic oceanic crust fragments [Zheng et al., 2007]. The borehole data shown by Zheng et al. [2007] reveal that basaltic rocks are present within the basement, maybe representing a trapped Paleozoic oceanic crust and/or the silicic rocks produced by melting of the Paleo-oceanic crustal rocks [Zheng et al., 2007]. Based on this understanding, evolutionary models are proposed suggesting the complicated arc and accretion systems developed at all the edges of Junggar basin. The trapped Junggar Ocean, which developed into the present-day Junggar basin, escaped from the normal extinction fate and was preserved as the result of the unique amalgamation of the CAOB [Xiao et al., 2008, Xiao and Santosh, 2014]. The locations of the borehole data are only limited to a few local areas, rendering them not able to sample the whole spatial distribution of the trapped ancient oceanic crust. However, other studies argue that several arc-basin systems are recognized beneath the Junggar basin and the present basement is probably composed of juvenile continental crust [He et al., 2013, Li et al., 2016, Yang et al., 2012c]. The last two interpretations both point out an intricate subduction-accretion system in the Junggar terrain with many details undetermined.

Mountains surrounding the Junggar basin are the nearly EW trending Altay mountain belt in the north, the Chinese northern Tien Shan (NTS) in the south, and a small mountain range

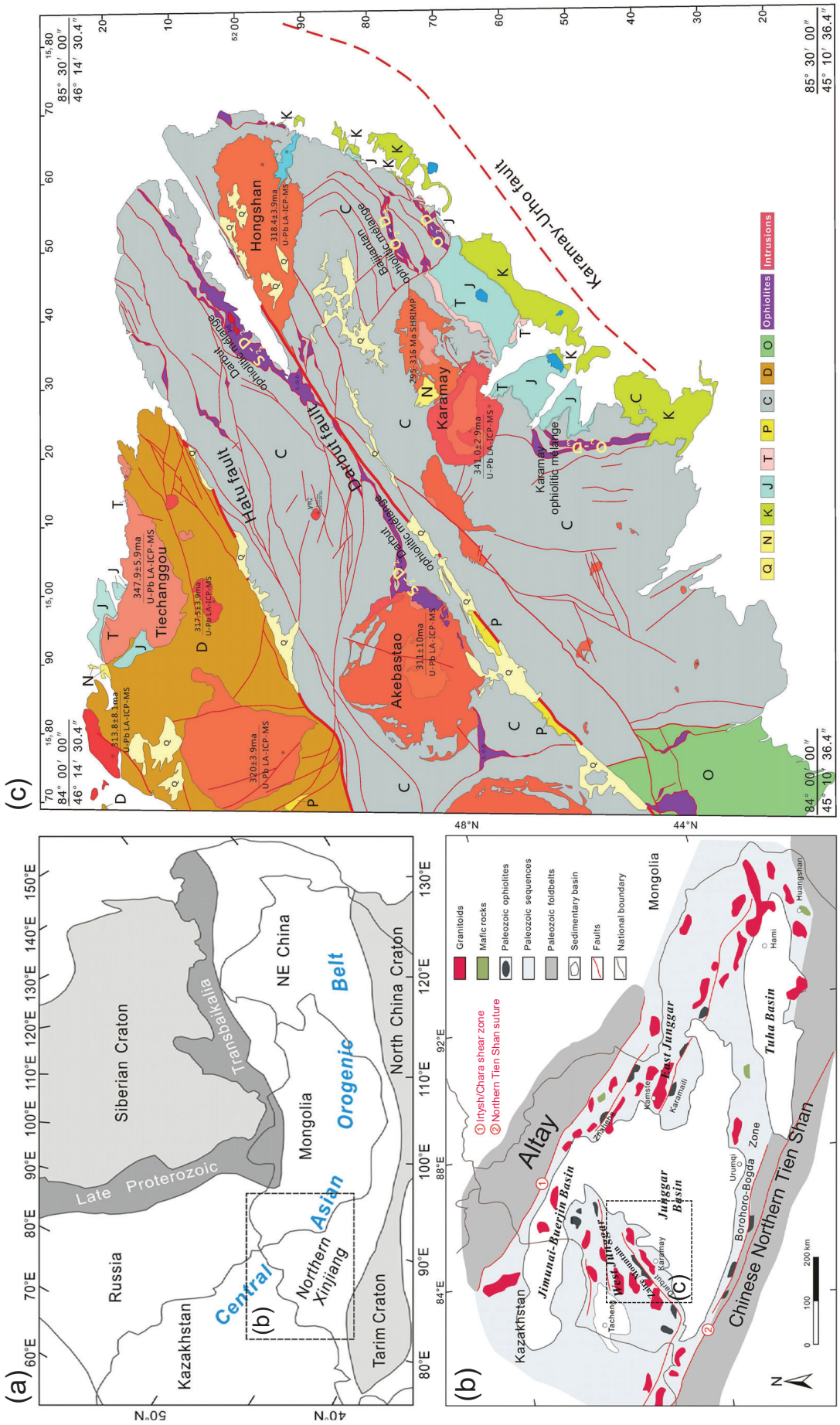

FIGURE 1.1: (a) The location of Junggar terrain and its relationship with CAOB, modified after Jahn [2000], Windley et al. [2007]. (b) Simplified geological map of the Junggar terrain, modified after Chen and Jahn [2004], Li et al. [2016]. (c) Detailed geological map of western Junggar region.

called the Zaire mountain (western Junggar) in the west (Figure 1.1b). The Altay in the north is composed of sedimentary series, ophiolitic belts, volcanic rocks and variably deformed metamorphic rocks. Continuous subduction related magmatism is observed from the Early to Middle Paleozoic based on the Zircon U-Pb age of the granitoids and metamorphic rocks [Cai et al., 2011, 2012, Sun et al., 2008, Yuan et al., 2007]. The southern NTS is believed to experience a two-stage uplifting: the first took place during the Paleozoic resulting from the amalgamation of several neighboring terranes [Allen et al., 1993, Gao et al., 1998, Glorie et al., 2010], and then in the late Cenozoic it was remotely reactivated by the collision between Indian and Eurasian Plate [Coleman, 1989, Dumitru et al., 2001, Jolivet et al., 2010]. The rejuvenation of NTS also causes the quick subsidence of the Junggar and Tarim basins, resulting in the thick sedimentary layer in these basins [Gao et al., 2013, Jiang et al., 2013]. The Zaire mountain of western Junggar (WJ, figure 1.1c) is one of the most attractive areas to study the Late Paleozoic evolution since the intriguing exposure of granitoids and ophiolitic mélanges. This region is characterized by Paleozoic ophiolitic belts and volcanic rocks cut by three large-scale NE-striking faults, the Darbut Fault, the Hatu Fault, and the Karamay-Urho Fault. The Darbut Fault, along which an ophiolitic mélange zone is cropped-out and many valuable Cu-Au-bearing ore deposits are discovered, is located at the central part of the region with more than 100 km length. The Karamay-Urho Fault is a hidden fault which separates the Junggar basin and the Zaire mountain and the Hatu Fault is a compress-shear fault located in the most northwest.

Extensive subduction related magmatism occurred in the Junggar terrain during the Paleozoic [Cai et al., 2011, 2012, Sun et al., 2008, Yuan et al., 2007], forming the complex magmatic suites comprise I- and A-type granitoids, mafic dykes and volcanic rocks [Li et al., 2015, Tang et al., 2012a,b, Yin et al., 2013]. Most of the intrusions are emplaced between ~320 Ma to ~250 Ma [Chen and Arakawa, 2005, Chen and Jahn, 2004, Geng et al., 2009, Han et al., 2006, Yin et al., 2010].

In addition, widespread ophiolitic mélanges outcropped in the mountains surrounding the basin mostly parallel to the trending of these mountains [Charvet et al., 2007, Xiao et al., 2008], aging from over 500 Ma to 300 Ma [Buslov et al., 2001, Feng et al., 1989, Xu et al., 2006, Yang et al., 2012b, Zheng et al., 2007]. The western Junggar region is characterized by three main ophiolitic mélanges emplaced in the surrounding Carboniferous strata. They are the nearly NE trending Darbut, Baijiantan ophiolitic mélanges and the NS trending Karamay

ophiolitic mélange (Figure 1.1c). The Darbut ophiolitic mélange is mostly distributed in the northern part of the Darbut Fault and stretching along the fault with ~105 km long and < 5 km wide. From the gabbro samples in the Darbut mélange, a Sm-Nd isochron age of 395±12 Ma [Zhang and Huang, 1992] and a zircon U-Pb age of 391±6 Ma [Gu et al., 2009] is obtained. The Baijiantan ophiolitic mélange is a smaller mélange zone situated in the southeast of the Darbut ophiolitic mélange, ranging from 0.5 to 2 km in width. Two sets of SHRIMP zircon U-Pb ages of 332±14 Ma and 414±9 Ma are obtained from the gabbros in the Baijiantan mélange [Xu et al., 2006]. The Karamay ophiolitic mélange is recently identified ophiolite, located in the west of the Baijiantan ophiolitic mélange. It is composed of pillow structured basalts, siliceous rocks with radiolarians, serpentinites and dunites [Xiang et al., 2013, Xu et al., 2006]. The complex distribution of these ophiolitic mélanges, intrusions and the accretion feature again indicates an intriguing subduction-collision-accretion history in this region.

Although numerous studies have been carried out on the formation and evolution of the Junggar terrain, it is still not clear about the subduction modes around the Junggar terrain, particularly for the western Junggar (WJ). Based on the different interpretations of the ophiolitic mélange, contradictive models are proposed to account for the late Paleozoic subduction modes in WJ and can be mostly classified into the following four groups:

(1) A single developed subduction system [Wang et al., 2003]. This model is built upon geochemical data of mafic rocks in ophiolitic mélanges. Wang et al. [2003] suggests the subductions around present-day Junggar basin is part of the Kipchak arc that is responsible for the formation of the entire CAOB [Şengör et al., 1993]. The following rotation and faulting during the Permian changed the geometry of units to its current location. However, by only using the geochemical data of mélanges, the evolution history could be biased. In addition, this evolutionary model is inconsistent with the paleomagnetic data [Xiao et al., 2015b].

(2) A two-way subduction [Yang et al., 2012a] model based on geochronological and geochemical data of gabbro and basalt rocks embedded in the ophiolitic complex. This model emphasizes that the Darbut ophiolitic complex is developed from a back-arc basin and two opposite subductions beneath WJ in the late Carboniferous. Major drawbacks of this model are that this model is in conflict with the different ages of the ophiolitic complex distributed in two sides of the Darbut fault, and the relatively

shallow depth of Darbut fault reveled by geophysical data [Xu et al., 2016].

(3) Multiple subduction systems proposed by Xiao et al. [2010] based on multi-discipline study. By integrating geochemical, geochronological and geomagnetic data, this model is considered as the most integrated model for the forming of present-day Junggar terrain. In this model, multiple separated subductions occurred within the Paleo-Asian ocean and WJ is considered as an intra-oceanic arc.

(4) A ridge-related subduction model with either one-way or two-way subduction [Geng et al., 2009, Jiang et al., 2010, Ma et al., 2012, Tang et al., 2012b, Zhang et al., 2011b]. The ridge subduction scenario is hotly discussed since the observation of adakitic intrusions in WJ. Within the ridge subduction framework, numerous models are proposed with different subduction polarity and geometry due to the contradictory interpretation of the ophiolitic mélanges.

The subduction polarity and the orogenic processes in western Junggar are still under hot debate to date, which can be (partly) resolved by geophysical imaging in this region, of a particular the fine-scale 3D seismic model of deep structures.

1.3 Surface wave tomography

Surface waves are the most pronounced signals with the largest amplitude and arrive later than body waves in seismograms. According to the particle motion directions, surface waves can be subdivided into two different types, i.e. Rayleigh and Love waves. Rayleigh waves are generated by the interaction between compressional wave (*P*-wave) and vertically polarized shear waves (*SV*), while Love waves emerge as the result of the interference among the horizontally polarized shear waves (*SH*). Both of them are trapped at the shallow depths of Earth. Surface waves are dispersive with different frequency surface waves sensitive to subsurface seismic structures at different depths, inspiring semiologists to exploit surface waves for imaging Earth's interior structures.

Earlier tomographic works based on surface waves emerged from 1980s. Global upper mantle velocity structures and anisotropies are imaged by utilizing surface waves emitted by earthquakes [Nakanishi and Anderson, 1982, 1983, Nataf et al., 1984, 1986, Tanimoto and Anderson, 1984]. These early studies on surface wave tomography all assume that the surface

waves travel along great-circle paths connecting sources and receivers. By measuring the phase and/or group velocities of a large number of surface waves propagating along different paths, lateral heterogeneities can be sampled and recovered. The successfully recovering of the major velocity anomalies from surface wave tomography globally leads seismologists to pay great attentions to surface waves and then the surface wave tomography gradually develops into a standard method in seismology.

In the past decades, with an explosive growth in the number of seismic stations and the improved instrument sensitivity for broader-band signals, a rapid progress can be achieved in imaging subsurface structures worldwide with a high resolution. Typically, when dealing with global crustal and mantle structures, teleseismic recordings with surface wave periods ranging from 30 s to 300 s are utilized. In this case, detailed crustal structures are neglected and the crust is then modelled as a homogeneous layer. For regional and local imaging problems, local earthquakes are utilized to get surface waves at periods from a few second to a few tens of second. These short-period surface waves provide information about the crustal and uppermost mantle structures. However, an issue in these tomography techniques is that these tomography studies have to rely on the surface wave data from earthquakes.

Using surface wave signals directly emitted by seismic events in surface wave tomography face several problems, such as the off-great-circle propagating effect and errors related to sources (location, timing and mechanism). Therefore, progresses in measuring phase velocity differences within a regional array or between two stations (or the two-station approach) are made and widely applied in regional surface wave tomography studies [Yao et al., 2008, 2006, 2005]. The two-station approach has its advantage in overcoming biases introduced by source uncertainties, and only requires a pair of two stations and a source align with a common great-circle path. This requirement, however, greatly limits the number of ray paths in a seismic array. In addition, this approach regards the incoming surface wave traveling along a great circle path. In fact, great distortions are inevitable when surface waves propagate through heterogeneities along their paths and result in a deviation off the great circle paths [Alsina et al., 1993, Laske, 1995]. Scattering and multipathing effects also contribute to the distortions [Capon, 1970, Snieder and Nolet, 1987, Wielandt, 1993]. In order to address these issues, Forsyth and Li [2005] developed a two-plane wave surface wave tomography solution (TPWT), in which an incoming surface wave is modelled by two interfering plane waves (the primary and secondary wave) with unknown amplitudes, initial phases and propagation

directions. This approach successfully avoids the non-planar effects and can generate more reliable subsurface structures. Later in 2006, Yang and Forsyth [2006b] implanted 2D surface wave sensitivity kernels [Zhou et al., 2004] into the TPWT framework to account for finite-frequency effects of surface waves.

Numerous studies were conducted ever since TPWT technique was developed. For example, Wagner et al. [2010] imaged the velocity structure of the northwestern United States; Wang et al. [2013] observed the attached fossil Farallon plate in north America; Bell et al. [2016] imaged the upper mantle structures beneath the Juan de Fuca plate; Guo et al. [2016b] applies the TPWT to the northeast China and Tibet, and many other studies based on this tomographic method [e.g. Li and Burke, 2006, Moschetti et al., 2010, Palomeras et al., 2014, Villagómez et al., 2007, Wang et al., 2009, Yang and Forsyth, 2006a].

Although the TPWT approach is widely adopted to produce regional velocity models around the world, one major limitation is that this method relies on surface waves at periods longer than 20/30 s. Therefore, crustal structures are not constrained well by the TPWT technique. To overcome this limitation, ambient noise tomography technique (ANT) is introduced and shows its revolutionary power in retrieving shorter periods surface wave signals.

Comparing with the traditional methods that extract dispersion curves from the earthquake surface waves, ANT has several obvious advantages. First, the traditional surface wave tomography using earthquakes are generally based on the assumption that the traveltime difference of two stations from one earthquake is all attributed to the receiver side and neglect the influence of the source and the travel path. The ambient noise cross-correlation only contains the information of the media between two stations, easily eliminating the influence of inaccurate source properties such as the location and moment tensor. Second, the ray path coverage of ANT is highly related to the seismic array deployed, which neglects the unevenly distributed earthquakes and suitable for aseismic region. Last and most importantly, the ability to obtain shorter periods surface wave dispersions turns ANT into a vital complement to the conventional teleseismic-based surface wave tomography and provides precise shallower structures.

The idea of ANT dates back fifty years ago. But until the 2001, the ultrasonic laboratory study of Weaver and Lobkis [2001] confirmed that the Green's function between two receivers can be extracted from the cross-correlation of noise recorded by these two receivers. During

the same time, theoretical studies are well-established [e.g. Derode et al., 2003a,b, Lobkis and Weaver, 2001, Roux et al., 2005, Snieder, 2004, Weaver and Lobkis, 2004, 2006] and the cross-correlation idea is then introduced to seismology by Campillo and Paul [2003]. By cross-correlating the coda waves, Campillo and Paul [2003] successfully extract fundamental Rayleigh and Love waves between stations in the Mexican National Seismological Network. Furthermore, Sabra et al. [2005a,b] obtained dispersion curves from the cross-correlations and constructed surface wave velocity maps at a frequency range of 0.1-0.2 Hz in the Southern California. Since then, ambient noise tomography has become a well-established method for investigating the subsurface velocity structures [e.g. Li et al., 2009, Lin et al., 2008, Moschetti et al., 2007, Yang et al., 2007, Zheng et al., 2008].

To broaden the surface wave period band, the ANT and teleseismic surface wave tomography technique can be combined to generate dispersions from shorter period (< 10 s) to long period (> 100 s). Then, a high-resolution crustal and upper mantle shear wave velocity model can be constructed through inverting these dispersion measurements. In the past few years, numerous studies can be found based on this passive-active-combined imaging approach [e.g. Ceylan et al., 2012, Fu et al., 2015, Guo et al., 2016b, Li et al., 2018, Ouyang et al., 2014, Shan et al., 2017, Yang et al., 2011a].

1.4 Body wave traveltime tomography

The origin of body wave traveltime tomography is usually attributed to Keiiti Aki, who published a seminar paper of the first seismic tomography in 1976 on inferring 3D seismic velocity structure beneath California based on local earthquakes [Aki and Lee, 1976]. In his paper, the crustal structure was designed as a series of rectangular blocks, each of which is then parameterized by P wave slowness perturbation. A set of linear equations for the observed first P wave arrival times collected at 60 stations from 32 local earthquakes were formulated in terms of the source and medium parameters. The source parameters for all the earthquakes and the medium parameters for all the blocks were then determined simultaneously by a damped least squares method. In 1977, this publication was followed by an equally influential paper which introduces the teleseismic tomography method to seismologists [Aki et al., 1977]. Traveltime residuals of teleseismic events were used to determine the 3D seismic velocity perturbations beneath the Norwegian Seismic Array in southeast Norway [Aki et al., 1977].

These early works of Aki undoubtedly promoted the development of the modern seismology.

Blocks with uniform seismic properties (e.g. velocity or slowness) are the most basic for tomographic parameterization, which makes the ray tracing straightforward since the ray path segments in each block are represented by straight lines. However, the artificial discontinuities between each block are unrealistic, which can lead to unwarranted ray shadow zones and triplications [Rawlinson et al., 2010]. Meanwhile, a different model parameterization method was used in the global tomography at around the same time by Dziewonski et al. [1977]. In order to determine the velocity structure of the Earth's mantle, a spherical harmonic parameterization method was used to invert a large set of P wave travel residuals collected from the Bulletin of the International Seismological Centre (ISC bulletin) [Dziewonski et al., 1977]. Then, Thurber [1983] applied trilinear interpolation between a rectangular grid of nodes to define a continuously varying velocity field for local earthquakes tomography. However, both the blocks and the spherical harmonic parameterization methods can not deal with models with velocity discontinuities. To solve this problem, Zhao et al. [1992] developed an efficient three-dimensional ray tracing algorithm based on the pseudo-bending technique [Um and Thurber, 1987] and Snell's law. This method can be used to a general velocity structure with a number of complexly shaped velocity discontinuities and with three-dimensional variations in the velocity in the model space.

Traditional body wave traveltime tomography is usually based on the Fermat's principle and ray theory, which is relatively simple with a high frequency approximation without considering the finite frequency effects in broadband traveltime data analysis. To account for the off-ray sensitivity, two types of finite-frequency tomography methods were proposed, i.e. the 'fat ray' [Husen and Kissling, 2001] and the 'banana doughnut theory' [Dahlen et al., 2000, Marquering et al., 1999]. In the fat ray tomography provided by Husen and Kissling [2001], the entire first Fresnel volume of the first arriving phase is considered in relating traveltime residuals to model perturbations. Therefore, the region of the model sensitive to a given datum is banana shaped for a typically curved path, with the source and receiver close to the tips of the 'banana'. In the banana doughnut theory [Dahlen et al., 2000, Marquering et al., 1999], 3D sensitivity kernels of body wave phases are hollow banana shaped with zero sensitivities along the centre ray, and are doughnut shaped in a cross section that perpendicular to the ray. The finite frequency tomography is usually used to account for scattering or diffraction effects including wave front healing [Dahlen et al., 2000, Rawlinson

et al., 2010].

The degree of improvement finite-frequency tomography brought to traditional ray theory tomography is hotly debated and has been discussed by many researchers [e.g. Dahlen and Nolet, 2005, De Hoop and van Der Hilst, 2005, Tong et al., 2011, Trampert and Spetzler, 2006]. Nevertheless, With the development and the use of finite-frequency tomography, this method has been proved to be useful and important [e.g. Hung et al., 2010, 2004, Kolstrup et al., 2015, Montelli et al., 2004, Obrebski et al., 2010, Yang et al., 2006]. Relative to the traditional ray theory, the finite-frequency tomography can use a larger range of phase information with different frequency bands to constrain the subsurface velocity structure.

1.5 Thesis objectives

As a key part of the CAOB, the formation history of the Junggar Terrain is still not fully understood. As summarized in section 1.2.2, contradictive Paleo-subduction models have been proposed to explain the formation of WJ. In order to discriminate among the competing models, high-resolution crustal and upper mantle velocity models are the key as the velocity structures inherit the imprints of past tectonic actives. However, the high-resolution subsurface 3D velocity structures of Junggar terrain has never been imaged before. Therefore, the main goal of this thesis is to build a high-resolution tomographic velocity model of the Junggar terrain, aiming to gain a better knowledge of the relevant tectonics and dynamics. Specifically, the objectives of this thesis are listed below.

1. Construct a high-resolution crustal isotropic *Vs* model based on a small seismic array deployed in western Junggar region. By incorporating the Moho information from receiver function studies and the velocity structure from ANT, I aim to a) examine the remaining features left over by past tectonic events and understand the complex subduction-collision-accretion history of this region, b) estimate the crustal composition through the velocity model.

2. Build a detail crustal and upper mantle isotropic *Vs* model across the entire Junggar terrain by deploying a larger seismic array. Such model will help to understand the deeper structures and its relationship with dynamic processes and examine possible structure differences between different units in Junggar terrain.

3. Generate a whole upper mantle *Vs* model using teleseismic *S* wave traveltimes based on finite-frequency tomography in order to investigate if there are any velocity features in deep upper mantle related to the past subduction system.

4. Build a comprehensive *Vs* model from surface down to the mantle transition zone combining results from the above tomographic studies, aiming to have a clear view of tectonic formation and evolution of the Junggar terrain.

1.6 Thesis structure

This thesis contains six chapters, the contents in each chapter are summarized below:

In chapter 1 (this chapter), an introduction is given, including the research background, general geology and tectonics, a review of previous evolutionary models in the study region, and the tomography techniques used in this thesis together with their history, advantage and application.

In chapter 2, a brief introduction to the method and theory is illustrated. Some key principles and aspects about TPWT, ANT and body wave finite-frequency tomography are discussed.

In chapter 3 (published in *Journal of Geophysical Research: Solid Earth* as Wu et al. 2018), I construct a 3D crustal *S*-wave velocity model in western Junggar region using ANT based on 31 portable broadband seismic stations from September 2013 to December 2013. The Moho depth is also determined by a H-κ method and a common-conversion-point (CCP) stacking method. I examine the high velocity body in the mid-lower crust and compare it with the calculated *S*-wave speed of various metamorphic facies of Mid-Ocean Ridge Basalt (MORB) under an appropriate Pressure/Temperature condition. The origin of the high velocity body and its implications for the dynamic process in the western Junggar is discussed.

In chapter 4 (in preparation for journal submission), a regional seismic array consisting 49 stations were deployed across the entire Junggar terrain. Using the new data, I construct a 3D *S*-wave velocity model of the crust and upper mantle by combining ANT and TPWT techniques. A wide spread high velocity zone is observed beneath the Junggar basin, which extends into the eastern part of the WJ. The temperature of uppermost mantle in this region is also inverted and compared with the predicted temperatures from a half cooling model.

The nature of this high velocity body and its relationship with surrounding tectonic units are discussed.

In chapter 5 (in preparation for journal submission), I adopt the teleseismic body wave finite-frequency tomography based on the same dataset in chapter 4 to construct the *S*-wave velocity structure of the upper mantle down to the depth of 500 km and then discuss our model in conjunction with the results of chapter 4. Our comprehensive velocity model in the Junggar terrain from the crust to mantle transition zone provides some new insights on the past tectonic processes.

Chapter 6 draws a conclusion of this thesis. The major discoveries are listed. In addition, a future research plan is outlined in the end of this chapter.

2

Methodology and Theory

2.1 Two-plane surface wave tomography

2.1.1 Modelling an incoming wave

In the Two-plane surface wave tomography (TPWT) framework, each incoming teleseismic surface wave is modelled as the interference between two plane waves (the primary and secondary wave), and the vertical displacement of the incoming wave v_z is represented by [Forsyth and Li, 2005]:

$$v_z(\omega) = A_1(\omega)\exp\left[-i(\mathbf{k_1}\bullet\mathbf{x} - \omega t)\right] + A_2(\omega)\exp\left[-i(\mathbf{k_2}\bullet\mathbf{x} - \omega t)\right], \tag{2.1}$$

where ω is the frequency, A_1 and A_2 are the amplitudes, $\mathbf{k_1}$ and $\mathbf{k_2}$ represent the horizontal wavenumber of the two modelled incoming waves, and $\mathbf{x}$ is the position vector. To simplify and better define the coordinate system, the position of a station is defined relative to a reference station in the array. In addition, for a single event, a common reference origin time is used for all the stations in the array. Therefore, for a given ith teleseismic event, function

2.1 can be simplified as:

$$ {}_i^k v_z = {}_iA_1 \exp[-i({}_i^k \phi_1)] + {}_iA_2 \exp[-i({}_i^k \phi_2)], \tag{2.2} $$

where ${}_i^k v_z$ is the vertical displacement for kth station at each single frequency, ${}_i^k \phi_1$ and ${}_i^k \phi_2$ are the phase of the modelled primary and secondary wave. The mathematical expression of these phases are:

$$ {}_i^k \phi_1 = {}_i^0 \phi_n + \overline{{}_i^k S} \omega \{ {}_i^k r \cos({}_i^k \psi - {}_i \vartheta_n) - {}_i^k \mathrm{x} \} + \omega({}_i^k \tau - {}_i^0 \tau), n = 1, 2 \tag{2.3} $$

where ${}_i^0 \phi_n$ denotes the phase at the reference station. ${}_i^k \tau$ represents the traveltime difference between the edge of the study region and the kth station, while ${}_i^0 \tau$ is the difference between the edge and the reference station. Here, ${}_i \vartheta_n$ is used to represent the direction of the two incoming wave, more specifically, represent the angular deviation from the great circle path. The $\overline{{}_i^k S}$ is the average slowness at kth station for ith event. In this equation, (r, ϑ) are the polar coordinate system centered at the reference station, and used to define the location of the kth station.

Traveltime difference ${}_i^k \tau$ in the function 2.3 is defined as the integration of the slowness between the edge of the study region and the kth station, mathematically:

$$ {}_i^k \tau = \int_{{}_i^{edge} x}^{{}_i^k x} {}_i S dx, \tag{2.4} $$

The averaged slowness $\overline{{}_i^k S}$ is calculated by:

$$ \overline{{}_i^k S} = \frac{1}{2} [{}_i^k \tau / ({}_i^k \mathrm{x} - {}_i^{edge} \mathrm{x}) + {}_i^0 \tau / ({}_i^0 \mathrm{x} - {}_i^{edge} \mathrm{x})], \tag{2.5} $$

To generate a 2D continuous velocity or slowness map, a Gaussian weighting scheme is introduced. Therefore, every point on the 2D map is weighted by the Gaussian weighting factor defined as:

$$ w_j = \exp\left[- \frac{(x - x_j)^2 + (y - y_j)^2}{L_w} \right], \tag{2.6} $$

where (x_j, y_j) is the location of jth grid node within the study region, L_w is the smoothing scale for the 2D map. Generally, decreasing L_w will result in an increase in the data fitting (i.e. smaller misfit) and bringing in more small-scale variances. However, it may introduce some unrealistic and artificial short-wavelength features in the resulting 2D variation maps. Therefore, the smoothing length L_w should be carefully chosen by balancing the tradeoff between resolution and model variance in any particular tomographic studies.

2.1.2 2D sensitivity kernels

The conventional ray theory based surface wave tomography can only retrieve anomalies with scales comparable or larger than the wavelength and the Fresnel zone [Lee and Nolet, 1997, Trampert and Woodhouse, 1995, Woodhouse and Dziewonski, 1984]. In order to resolve anomalies with scale smaller than the wavelength in regional tomographic problems, surface wave finite-frequency effects cannot be ignored [Yang and Forsyth, 2006b]. 3D surface wave sensitivity kernels are well-established by Zhou et al. [2004] based on the Born approximation. Surface wave phase or amplitude perturbations at frequency ω ($\delta\phi(\omega)$ or $\delta \ln A(\omega)$ respectively) are linked to the Earth's 3D heterogeneities $\delta m(\mathbf{x})$ by phase or amplitude kernels, mathematically:

$$\begin{aligned} \delta\phi(\omega) &= \iiint_{\oplus} K_{\phi}^{m}(\mathbf{x},\omega)\delta m(\mathbf{x})d^3\mathbf{x}, \\ \delta \ln A(\omega) &= \iiint_{\oplus} K_{A}^{m}(\mathbf{x},\omega)\delta m(\mathbf{x})d^3\mathbf{x}, \end{aligned} \tag{2.7}$$

where K^m are the phase or amplitude sensitivity kernels, and $\iiint_{\oplus} d^3\mathbf{x}$ denotes an integration over a 3D volume of the Earth. When reducing the condition into 2D planar problems, the function 2.7 can be simplified into:

$$\delta d(\omega) = \iint_{\Omega} K_{d}^{c}(r,\omega)\left(\frac{\delta c}{c}\right)d\Omega, \tag{2.8}$$

where $\iint_{\Omega} d\Omega$ is the integration over a 2D sphere Ω, $\delta d(\omega)$ represents the phase perturbation $\delta\phi(\omega)$ or the amplitude perturbation $\delta \ln A(\omega)$, $\delta c/c$ is the phase velocity fractional perturbation, and $K_{d}^{c}(r,\omega)$ denotes the 2D phase or amplitude sensitivity kernel, i.e. $K_{\phi}^{c}(r,\omega)$ and $K_{A}^{c}(r,\omega)$ respectively. The phase velocity c in a weakly anisotropic medium [Smith and Dahlen, 1973] is described as:

$$c(\omega,\theta) = B_0(\omega) + B_1(\omega)\cos 2\theta + B_2(\omega)\sin 2\theta + B_3(\omega)\cos 4\theta + B_4(\omega)\sin 4\theta. \tag{2.9}$$

Here, θ is the event azimuth, B_0 is the averaged phase velocity and $B_{1,2}$ are 2θ dependent azimuthal anisotropic coefficients. $B_{3,4}$ are 4θ-dependent and often neglected because they only provide tiny contributions. The 2D sensitivity kernels in function 2.8, as illustrated by Zhou et al. [2004], are defined as:

$$\begin{aligned} K_{\phi}^{c}(r,\omega) &= \mathrm{Im}\left(\frac{2k^2\mathcal{S}'\mathcal{R}''e^{-i[k(\Delta'+\Delta''-\Delta)-(n'+n''-n)\pi/2+\pi/4]}}{\mathcal{S}\mathcal{R}\sqrt{8\pi k(|\sin\Delta'||\sin\Delta''|/|\sin\Delta|)}}\right), \\ K_{A}^{c}(r,\omega) &= -\mathrm{Re}\left(\frac{2k^2\mathcal{S}'\mathcal{R}''e^{-i[k(\Delta'+\Delta''-\Delta)-(n'+n''-n)\pi/2+\pi/4]}}{\mathcal{S}\mathcal{R}\sqrt{8\pi k(|\sin\Delta'||\sin\Delta''|/|\sin\Delta|)}}\right), \end{aligned} \tag{2.10}$$

where k is the wavenumber, $\mathcal{S}$ is the source radiation for the wave directly traveling to the receiver along the great circle path, while $\mathcal{S}'$ is the source radiation for wave traveling to a scatterer, $\mathcal{R}$ and $\mathcal{R}''$ are the receiver polarization for the direct incoming wave and the scattered wave, respectively. The integer n stands for the polar passage index, $n = 0$ corresponds to a minor-arc wave and $n = 1$ for a major-arc wave, Δ in this equation denotes the source-receiver epicentral distance for the direct wave, Δ' and Δ'' are the source-scatterer and the scatterer-receiver distance respectively. The schematic diagram of all the variables in function 2.10 is given in Figure 2.1.

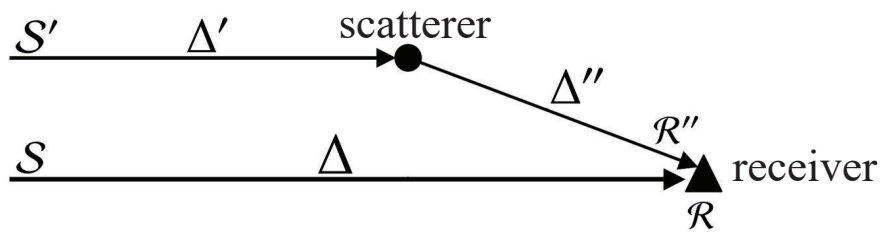

FIGURE 2.1: The schematic figure showing the propagation of a plane wave in a media where single scatterer exists. Modified after Yang and Forsyth [2006b].

Typically, the incoming surface waves in TPWT are regarded as plane waves when traveling through a long distance to a regional array. Hence, the source radiation $\mathcal{S}$ and $\mathcal{S}'$ are considered equal in this case. Also, the receiver polarizations $\mathcal{R}$ and $\mathcal{R}''$ are also equal to each other if only Rayleigh waves in vertical components are used. Thus, in a situation where only minor-arc waves presence (i.e. $n = 0$), the sensitivity kernels of function 2.10 can be further simplified into:

$$\begin{aligned} K_{\phi}^{c}(r,\omega) &= \mathrm{Im}\left(\frac{k^2 e^{-i[k(\Delta'+\Delta''-\Delta)+\pi/4]}}{\sqrt{2\pi k(|\sin\Delta'||\sin\Delta''|/|\sin\Delta|)}}\right), \\ K_{A}^{c}(r,\omega) &= -\mathrm{Re}\left(\frac{k^2 e^{-i[k(\Delta'+\Delta''-\Delta)+\pi/4]}}{\sqrt{2\pi k(|\sin\Delta'||\sin\Delta''|/|\sin\Delta|)}}\right). \end{aligned} \tag{2.11}$$

The accuracy of the sensitivity kernels in function 2.11 is systematically tested by comparing with the numerical simulations [Yang and Forsyth, 2006b]. The implantation of the 2D sensitivity kernels in TPWT successfully recovers the velocity anomaly with size larger or close to one wavelength of the surface waves and improves the resolution for regional tomographic studies [Yang and Forsyth, 2006a,b].

In practice, when processing surface wave data, a time window is generally utilized to separate the surface wave waveform from other waves. Therefore, the sensitivity kernels for

the separated surface waves are actually a integral of the single-frequency kernels over a range of adjacent frequencies. In addition, since the Gaussian weighting scheme is employed in producing the final tomographic maps (function 2.6), the 2D sensitivity kernels here should also be smoothed through the same approach in order to represent sensitivities at every grid nodes in the study region.

2.1.3 Inversion

As described in section 2.1.1, each incoming surface wave is parameterized by two interfering plane waves with unknown amplitude, initial phase and propagating direction. Thus, a total number of six wavefield parameters are required in the inversion and an iterative procedure is employed to solve the inverse problem. At the very beginning, a station with the largest amplitude is chosen as the reference station for each event, the amplitude and phase at other stations are then normalized by the reference station. The reason for choosing the station with the largest amplitude as the reference station is the two incoming waves are considered in phase at this station which then yield the largest amplitude. In the inversion scheme, misfits are defined upon the real and the imaginary components of the recording, which avoid the inaccuracy in directly fitting the phase or amplitude in a situation where destructive interference occurs.

Each iteration in the inversion can be divided into two stages. The first stage starts with a fixed velocity model which derives directly from the initial model or from the previous iteration. The main purpose of this stage is to assist the inversion in finding the global minimum when the two incoming waves have a similar propagating azimuth. The best fitting waveform parameters are searched through a downhill simplex method of simulated annealing [Press et al., 2007]. In the second stage of the iteration, a standard linearized inversion approach of Tarantola and Valette [1982] is adopted to invert for phase velocities and the six waveform parameters. The solution to the problem in the second stage can be written as:

$$\Delta m = (G^T C_{nn}^{-1} G + C_{mm}^{-1})^{-1} (G^T C_{nn}^{-1} \Delta d - C_{mm}^{-1} [m - m_0]), \tag{2.12}$$

where Δm represents the correction to the current model, Δd is the discrepancy between observed and predicted data, m and m_0 are the current model and the starting model, C_{mm} and C_{nn} denote the *a priori* model and data covariance matrix respectively, and the sensitivity matrix, G, relates the perturbation of m with the changes in the data d. Generally, the

data covariance matrix C_{nn} acts as a data weighting matrix with the diagonal elements representing the input data uncertainties, while the model covariance matrix C_{mm} acts as a damping regularization. The smoothing regularization is introduced to the velocity maps and the 2D sensitivity kernels (section 2.1.2) as the Gaussian weighting function with spatial width L_w in equation 2.6, whilst no smoothing is applied for the six waveform parameters. In practice, a relatively stable variation is produced after 4 to 5 iterations.

Under the TPWT inversion scheme, the final solution to the model and the six waveform parameters is solved through two group of iterations. In the first group of iterations (usually contains 5 to 10 iterations), the primary objective is to generate the *a posteriori* standard deviation for each teleseismic event. Then, in the second group of iterations (another 5 to 10 iterations), the *a priori* distribution is built upon the *a posteriori* standard deviations generated by the first group of iterations. The configuration of this two group iteration process successfully suppress the influences caused by the events with large residuals during inversion.

The resolution of the final velocity map is highly controlled by the width of the Gaussian weighting function, L_w, which relates the velocity value at each grid node to its neighbouring nodes. The uncertainty of the phase velocity map in TPWT is estimated by [Forsyth and Li, 2005]:

$$\begin{aligned} \sigma_v^2 &= \mathbf{q} C_{MM} \mathbf{q}^T, \\ C_{MM} &= (G^T C_{nn}^{-1} G + C_{mm}^{-1})^{-1}, \end{aligned} \tag{2.13}$$

where $\mathbf{q}$ is the weighting vector at a particular grid node, C_{MM} is the *a posteriori* covariance matrix. Generally, the uncertainties of phase velocities increase with increasing periods, resulting in a slightly lower resolution and damped velocity values at longer periods.

2.2 Ambient noise tomography

2.2.1 Cross-correlations and Empirical Green's Functions

Theoretically, the full Green's function between two receivers can be retrieved by cross-correlating ambient noise waveforms recorded at the two receivers [Lobkis and Weaver, 2001, Roux et al., 2005, Weaver and Lobkis, 2001]. Researchers have demonstrated the underlying mathematical theory from a variety of perspectives, such as the modal theory [Lobkis and

Weaver, 2001], time-reversed acoustics frame [Derode et al., 2003a,b], reciprocity theorem [Van Manen, 2006, Wapenaar and Fokkema, 2006, Wapenaar et al., 2005] and stationary-phase approach [Snieder, 2004, 2006]. However, the successful recovery of the full Green's function is valid only under the strict circumstances that the ambient noise field is diffusive with equipartitioning energy or the noise sources are evenly distributed [Snieder, 2004, Weaver and Lobkis, 2004]. Unfortunately, the real noise field is usually not fully diffusive and the sources are not homogeneously distributed. The recovery of full Green's function using real ambient seismic noise then becomes questionable. With later studies, seismologists found that the cross-correlation of ambient noise waveform is different from the full Green's function and dominated by surface wave signals which can produce reliable dispersions [Bensen et al., 2007, Campillo and Paul, 2003, Yang et al., 2011a, 2007, Yao et al., 2006]. Hence then, the noise cross-correlation waveform is referred as the empirical Green's function (EGF). In simple terms, the relationship between a cross-correlation function and a EGF is formulated as:

$$\frac{dC_{AB}}{dt} \approx -\frac{1}{2}(G_{AB}(t) - G_{BA}(-t)), \tag{2.14}$$

where C_{AB} is the cross-correlation of the ambient noise waveforms recorded at station A and station B, the G_{AB} and G_{BA} in the right hand represent the causal and anti-causal part of the EGF between station A and B. The above function indicates the link between the derivative of a cross-correlation with respect to time and the superposition of the EGF and its time-reversed part. It should be noted that the two sides of this function is not identical. The reason behind this asymmetry is the unknown frequency-dependent amplitude factor [Weaver and Lobkis, 2001], which then results in the incorrect amplitude information in the recovered EGF.

When considering the time-averaged cross-correlation, the mathematical expression of C_{AB} is defined as:

$$C_{AB}(t) = \frac{1}{T}\int_0^T \langle v_A(\tau)v_B(t+\tau)\rangle d\tau, \tag{2.15}$$

where $\langle\cdot\rangle$ denotes the expectation value, T represents the total length of the observation, t is the lag time in the cross-correlation, and v_A, v_B indicates the time domain ambient noise waveform recorded at station A and B respectively.

2.2.2 Single station preparations

As a commonly used method to image the earth's interior structure, the ANT technique is widely applied and the data processing procedure for ANT is nearly standardized [Bensen et al., 2007]. Prior to cross-correlation, instrument responses are first removed for continuous seismic data at each station. Then, continuous seismic data are resampled and bandpass filtered. The sampling rate and the bandpass filter period range are different dependant on specific periods of interest. The processed data are then cut to certain lengths for stacking purposes.

The most important step in the single station preparation is the temporal and spectral normalization. Time-domain normalization is employed to reduce the influences caused by earthquakes and/or instrument irregularities. These unwanted signals are regarded as 'noise' in the ANT framework. Bensen et al. [2007] has compared several different methods for temporal normalization, such as the one-bit normalization, running absolute mean normalization, 'water level' normalization and so on. The effectiveness of different methods are systematically documented by Bensen et al. [2007], Groos et al. [2012].

In this thesis, the running absolute mean normalization method is utilized in the ANT data processing in chapter 3 and 4. This normalization approach normalizes time series using the averages of the absolute values in a surrounding window and can be formulated as:

$$\widetilde{v}(i) = v(i) / \left(\frac{1}{2N+1} \sum_{j=i-N}^{i+N} |v(j)| \right) \tag{2.16}$$

where $v(i)$ is the waveform value at time i, $\widetilde{v}(i)$ represents the time-series after the normalization, $(2N + 1)$ is the time window width when calculating the averaged absolute value.

As the amplitude spectrum of ambient noise is generally not flat, spectral whitening is introduced to flatten and broaden the frequency band of the ambient noise signals. In this thesis, influences of the spectral whitening on real data are also tested during ANT data processing. The testing result shows that, reliable phase velocities at a wider period band can be measured when spectral whitening is applied. Thus, the spectral whitening step is considered essential in this thesis and employed in chapter 3 and 4.

2.2.3 Temporal stacking

Temporal stacking is a necessary step in ANT data processing since stacking cross-correlations over a long time span can compensate for the unevenly distributed ambient noise sources,

enhance the signal and reduce the uncorrelated noise. Most ANT studies to date typically employ a linear stacking approach to boost the signal-to-noise ratio (SNR) of the EGFs. The ability of linear stacking approach in boosting SNR is restricted to a factor of $N^{1/2}$, where N is the number of cross-correlation segments. More effective stacking techniques have been developed in the past few years.

Schimmel and Paulssen [1997] proposed a non-linear stacking method termed as phase-weighted stacking (PWS). The PWS method introduces a weighting factor based on the coherency of the instantaneous phases into linear stacking and achieves a huge improvement in enhancing weak but coherent signals. However, heavy waveform distortions are introduced simultaneously in the final stacked traces, making the PWS method unsuitable for phase velocity measurements and limits its applications in ANT. Later, Schimmel and Gallart [2007] slightly modified the PWS method by measuring local phases from S transform rather than from the Hilbert transform in the original PWS method. The improved stacking algorithm, which minimizes the distortions in the original PWS, is referred as the time-frequency PWS method (tf-PWS). The mathematical expression of tf-PWS function is:

$$S_{tf\_pws}(\tau, f) = |c_{ps}(\tau, f)|^{v} \frac{1}{N} \sum_{j=1}^{N} S_j(\tau, f), \tag{2.17}$$

where the $c_{ps}(\tau, f)$ with a power v is a coherence dependent weighting term that vary from 0 to 1, the power v controls the sharpness of the coherent signals, N and j represent the total number and index of trace, $S_j(\tau, f)$ denotes the elapse time spectrum for jth trace at elapse time τ and it is calculated through S transform. The weighting term $c_{ps}(\tau, f)$ is expressed as:

$$c_{ps}(\tau, f) = \frac{1}{N} \sum_{j=1}^{n} e^{i\phi_j(\tau, f)}, \tag{2.18}$$

the $\phi_j(\tau, f)$ refers to the phase spectrum of the elapse time spectra $S(\tau, f)$. The S transform is a generalization of the short-time Fourier transform (STFT) widely used in geophysical studies and defined as [McFADDEN et al., 1999]:

$$S(\tau, f) = \int_{-\infty}^{+\infty} v(t)\omega(\tau - t)e^{-i2\pi ft} dt, \tag{2.19}$$

where $v(t)$ is the time serials, $\omega(\tau - t)$ refers to a Gaussian window function centered at τ:

$$\omega(\tau - t) = \frac{|f|}{k\sqrt{2\pi}} e^{\frac{-f^2(\tau - t)^2}{2k^2}}, \tag{2.20}$$

here, k is a factor controlling the resolution of the elapse time spectrum. The factor k can vary to form different types of S transform, such as the original S transform where $k = 1$

[Stockwell et al., 1996], the modified S transform where k is a variable of time or frequency [Assous and Boashash, 2012, Du et al., 2007, Li and Castagna, 2013].

The stacked elapse spectrum $S_{tf\_pws}(\tau, f)$ are then transferred back into time domain to generate the EGFs through the inverse S transform (IST). The IST can either be performed in the frequency domain as shown in Stockwell et al. [1996] or in the time domain illustrated by Schimmel and Gallart [2005], Schimmel et al. [2011]. The algorithms for these two different IST and their output EGFs are systematically demonstrated and tested by Li et al. [2018]. According to this paper, large distortions are observed for EGFs generated from time domain IST, especially at longer periods. Phase velocities measured from these EGFs display a non-negligible deviation from the linear stacking, reaching 0.3% at period around 40s. While for the EGFs calculated by frequency domain IST, phase velocity deviations are much smaller, only reaching a maximum value of 0.1% around 30s period. Hence then, in the tf-PWS stacking scheme, frequency domain IST is preferred and the calculation is quite straightforward:

$$\begin{aligned} v(t) &= \int_{-\infty}^{+\infty}\int_{-\infty}^{+\infty} S(\tau, f) d\tau e^{i2\pi f t} d\tau df \\ &= \int_{-\infty}^{+\infty} V(f) e^{i2\pi f t} df, \end{aligned} \tag{2.21}$$

where $v(t)$ is the time serials and $V(f)$ is the Fourier transform of $v(t)$.

Because the tf-PWS stacking technique measure the signals that are more phase coherent, it has a great natural advantage over traditional linear stacking when dealing with weak signals in cross-correlations and can boost SNR remarkably. Figure 2.2 illustrates several example EGFs generated by the linear stacking method (left panel in figure 2.2) and the tf-PWS method (right panel in figure 2.2). It is obvious that the EGFs calculated by tf-PWS method have a higher SNR when compare to the EGFs from linear stacking, particularly for EGFs with larger inter-station distances. The averaged frequency-dependent SNR for both linear stacking appraoch and the tf-PWS method is shown in figure 2.3, the SNR of EGFs by tf-PWS are significantly higher than the EGFs from linear stacking. The higher SNR will then yield more ray path numbers in tomography, which directly enhance the resolution of the final phase velocity maps. For example, in chapter 4, number of ray paths are increased by ~10% at each period after introducing the tf-PWS stacking method.

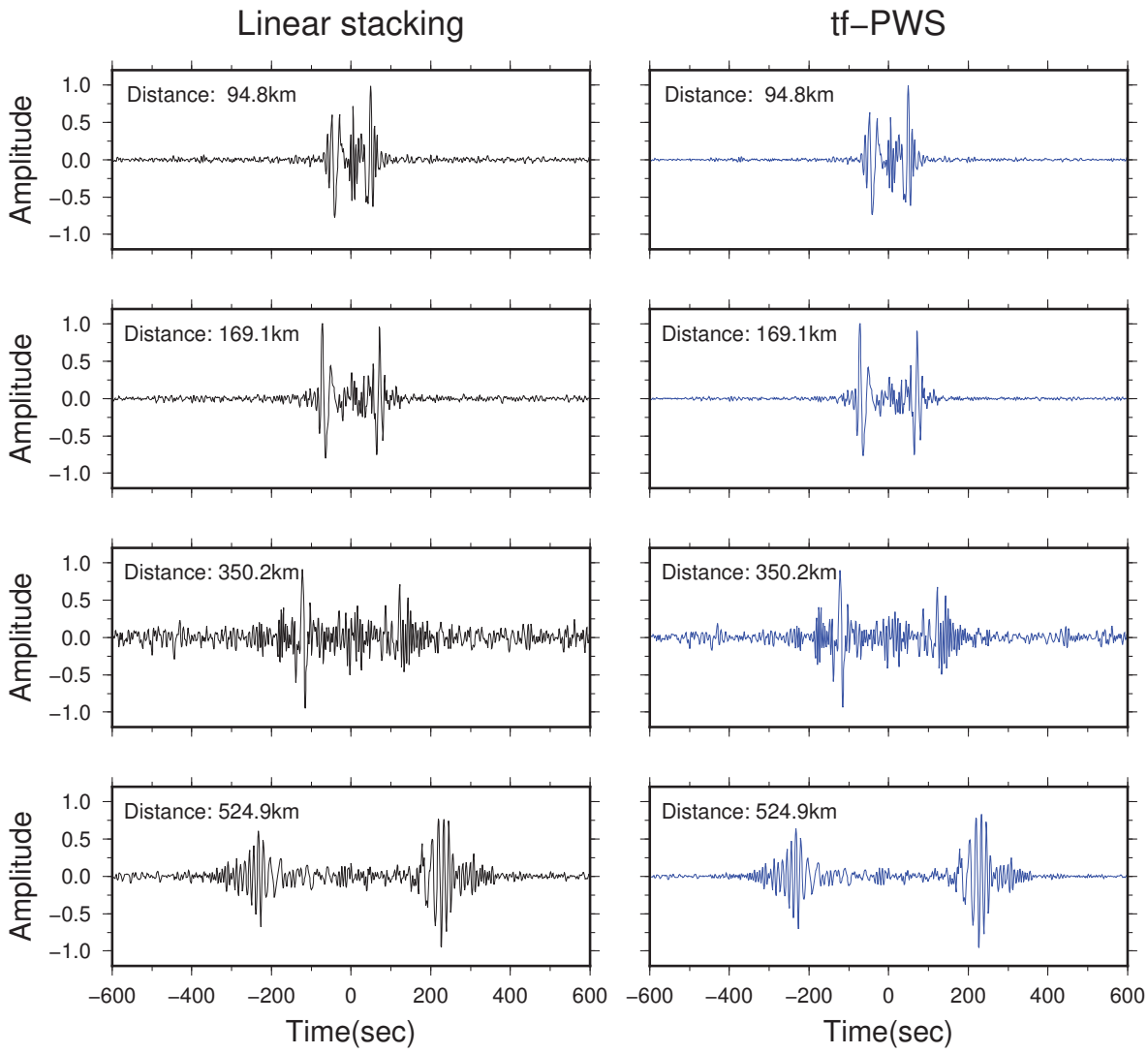

FIGURE 2.2: Comparison between EGFs generated by the linear stacking (left) and the tf-PWS method (right), the amplitude of each EGF is normalized by its maximum value for plotting purposes. EGFs in this figure are selected from the cross-correlation data in chapter 4, the inter-station distances are shown in the top left in each subfigure.

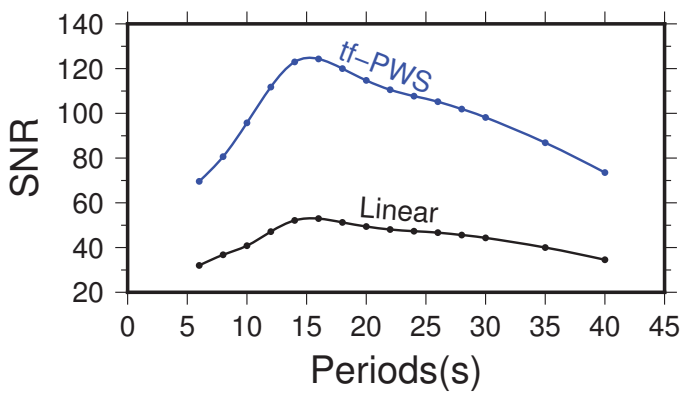

FIGURE 2.3: Averaged frequency-dependent SNR of the EGFs in chapter 4. Note a significant improvement for EGFs generated by tf-PWS method (blue solid line).

2.3 Markov chain Monte Carlo inversion

In this thesis, local phase velocity dispersions derived from surface wave tomography (ANT and TPWT) in chapter 3 and 4 are used to invert for the 1D shear wave velocity (Vs) structure beneath each inversion grid. A probabilistic (Bayesian) inference Markov chain Monte Carlo (MCMC) nonlinear inversion approach [Afonso et al., 2013a,b, Guo et al., 2016b] is employed to solve the inversion problem. As a powerful tool to solve non-linear problems, the MCMC method is widely applied in multiple disciplines, such as geophysics [e.g. Bodin et al., 2012, Khan et al., 2009, Molnar et al., 2010, Shapiro and Ritzwoller, 2002, Shen et al., 2013, Socco and Boiero, 2008], chemical kinetics [e.g. Battaile and Srolovitz, 2002, Boys et al., 2008, Golightly and Wilkinson, 2005, 2006], finance [e.g. Dagpunar, 2007, Eraker, 2001, Greyserman et al., 2006, Korn et al., 2010], ecology [e.g. Beaumont, 2010, Malve et al., 2005, 2007, Nylander et al., 2007], etc. In seismology, numerous studies have successfully implemented the MCMC algorithm into joint inversion of receiver functions and surface wave dispersions [e.g. Agostinetti and Chiarabba, 2008, Agostinetti and Malinverno, 2010, Hetényi and Bus, 2007, Jiang et al., 2014, Shen et al., 2013, Vinnik et al., 2004].

The solution of the Bayesian inference inversion is represented by a posterior probability density function (PDF), $p(\theta|y)$, which can be formulated under the Bayesian theorem as:

$$p(\theta|y) = \frac{p(y|\theta)p(\theta)}{p(y)}, \tag{2.22}$$

where θ and y represent the model parameters and the observational data, $p(y|\theta)$ is the density function of y when θ is given, also known as the $likelihood\ function$, $p(\theta)$ is the unconditional distribution of the unknowns, also known as the $a\ priori$ distribution. This $a\ priori$ distribution consists of our prior knowledge about the model θ. For most geophysical problems, usually the observational data y are fixed and $p(y)$ then becomes a constant. Thus, function 2.22 can be simplified and expressed according to geophysical manner as:

$$p(m|d_{obs}) \propto p(d_{obs}|m)p(m), \tag{2.23}$$

where θ and y in function 2.22 are represented by m and d_{obs} respectively. The $likelihood\ function$, $p(d_{obs}|m)$, in surface wave dispersion inversions, is defined by the misfit function $S(m)$ as follows:

$$\begin{aligned} p(d_{obs}|m) &= \exp\left(-\tfrac{1}{2}S(m)\right), \\ S(m) &= \left[g(m) - d_{obs}\right]^T C_e^{-1} \left[g(m) - d_{obs}\right], \end{aligned} \tag{2.24}$$

here, $g(m)$ is the data predictions from model m, C_e denotes the data covariance matrix.

The MCMC simulation generate a series of values $(m^0, m^1, \ldots, m^N)$ which follow a stochastic process called the Markov chain, these values are not independent but instead somehow depend on the previous values in the chain. The posterior PDF actually is an assemble of the accepted values left in the end of the chain. Therefore, how to efficiently and correctly sample these values becomes extremely important in any MCMC applications. In the following sections, several sampling algorithms will be presented and briefly introduced.

2.3.1 The Metropolis-Hastings algorithm

The Metropolis-Hastings algorithm (MH) is first introduced by Metropolis et al. [1953] and extended by Hastings [1970], and is the most generally used algorithm in MCMC schemes. The fundamental idea of MH is very straightforward. Let's use $\pi(m)$ to represent the target distribution, the MH algorithm measures the ratio between two different target distribution $(\pi(m)/\pi(m^*))$ instead of computing a single $\pi(m)$. Note that $\pi(m)$ here corresponds to the posterior PDF $p(m|d_{obs})$ in function 2.23. The Metropolis-Hastings acceptance probability α in MH algorithm is defined as:

$$\alpha(m, m^*) = \min\left\{1, \frac{\pi(m^*)q(m^*, m)}{\pi(m)q(m, m^*)}\right\}, m \neq m^*, \tag{2.25}$$

where q is called the proposal density with the first element representing the current location in the chain. The choice of q can be arbitrary, it could be a Gaussian or uniform distribution. In practice, the proposal density q in phase velocity inversion is generally set to be the Gaussian density and then the ratio of $q(m^*, m)/q(m, m^*)$ in function 2.25 will be cancelled out. In brief, the MH algorithm follows these steps:

1. Propose an initial value m^0 and define the proposal density q.
2. Generate a new parameter m^* according to the current m through the proposal density $q(m, \cdot)$.
3. If $\pi(m^*)q(m^*, m) > \pi(m)q(m, m^*)$, i.e. $\alpha = 1$ in function 2.25, the proposed value m^* will be accepted unconditionally.
4. If it does not meet the above criteria, m^* will be accepted with a probability α given in function 2.25.
5. If m^* is rejected, the chain will stay at its current value m.
6. Repeat step 2 to 5 until enough proposals have been accepted.

2.3.2 Adaptive Metropolis algorithm

The MH algorithm highly depends on the choice of the proposal distribution q, which means choosing a proper distribution that is very close to the target distribution will dramatically shorten the convergence time. However, the real target distribution is usually unknown and different for different problems, making it difficult to chose the proposal distribution [Gelman et al., 1996, Gilks et al., 1996, 1998, Haario et al., 1999, Roberts et al., 1997]. The concept of Adaptive Metropolis algorithm (AM) is first documented by Haario et al. [1999, 2001], the proposal covariance in the AM algorithm is defined as the covariance of the chain to its current location. Therefore, by employing the Gaussian proposal distribution as an initial, we can successfully solve more problems than the original MH algorithm, especially in highly non-linear situations. In brief, the AM algorithm follows these steps:

1. Propose an initial value m^0 and define the initial proposal covariance C_0. Set a covariance scaling factor s, a small number ε to regulate the covariance, and a non-adaptiong period n_0.
2. Generate a new parameter m^* according to a Gaussian distribution $N(m, C)$ centered at m, m is the current location of the chain.
3. Judge the m^* by the MH algorithm in section 2.3.1.
4. When the time of simulations reaches n_0, adapt the proposal covariance according to the previous values in the chain:

$$C = \mathrm{cov}(m^0, m^1, \ldots, m^i)s + I\varepsilon, i \geq n_0. \tag{2.26}$$

   The adaption can be done from the beginning of the chain or at certain intervals (fixed or random) within the chain.
5. Back to step 2 until enough values have been generated.

2.3.3 Delayed rejection

In the MH algorithm, once a proposal is rejected, this proposed value is then deleted and the chain stays at the previous position. The delayed rejection method (DR) is a different algorithm which delays the rejection of a 'bad' proposal [Green and Mira, 2001, Mira et al., 2001]. In the DR scheme, a second move is introduced after the rejection of a proposed value, this process can be iterated for arbitrary times. The DR algorithm begins with the MH

acceptance probability:

$$\alpha_1(m, m^*) = \min\left\{1, \frac{\pi(m^*)q(m^*, m)}{\pi(m)q(m, m^*)}\right\}. \tag{2.27}$$

The meanings of the symbols here are the same as in function 2.25. Once the m^* is rejected, a second move m^{**} is suggested in the DR method with the acceptance probability:

$$\alpha_2(m, m^*, m^{**}) = \min\left\{1, \frac{\pi(m^{**})q_1(m^{**}, m^*)q_2(m^{**}, m^*, m)[1 - \alpha_1(m^{**}, m^*)]}{\pi(m), q_1(m, m^*)q_2(m, m^*, m^{**})[1 - \alpha_1(m, m^*)]}\right\}. \tag{2.28}$$

This procedure can be iterated for further higher-stage proposals. By employing the DR method in sampling the posterior PDF, the MCMC asymptotic variance is reduced than the MH algorithm, in another words, this DR chain is more efficient when compares to the standard MH algorithm [Mira et al., 2001].

2.3.4 DRAM

By combining the DR and the AM, a new improved method arises, i.e. the DRAM. The DRAM algorithm is first introduced by Haario et al. [2006]. This algorithm provides a automatic burn-in with small initial tuning and short burn-in period, increasing the efficiency of the MH type MCMC algorithms. The steps of DRAM can be concluded as:

1. Propose an initial value m^0 and define the initial proposal covariance $C^1 = C_0$. Set a covariance scaling factor s, a small number ε to regulate the covariance, a initial non-adaption period n_0, and covariances for the higher stage proposals $C^i, i = 1, 2, \ldots, N$, where N is the maximum time of tries allowed.
2. Enter DR loop until a new proposal is accepted or the maximum proposal time of N is reached:
   a) Make m^* from a Gaussian distribution $N(m, C^k)$ similar to AM algorithm step 2.
   b) Accept the proposal m^* according to the kth stage acceptance probability α.
3. If the new value is accepted, set the current chain to m^* or keep it as m if the new value is rejected.
4. After the time of simulations reaches n_0, adapt the proposal covariance according to the previous values in the chain similar to the step 4 in AM:

$$C^1 = \mathrm{cov}(m^0, m^1, \ldots, m^i)s + I\varepsilon, i \geq n_0. \tag{2.29}$$

   Generate the higher stage proposals based on the C^1 and the defined rule.

5. Repeat from step 2 until enough proposals are accepted.

For the surface wave dispersion inversion in this thesis (chapter 3 and 4), the posterior PDFs, which is usually with a large parameter space and no closed form, is sampled by this DRAM algorithm.

2.4 Body wave finite-frequency tomography

The theoretical basis of body wave finite frequency tomography (BWFFT) is the so called banana-doughnut theory that was firstly proposed by Marquering et al. [1999] based on surface wave coupling theory in conjunction with Born approximation. Based on body wave ray summation theory, Dahlen et al. [2000] developed an paraxial approximation method to calculate banana-doughnut kernels in a more efficient way, which is now widely adopted in most BWFFT studies and also in this thesis.

2.4.1 Body wave ray theory

According to JWKB theory [Dahlen and Tromp, 1998], the impulse response $\mathbf{G_{rs}}(\omega)$ solution to the equation of motion is expressed as a summation of all body waves from the source $\mathbf{s}$ to the receiver $\mathbf{r}$. In frequency domain [Dahlen et al., 2000], that is

$$\mathbf{G_{rs}}(\omega) = \frac{1}{4\pi} \sum_{rays} \hat{\mathbf{p}}_s \hat{\mathbf{p}}_r (\rho_r \rho_s c_r c_s^3)^{-1/2} \Pi_{rs} \mathscr{R}_{rs}^{-1} \times \exp[i(-\omega T_{rs} + M_{rs}\pi/2)], \tag{2.30}$$

where $\hat{\mathbf{p}}_s$ and $\hat{\mathbf{p}}_r$ denote the polarization vectors at the source and receiver,respectively. ρ is density and the two c are the wave speeds for either α or β depending on whether there is conversion of P and S waves. Π_{rs} and $\mathscr{R}_{rs}$ are the reflection-transmission coefficients and geometrical spreading factors. T_{rs} is the traveltime, and M_{rs} is the number of caustic passages.

For a specific moment tensor source $m(\omega)$, the frequency domain displacement [Dahlen and Tromp, 1998] is expressed as:

$$s(\omega) = \sqrt{2} M_0 (i\omega)^{-1} \dot{m}(\omega) \hat{\mathbf{v}} \cdot \left[\hat{\mathbf{M}} : \nabla_s \mathbf{G}_{\mathbf{rs}}^T(\omega)\right], \tag{2.31}$$

where $\hat{\mathbf{v}}$ represents the component direction of displacement. M_0 is the scalar moment, and $\hat{\mathbf{M}}$ is the unit source mechanism tensor that satisfies $\hat{\mathbf{M}} : \hat{\mathbf{M}} = 1$. Upon collecting the source

and receiver terms separately in the above equation, it can be reduced to a more simple form:

$$s(\omega) = \frac{1}{4\pi} \sum_{rays} \Lambda \Upsilon \Pi_{rs} \mathscr{R}_{rs}^{-1} \dot{m}(\omega) \exp[i(-\omega T_{rs} + M_{rs}\pi/2)], \tag{2.32}$$

where Λ and Υ are the source and receiver factors as defined in Dahlen et al. [2000].

2.4.2 Born approximation and banana-doughnut kernels

According to Dahlen et al. [2000], the first order Born scattering theory gives the expression of a perturbed Green's tensor in terms of perturbed model parameters and Green's tensors in a reference medium. That is,

$$\begin{aligned} \delta \mathbf{G_{rs}} = \quad & \iiint \delta\rho(\omega^2 \mathbf{G_{rx}} \cdot \mathbf{G_{xs}}) d\mathbf{x}^3 \\ & - \iiint \delta\lambda(\nabla \cdot \mathbf{G}_{\mathbf{rx}}^T)(\nabla \cdot \mathbf{G_{xs}}) d\mathbf{x}^3 \\ & - \iiint \delta\mu(\nabla \mathbf{G_{rx}})^T : [\nabla \mathbf{G_{xs}} + (\nabla \mathbf{G_{xs}})^T] d\mathbf{x}^3. \end{aligned} \tag{2.33}$$

Similar to eq. 2.31, the perturbed displacement in the frequency domain is

$$\delta s(\omega) = \sqrt{2} M_0 (i\omega)^{-1} \dot{m}(\omega) \hat{\mathbf{v}} \cdot \left[\hat{\mathbf{M}} : \nabla_s \delta \mathbf{G}_{\mathbf{rs}}^T(\omega) \right], \tag{2.34}$$

Substituting eq. 2.33 into eq. 2.34,

$$\begin{aligned} \delta s(\omega) = \left(\frac{\omega}{4\pi}\right)^2 \iiint \Bigg\{ & \sum_{\text{rays}'} \sum_{\text{rays}''} (c' c''^3)^{-1/2} \\ & \times \Lambda' \Upsilon'' \Pi_{rx} \Pi_{xs} (\mathscr{R}_{rx} \mathscr{R}_{xs})^{-1} (\hat{\mathbf{p}}'' \cdot \mathbf{S} \cdot \hat{\mathbf{p}}') \dot{m}(\omega) \\ & \times \exp i[(-\omega(T_{rx} + T_{xs}) + (M_{rx} + M_{xs})\pi/2)] \Bigg\} \, d\mathbf{x}^3, \end{aligned} \tag{2.35}$$

where a single prime denotes qualities source to scatterer and double prime denotes those from a scatterer to a receiver. $\mathbf{S}$ is a second-order scattering tensor that captures all scattering information of an incoming body wave into an outgoing wave at $\mathbf{x}$.

For a cross-correlation traveltime measurement, the traveltime perturbation is related to perturbed displacement fields as

$$\delta T = \frac{\text{Re} \int_0^\infty i\omega s^*(\omega) \delta s(\omega) d\omega}{\int_0^\infty \omega^2 |s(\omega)|^2 d\omega}, \tag{2.36}$$

where the asterisk represents complex conjugation.

In finite frequency tomography, the traveltime perturbations are related to model parameters by 3-D Fréchet kernel over a volume integral, that is

$$\delta T = \iiint \left[K_\alpha \left(\frac{\delta\alpha}{\alpha} \right) + K_\beta \left(\frac{\delta\beta}{\beta} \right) + K_\rho \left(\frac{\delta\rho}{\rho} \right) \right] d^3\mathbf{x}, \tag{2.37}$$

where, K_α, K_β, K_ρ are the so called banana-doughnut kernels. By defining a dimensionless product:

$$N = \left(\frac{\Lambda'}{\Lambda} \right) \left(\frac{\Upsilon'}{\Upsilon} \right) \left(\frac{\Pi'\Pi''}{\Pi} \right). \tag{2.38}$$

The sensitivity kernels can be written in the form:

$$\begin{aligned} K_{\alpha,\beta,\rho} = &- \frac{1}{2\pi} \sum_{\text{rays}'} \sum_{\text{rays}''} N\Omega_{\alpha,\beta,\rho} \left(\frac{1}{\sqrt{c'c''}} \right) \left(\frac{\mathscr{R}}{c_r \mathscr{R}' \mathscr{R}''} \right) \\ &\times \frac{\displaystyle\int_0^\infty \omega^3 |\dot{m}(\omega)|^2 \sin[\omega(T' + T'' - T) - (M' + M'' - M)\pi/2] d\omega}{\displaystyle\int_0^\infty \omega^2 |\dot{m}(\omega)|^2 d\omega}. \end{aligned} \tag{2.39}$$

The calculation of these kernels demands a double sum of all possible ray paths from a source to a scatterer (rays′) and a scatterer to a receiver (rays″) at every scatterer, which makes it computationally heavy.

2.4.3 Paraxial kernels

Realizing that traveltime perturbations are mostly sensitive to model heterogeneities at a banana-doughnut area in the vicinity of the centre ray, Dahlen et al. [2000] proposed a paraxial approximation method to calculate these kernels within the first Fresnel zone. This method relies on two assumptions:

(1) Only the so called 'like-type' scattering paths are considered as paraxial rays, which have the same number and type of boundary interactions as the centre ray path. Thus, the factor $N = 1$.

(2) The outgoing and incoming wave vector at the scatterer are assumed to be identical, thus the amplitude of scattering coefficients ($\Omega_{\alpha,\beta,\rho}$) is 1 for P→P off a $\delta\alpha$ heterogeneity and S→S off a $\delta\beta$ heterogeneity, and zero for other types of scattering.

Based on these approximations, the computation of the banana-doughnut kernels is reduced to a more efficient form:

$$K_{\alpha,\beta,\rho} = -\frac{1}{2\pi} \sum_{\text{rays}'} \sum_{\text{rays}''} \left(\frac{1}{\sqrt{c'c''}} \right) \left(\frac{\mathscr{R}}{c_r \mathscr{R}' \mathscr{R}''} \right) \frac{\int_0^\infty \omega^3 |\dot{m}(\omega)|^2 \sin \Phi d\omega}{\int_0^\infty \omega^2 |\dot{m}(\omega)|^2 d\omega}, \tag{2.40}$$

where Φ is the phase factor in eq. 2.39.

Considering a ray-centred coordinate, the position of each scatterer is described as:

$$\mathbf{x} = \xi + \mathbf{q} = (q_1, q_2, l), \tag{2.41}$$

where ξ is the nearest point on the central ray, and $\mathbf{q}$ is the vector from ξ to the scatterer. The "nearest" means that $\mathbf{q}$ is perpendicular to the ray direction at point ξ. The point ξ is parameterized by the arclength $0 \leq l \leq L$, where 0 is the start point at the source and L is the start point at the receiver. q_1 and q_2 are the two orthogonal components of $\mathbf{q}$. In this ray-centred coordinate, the phase factor Φ is related to the forward and backward Hessians as:

$$\Phi = \frac{1}{2}\omega \mathbf{q}^T \cdot (\mathbf{M}' + \mathbf{M}'') \cdot \mathbf{q} - [\text{sig}(\mathbf{M}' + \mathbf{M}'') - 2]\pi/4 \tag{2.42}$$

The steps for calculating the paraxial kernel is summarized in the following.

1) Ray tracing from the source to the receiver.
2) Calculating the position of every potential scattering point $\mathbf{x} = (q_1, q_2, l)$ in the ray-centred coordinate.
3) Computing the forward and backward Hessians $\mathbf{M}'$ and $\mathbf{M}''$ at every point $\xi = (0, 0, l)$.
4) Calculating the paraxial kernels based on eq. 2.40, allowing for multiple projections.

In this paraxial framework, one only needs to conduct a single numerically intensive two-point ray tracing. As long as the centre ray is determined, the two Hessians $\mathbf{M}'$ and $\mathbf{M}''$ are calculated based on numerical integration. In this way, the paraxial approximation method significantly reducse the computation cost of the exact ray-theoretical kernel which requires a double sum of all possible scattering waves.

3

Seismological Evidence for a Remnant Oceanic Slab in the Western Junggar, Northwest China

3.1 Summary

The western Junggar is situated in the southwestern Central Asian Orogenic Belt, and its origin is believed to be related to either intracontinental arc or intraoceanic arc-related subduction system. However, the mode of subduction is still contentious. In this study, we build a high-resolution 3-D model of the crust of the western Junggar to constrain the subduction mode. By deploying a seismic array consisting of 31 portable broadband seismic stations from September 2013 to December 2013, we determine the Moho depth beneath every station using a H-κ method and the Moho variations along three NW-SE profiles using a common conversion point stacking method. We also construct a 3-D crustal S wave velocity model

using ambient noise tomography. Our results reveal significant variations of Moho depths across the study region and a pronounced Moho offset between the Zaire mountains and the western Junggar basin. Ambient noise tomography shows that a high shear velocity layer (> 3.9 km/s) is observed in the middle/lower crust of the western Junggar Basin, which is overlaid by a low velocity upper crust. The high-velocity body gradually dips northwestward with depth beneath the Zaire mountains. The speed of this high-velocity body is consistent with the calculated *S* wave speed of various metamorphic facies of mid-ocean ridge basalt under the P/T conditions of middle/lower crust in the western Junggar. Our seismic observations support a northwest paleosubduction model for the evolution of the western Junggar, in which a remnant oceanic slab is still trapped in the western Junggar.

3.2 Introduction

The Central Asian Orogenic Belt (CAOB), also knownas the Altaid Tectonic Collage, is one of the largest orogens among the world and comprises island arcs, seamounts, accretionary wedges, oceanic plateau and, possibly, microcontinents accreted during the closure of the Paleo-Asian Ocean [Jahn, 2000, Kröner et al., 2008, 2007, Şengör et al., 1993, Windley et al., 2007, Xiao et al., 2015a]. The CAOB extends from the Urals in the west, through Kazakhstan, northern China, and Mongolia to the eastern Russian coast. The CAOB is a wide orogenic collage formed during the Paleozoic as a result of the convergence of Siberia, Baltica, Tarim, and North China blocks. The complex tectonic evolutionary history and associated metallogeny in the CAOB have attracted great attention of geologists worldwide [e.g., Cao et al., 2014, Kröner et al., 2008, Ma et al., 2012, Shen et al., 2015, 2009, Tang et al., 2010, Xiao et al., 2015a, Yakubchuk, 2004].

The western Junggar region, situated in the southwestern CAOB, is surrounded by the Altai Orogen to the north, the Tien Shan Orogen to the south, the Kazakhstan Plate to the west, and the Junggar Basin to the east [e.g., Buckman and Aitchison, 2004, Coleman, 1989, Feng et al., 1989, Figure 3.1]. This region is characterized by the Paleozoic ophiolites, volcanic rocks, and many valuable Cu-Au-bearing ore deposits, along with three NE striking faults, which are Hatu, Karamay-Urho, and Darbut faults. Particularly along the more than 200-km-long Darbut Fault and the hidden Karamay-Urho Fault (K-U fault), lenses of ophiolitic mélanges crop out discretely [Chen and Arakawa, 2005, He et al., 2007, Xu et al., 2006]. The

late Paleozoic magmatism and deformation extensively occurred in this region [Chen et al., 2010, Gao et al., 2014, Li et al., 2015, Ma et al., 2015, Xiao et al., 2008, Yan et al., 2015, Zhang et al., 2011a,b] and also the entire CAOB [Jahn, 2000, Şengör et al., 1993].

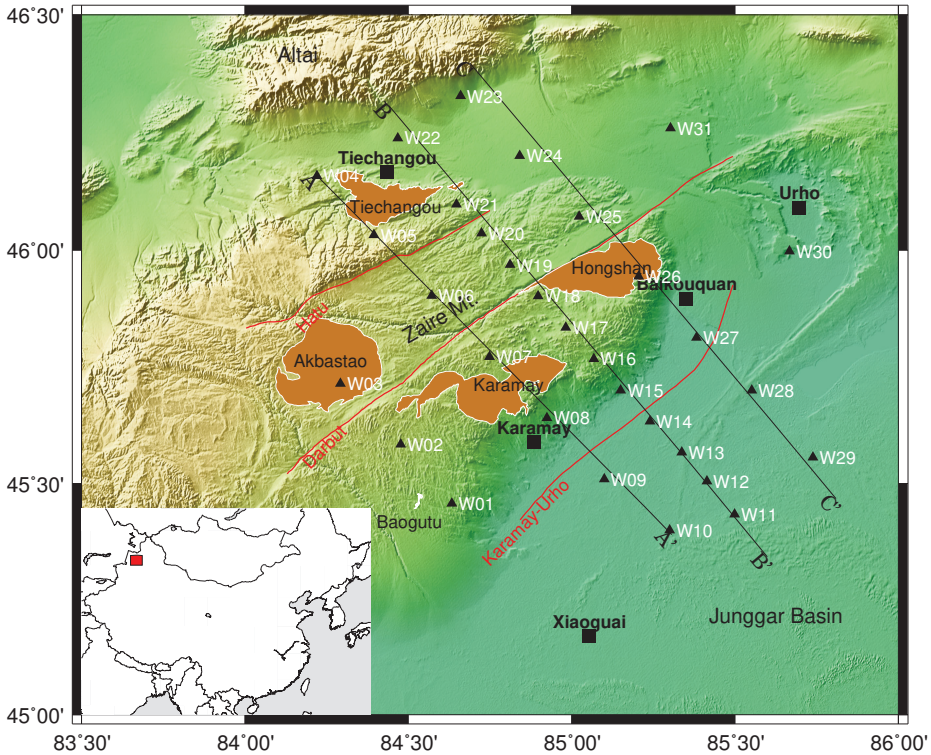

FIGURE 3.1: Tectonic settings of the western Junggar. The red lines indicate the major faults, and the black triangles indicate the seismic array. The three black lines delineate the three profiles AA', BB', and CC'. The red box in the inset indicates the location of our study region.

The western Junggar is an ideal place to study the evolutionary history of the CAOB. The tectonic origin of the western Junggar is believed to be related to either intracontinental arc [Zhang and Huang, 1992] or intraoceanic arc-related subduction system [Su et al., 2006, Xiao et al., 2008] which developed in the early Paleozoic and closed in the late Paleozoic. However, the mode of subduction still remains elusive. Based on geological, geophysical, and geochemical studies, several competing models of the subduction have been proposed, including a northwestward subduction to continental arc [Li et al., 2006], a double side subduction [Yang et al., 2012a], a failed northwestward intraoceanic subduction [Xu et al., 2016], and an oceanic-ridge involved subduction [Geng et al., 2009]. These different models would predict different crustal structure associated with the different subduction modes. Thus, imaging the high-resolution crustal structure helps discriminate among the competing

models.

In order to build a high-resolution 3-D model of the crust, we deployed a seismic array consisting of 31 portable broadband seismic stations from September 2013 to December 2013. This array mainly comprised three NW-SE profiles plus five offline stations (Figure 3.1). Because it is hard to access to the Altai (Xiemisitai) mountains with elevations of more than 4 km in the west and the Junggar desert in the east, the deployed array is limited to a dimension of ~120 km (Figure 3.1). From this seismic array, we then collect teleseismic events to determine the crustal thickness and also perform ambient noise tomography to construct a 3-D shear velocity model of the crust. The crustal model constrained by receiver functions and ambient noise data provides new insight into the Paleo-subduction system in western Junggar, NW China.

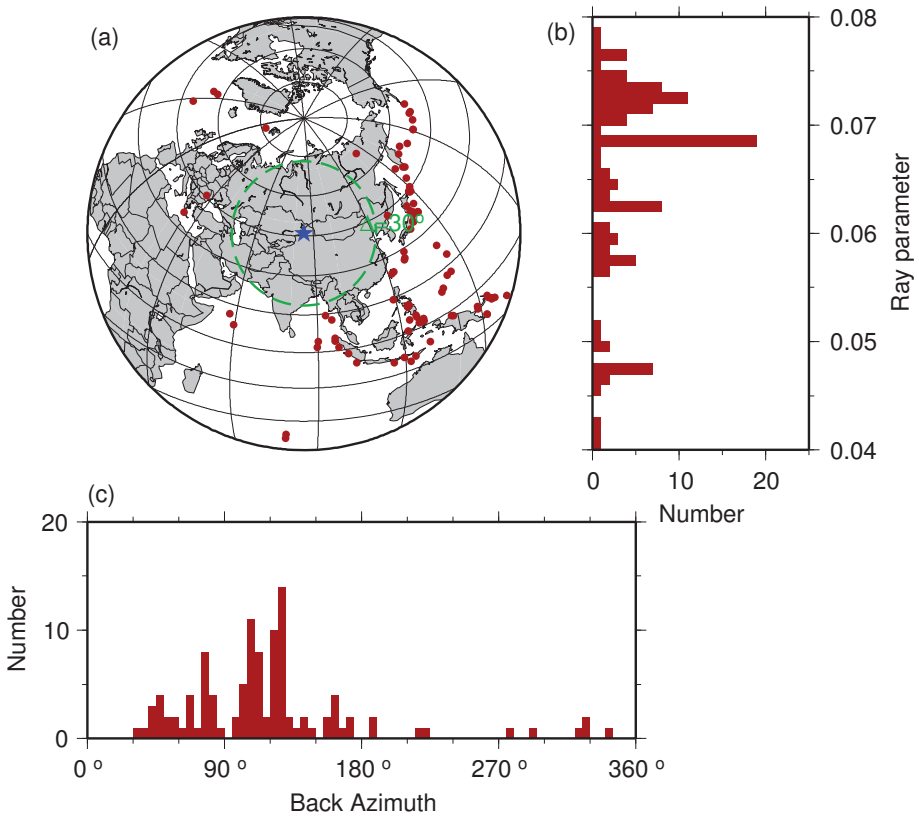

FIGURE 3.2: (a) Distribution of teleseismic events used in receiver functions. The dashed green line and outer boundary represent the 30° and 90° distances to the center of the study area marked by the blue star. (b) Distribution of ray parameter and (c) back azimuth for the events shown in (a).

3.3 Data and method

3.3.1 *P* wave receiver function

All the 31 portable broadband seismic stations (Figure 3.1) continuously recorded seismic data with a 40 Hz sampling rate from September 2013 to December 2013. Station location and the other information is presented in supplementary materials (Table 3.1). We select 109 earthquakes with the magnitudes larger than 5.0 Mb and the epicentral distances from 30° to 95° (Figure 3.2). All the waveforms of vertical components are visually inspected to ensure that only waveforms with good SNRs (> 5) are retained. Afterward, we remove linear trends, resample the waveforms to 10 Hz, and filter the data with a band-pass filter of 0.05 to 2 Hz. We use three component *P* wave waveforms windowed at 30 s before and 90 s after the direct *P* arrival. To calculate *P* wave receiver functions (pRF) at each station, we adopt the time domain iteration deconvolution [Kikuchi and Kanamori, 1982, Ligorria and Ammon, 1999]. A Gaussian low-pass filter is applied to the deconvoluted results to reduce noises above 1 Hz. For each station, all receiver functions are sorted by the back-azimuth and inspected to identify and remove bad ones. Finally, one station W10 (see Figure 3.1) is abandoned because the recorded seismic data by this station are very noisy. We obtain 556 good-quality receiver functions for the rest 30 stations, with the number of pRFs at each station ranging from 14 to 52. Receiver functions with similar back-azimuths and ray-parameters are stacked.

H-κ stacking

We adopt the H-κ stacking method [Zhu and Kanamori, 2000] to determine crustal thickness and κ (*Vp/Vs* ratio) for the stations in the areas with hard rock outcrops. The method uses the time delay of Moho converted phase *Ps* and its crustal multiphase *PpPs* and *PsSs* + *PsPs* to simultaneously determine the thickness *H* and *Vp/Vs* ratio while constraining the trade-off between these two parameters (Figure 3.3). In order to better constrain the *Vp/Vs* ratio, we use weighting factors of 0.5, 0.3, and 0.2 for the phases of *Ps*, *PpPs*, and *PsSs* + *PsPs* in the data processing. As illustrated in Figure 3.3, most of the H-κ stacking results show a reasonable quality. Results of all stations within mountain range and their uncertainties are listed in Table 3.2 in the supplementary material.

We then use receiver function inversion of neighborhood algorithm [Sambridge, 1999a,b] to obtain basin thickness beneath the stations in the basin area. A Haskell propagation matrix

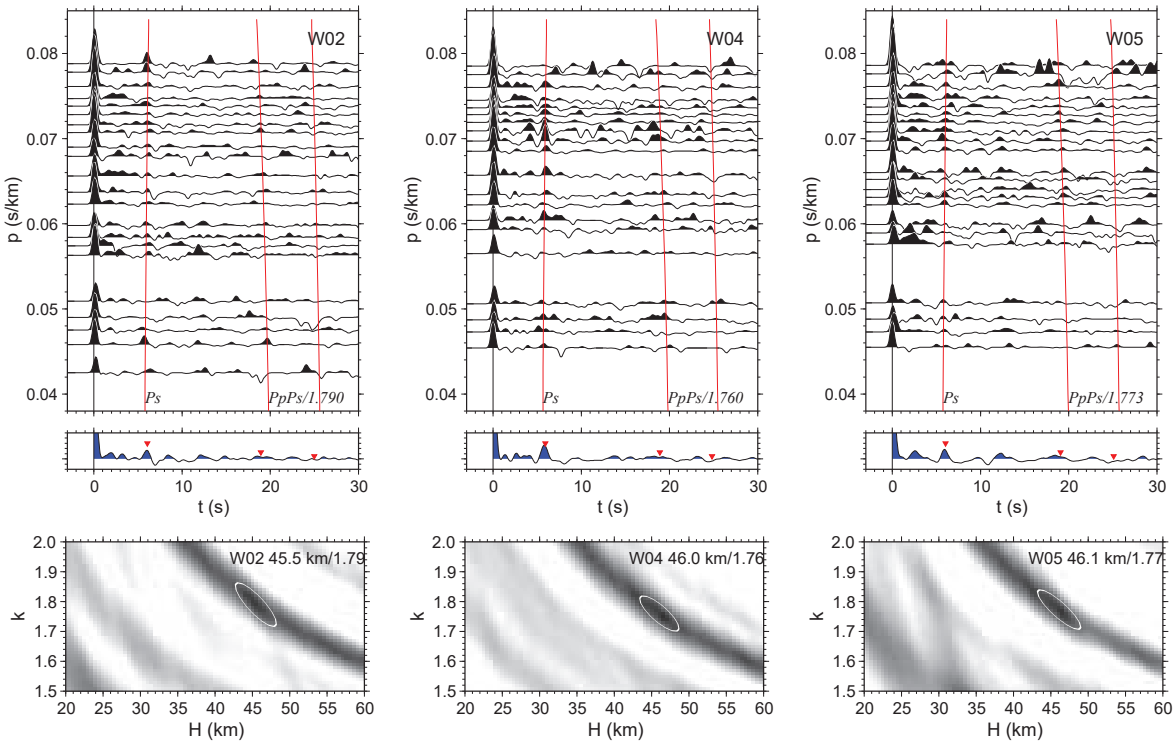

FIGURE 3.3: H-κ stacking results of station W02, W04, and W05 in the mountainous area. The receiver functions filled in blue in the middle panels indicate the stack traces by stacking all the traces shown in the top panels, and the red inverted triangles represent the arrivals of Ps and the multiples.

method is adopted to calculate the synthetic waveform of receiver functions [Haskell, 1964]. The algorithm begins to construct an initial model with a surface single layer underlain by a half-space. By varying the thickness and *Vp/Vs* ratio of the surface layer in a wide range, we can find a solution with the least misfit between calculated pRFs and synthetic ones, which results from the models with the velocities continuously increasing with depths in the basin zone (Figure 3.4). In the neighborhood algorithm inversion, we only focus on fitting the first 10 s of receiver functions as the sedimentary structure mainly affects the receiver functions at the first 10 s. In the process, we set the maximum basin depth to 10 km with a 0.2-km interval, and the *Vp/Vs* ratio in a range of 2.0 to 4.0 with a 0.1 interval. The *S* wave velocity is set in the range of 0.2 to 3.0 km/s for the top basin zone and 1.0 to 3.0 km/s for the bottom basin zone, respectively, both having a 0.1-km/s searching interval. Meanwhile, the ranges of *S* wave velocity and *Vp/Vs* ratio in the half-space are set to constants of 3.43 km/s and 1.75, respectively. Results of all stations within basin range and their uncertainties are listed in Table 3.3 in the supplementary material. Finally, we have the results of Moho depth and basin thickness for all stations as plotted as contours in Figure 3.5. The results of basin thickness and *Vp/Vs* ratio are then used to constrain the crustal structure in the following

common conversion point (CCP) stacking.

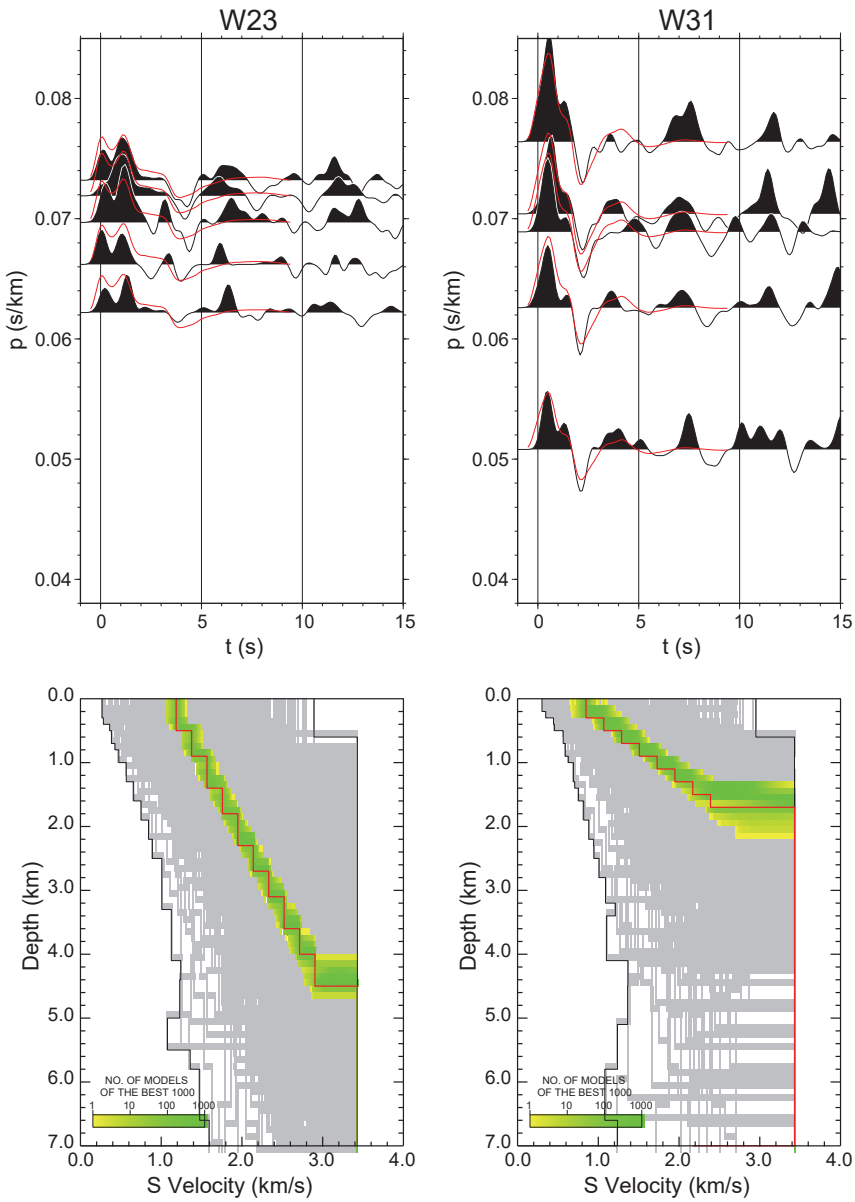

FIGURE 3.4: Results of the neighborhood algorithm inversion at the station W23 and W31 located in the basin area. The green area at the bottom panels shows the 1,000 *Vs* models with the lowest misfits among the entire sampled model space, which is the gray-shaded area. The red solid lines in the bottom panels indicate the best *Vs* models. The top panels display the waveform fits between observations (black) and synthetic receiver functions (red) based on the best models, that is, the red solid models shown at the bottom.

CCP stacking

To better illustrate the crustal structure in the region, we also use the CCP stacking method [Zhu, 2000] to image the lateral variations of Moho depth along three profiles AA' , BB', and CC', which are approximately perpendicular to the NE-SW trending Hatu, Darbut, and

K-U faults (Figure 3.1). We divide the crustal volume into 1-km-wide and 0.5-km-thick bins and stack all receiver function amplitudes in each bin by calculating the raypath of each pRF. We set different 1-D models by taking account of basin thickness and *Vp/Vs* ratio for the calculation of raypath at individual stations in the basin area. The stacked amplitude in each bin is proportional to the impedance contrast of velocity structure at the location of the bin. We use the first Fresnel zone size determined by $\lambda * z$ as the width of the ray, where λ is the wavelength and z is the depth, to determine the lateral resolution of the CCP image. The resolution varies from ~5 km in the upper crust to ~10 km at the Moho depths based on the values estimated by the dominant period of 1 s in the receiver functions. Figure 3.6 illustrates CCP imaging of profile AA' , BB' , and CC' by using pRFs of stations W4-W9, W11-W22, and W23-W29, respectively.

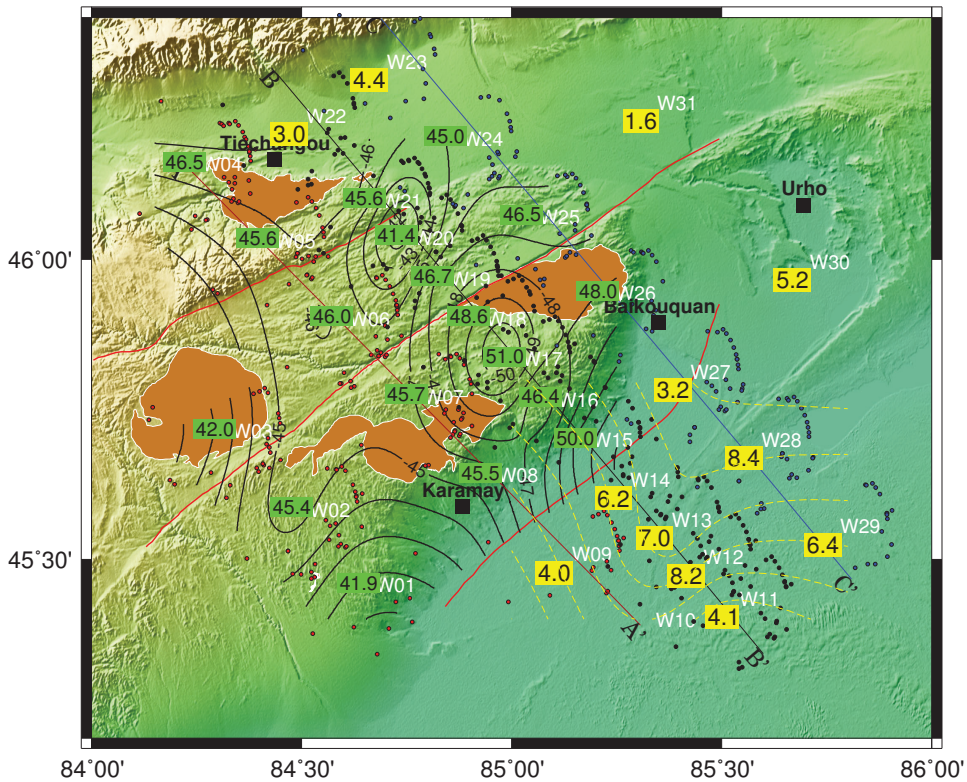

FIGURE 3.5: The Moho depths in the mountainous area and the depths of sedimentary basement in the basin areas shown as contours. The numbers in the green boxes and in the yellow boxes represent the Moho depth and basin thickness, respectively. All piercing points at the Moho are indicated by the small dots with colors, corresponding to the colors of their corresponding profiles.

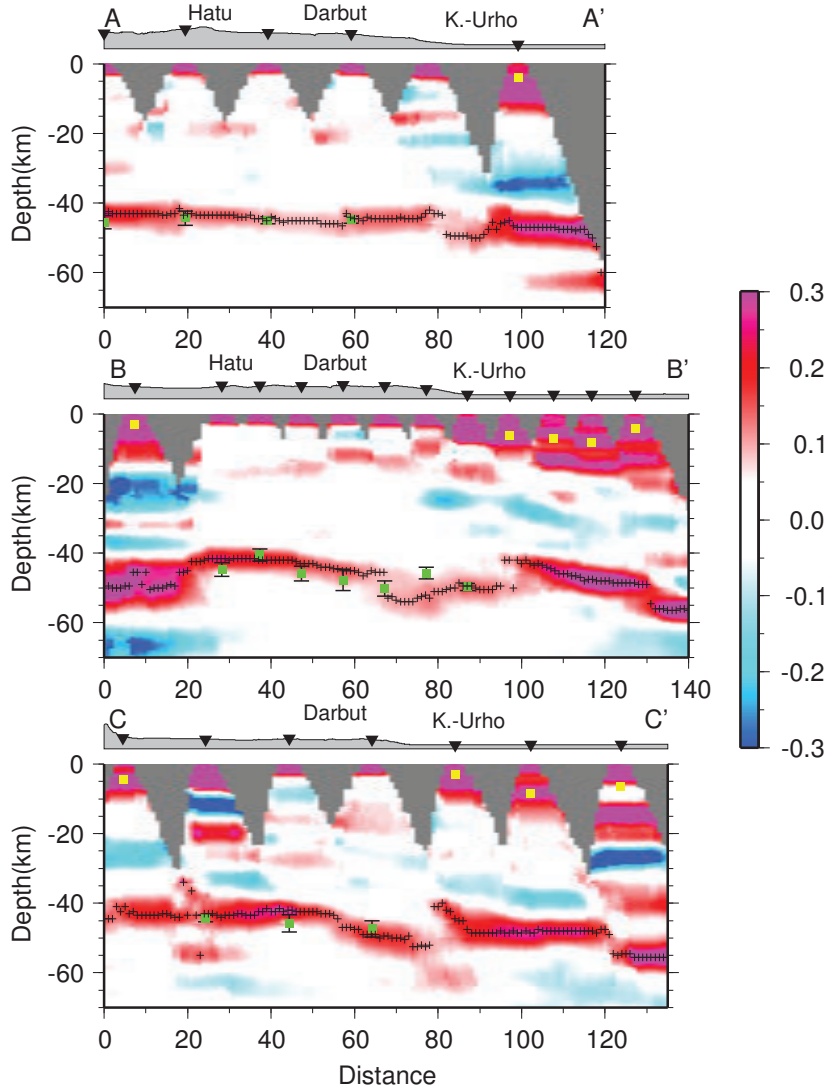

FIGURE 3.6: The common conversion point stacking images along the three profiles AA', BB', and CC' with their locations shown in Figure 1. The green boxes with error bars are results from H-κ stacking, the yellow boxes from the results of receiver function inversion of neighborhood algorithm, and the black crosses are the maximum amplitude peak along profiles.

3.3.2 Ambient noise tomography

Data processing and dispersion measurement

The data processing procedures of ambient noise tomography used here are similar to the workflow proposed by Bensen et al. [2007] except in the stacking stage. Raw continuous seismic data sampled at 40 Hz are first decimated into 5 Hz and the instrument responses are removed for each station. We then cut the continuous data into one-hour pieces and filter them using a bandpass filter of 1-30 s. After removing the mean and trend, we apply the running-average mean normalization in time domain and spectral whitening in

frequency domain to each hourly segment to diminish the influences caused by earthquakes or other irregularities and also normalize the frequency band of ambient noise. Finally, cross-correlations are performed on the hourly segments between each pair of stations, and then the hourly cross-correlations are stacked together to generate the final stacked cross-correlations using a method called tf-PWS [Schimmel et al., 2011]. Compared to linear stacking, tf-PWS stacking method improves the signal-to-noise ratio (SNR) of the stacked cross-correlations.

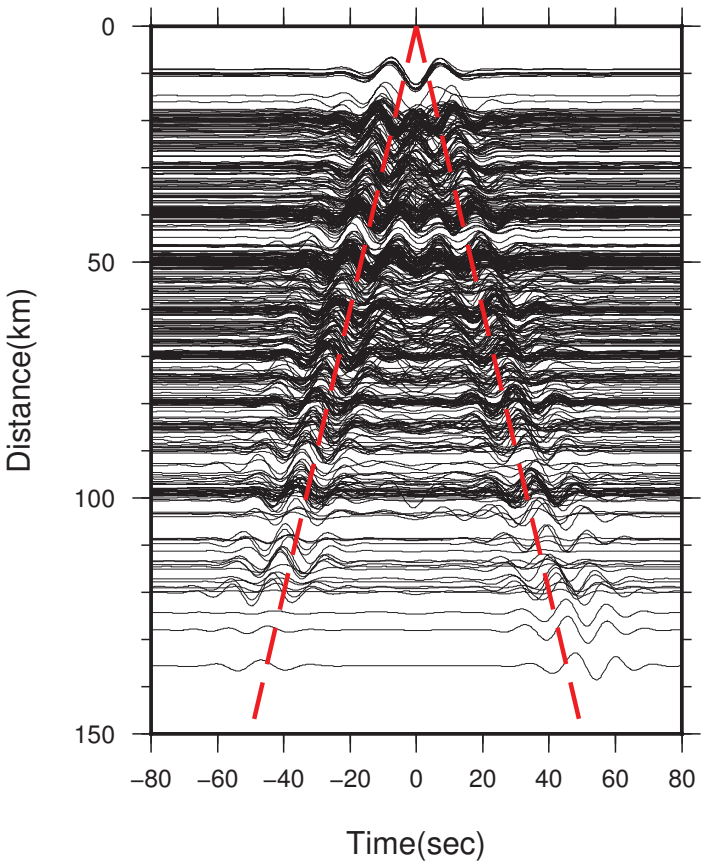

FIGURE 3.7: The stacked cross-correlations of vertical components between all station pairs, filtered at a 10-30 s period band.

As plotted in Figure 3.7, prominent Rayleigh waves emerge from Z-Z cross-correlations in both positive and negative lags. To enhance SNR, we cut and stack the two lags to construct the symmetric-component cross-correlations. Then, all the subsequent data analyses are carried out on the symmetric components. We adopt the frequency-time analysis technique (FTAN) [Levshin and Ritzwoller, 2001] to measure phase velocities from the symmetric cross-correlations. Luo et al. [2015] demonstrate that phase velocity measurements from cross-correlation with interstation distances as short as one wavelength are still reliable for tomography. Thus, in order to include more short-path data to improve path coverage and

resolution in tomography, we use one and a half wavelength distance cutoff in the selection of dispersion curves for the following ambient noise tomography. Due to the limitation of the aperture of our seismic array, the longest period of surface waves extracted from our array is 18 s, which limits the resolution of the shear velocity model to depths shallower than ~35-40 km. The SNR of cross-correlations is also a crucial criterion in the dispersion measurements. We only choose those dispersion measurements with the SNR of surface waves larger than 15. Here, SNR is calculated for each stacked cross-correlations by measuring the ratio of peak amplitude of surface wave signals relative to the root mean square (RMS) of trailing time series.

Phase velocity tomography

The selected phase velocity dispersion data are then inverted for phase velocity maps on a $0.1° \times 0.1°$ grid by an iterative, non-linear inversion method called Fast Marching Surface wave Tomography (FMST) which is developed by Rawlinson and Sambridge [2005]. This method applies a Fast Marching Method (FMM) [Rawlinson and Sambridge, 2005] for solving the forward problem and a subspace method [Kennett et al., 1988] to invert dispersion data. Damping (ϵ) and smoothing (η) regularization terms used to stabilize the inversion are chosen by carefully inspecting the trade-off curves between data and model variance. Rayleigh wave phase velocity maps are then generated at 4-18 s periods. Examples of phase velocity maps at 5, 10 and 15 s are illustrated in Figure 3.8.

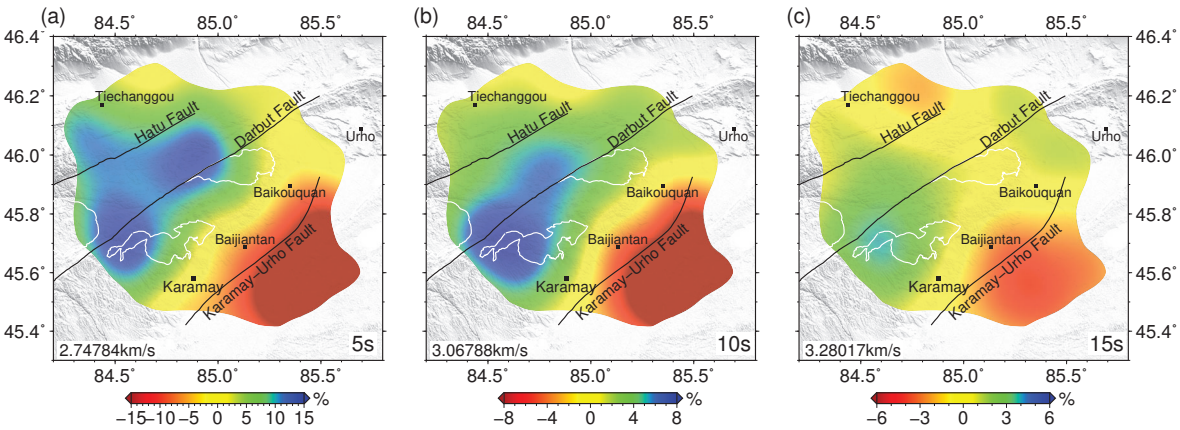

FIGURE 3.8: Examples of phase velocity maps at periods of 5, 10 and 15 s. The anomalies are relative to the average phase velocities shown at the left bottom of each image.

Synthetic checkerboard tests and uncertainty estimation are conducted to evaluate the resolution and uncertainties of phase velocity maps. Checkerboard tests are performed with

the anomaly sizes set to be $0.3° \times 0.3°$ and $0.2° \times 0.2°$ and the velocity perturbations set to be ±8% relative to an average of 3.0 km/s. Based on the same ray path coverage and the same $0.1° \times 0.1°$ grid node size as the real tomography, synthetic phase traveltimes are calculated and Gaussian noise with a zero mean and a 0.05 s standard deviation are added to the synthetic data. Then, inversions are performed with the same damping and smoothing factors as used in the real-data tomography. Uncertainties in phase velocity maps are estimated from the diagonal elements of the posteriori covariance matrix:

$$C_M = \epsilon[G^T C_d^{-1} G + \epsilon C_m^{-1}]^{-1}, \tag{3.1}$$

where G is the Fréchet matrix, ϵ is damping factor, C_d is *a priori* data covariance matrix and C_m is *a priori* model covariance matrix [Rawlinson et al., 2003]. Figure 3.9 presents examples of checkerboard resolution tests and uncertainty map at 10 s period and the checkerboard tests for other periods are shown in supplementary materials (Figure 3.14). The input velocity perturbations are recovered very well for both anomalies of $0.3° \times 0.3°$ and $0.2° \times 0.2°$. The uncertainties of phase velocity are around ~20 m/s in most regions covered by stations, and increase toward to the fringes of the seismic array.

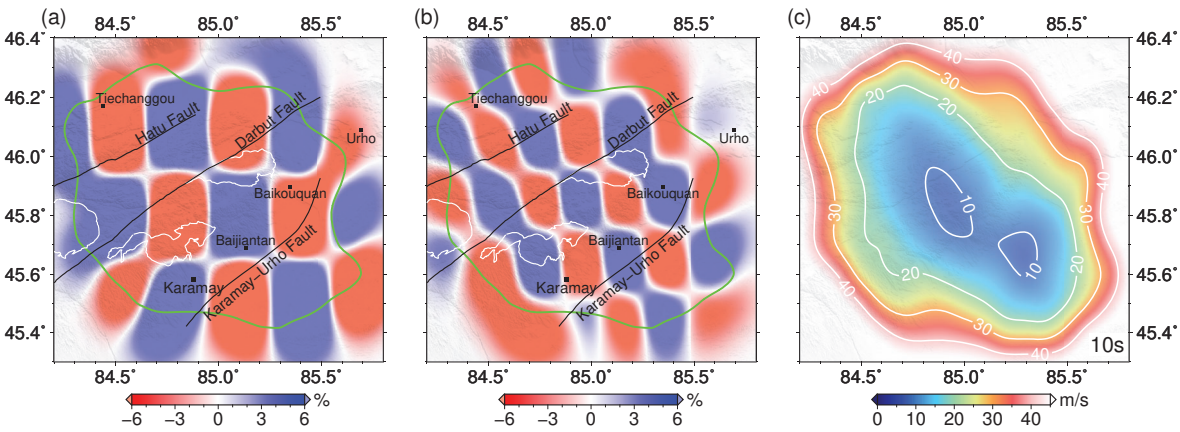

FIGURE 3.9: Synthetic checkerboard tests for 10 s period with the anomaly sizes of (a) $0.3° \times 0.3°$ and (b) $0.2° \times 0.2°$. Green contours in (a) and (b) indicate the boundary of the area with good resolutions. (c) The uncertainties of phase velocities at 10 s period.

Inversion for shear wave Velocity

Local phase velocity dispersion curves are extracted from the constructed phase velocity maps at each $0.1° \times 0.1°$ grid node at 4 to 18 s periods. Each local dispersion curve is inverted for a 1D shear wave velocity (Vs) profile. In this study, we adopt a Bayesian method

of Afonso et al. [2013a] to perform the 1D shear wave inversion. In this method, under the Bayesian framework, the solution to the inverse problem is given by a joint probability density function (PDF) in the parameter and data space, known as the posterior PDF [Guo et al., 2016b]. The posterior PDF describes a series of acceptable models, which fit the data and are consistent with prior information. A Delayed Rejection and Adaptive Metropolis (DRAM) algorithm [Haario et al., 2006] is applied to sample the posterior PDFs. Details of the inversion approach are given by Afonso et al. [2013a] and Guo et al. [2016b].

In our inversion, the parameterization of 1D *S*-wave velocity model is similar to that of Guo et al. [2016b]. Since our longest period of surface waves only reaches 18 s, which is sensitive to structures at depths shallower than 60 km, we parameter our 1D *Vs* model space with a thickness of 70 km consisting of one crustal domain and one upper mantle domain plus a sedimentary layer if necessary. Three parameters are used to describe the sedimentary layer, including the thickness and *S*-wave velocity at the top and bottom of the sedimentary layer. We assume that the *S*-wave velocity increases linearly with depth within the sedimentary layer. We use five B-splines in the crust and four B-splines in the upper mantle to describe the velocity variations in the crust and the upper mantle, respectively. Together with crustal thickness, there are total 12 or 15 (where sedimentary layer exists) free parameters for each 1D model. The searching range of prior *S*-wave velocities are set wide, ranging from 2.0 to 4.5 km/s in the crust and 3.6 to 5.5 km/s in the upper mantle, and the velocities are forced to increase across the Moho interface. The thickness of sedimentary layers in the western Junggar basin and the Moho depth included in the inversion are acquired from results of receiver functions. And both of them are allowed to vary ±2 km from the starting model. Since surface waves are mostly sensitive to *S*-wave velocity, we calculate *P*-wave velocity (*Vp*) and density from *Vs* based on the empirical relationship suggested by Brocher [2005]. In the sedimentary layer, *Vp/Vs* ratio is set to a constant of 2.0 and the density is scaled by the Gardner's rule [Gardner et al., 1974].

During each sampling, surface wave phase velocity dispersion is calculated based on the above parameters using a modified version of the MINEOS modes code [Masters et al., 2007]. After a total number of 240,000 samples, the last 3,000 accepted samples are kept and used to generate the statistics of posterior PDF. One advantage of this probabilistic inversion method is that *Vs* uncertainties can be estimated by calculating the standard deviation of the 3,000 accepted models.

An example of inversion at the grid point of 45.9°N, 84.9°E is illustrated in Figure 3.10 (another example of 1D inversion at grid point located in the basin range is presented in Figure 3.15). Predicted dispersion curves from inverted models fit observed dispersion curves very well. The inverted 1D model of all grid points are then combined to generate 3D shear wave velocity model of the study region. Shear wave velocity slices at different depths and three transects depicted in Figure 3.6 are plotted in Figure 3.11 and 3.12, respectively. The uncertainties of the *Vs* profiles beneath individual nodes are calculated.

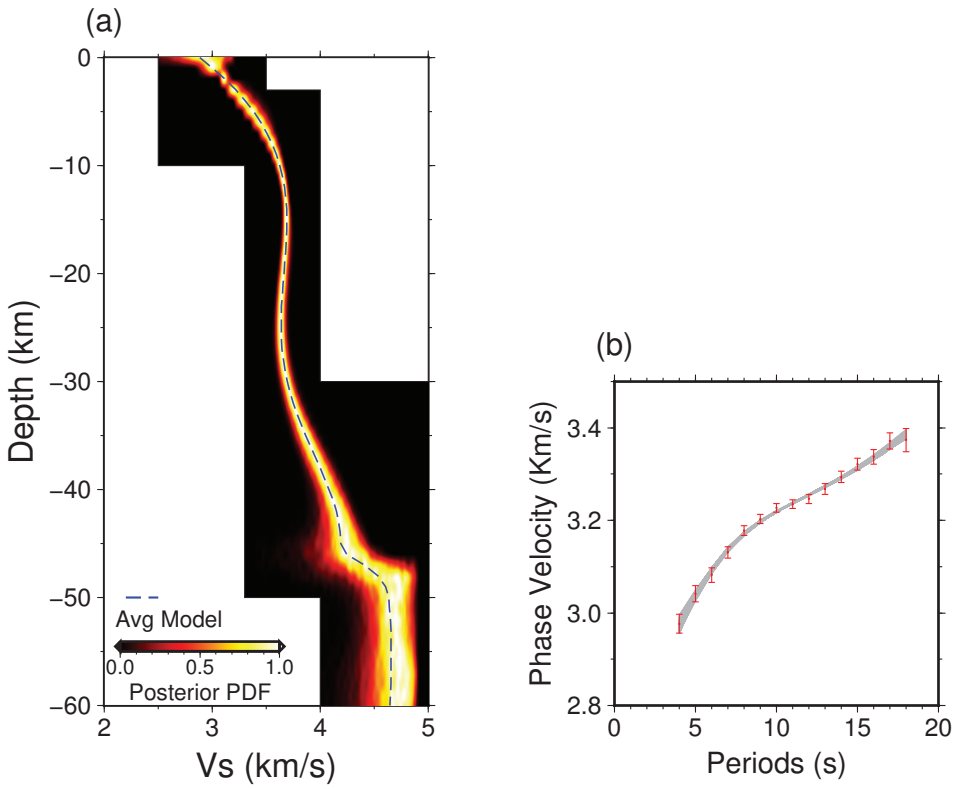

FIGURE 3.10: Example of the MCMC based Bayesian inversion at the grid point of 45.9°N, 84.9°E. (a) Inverted 1-D shear wave velocity model from the regional phase velocity dispersion curve shown in (b) with red error bars. Brighter zones in (a) represent a higher possibility of the *Vs* distributions and the blue dash line is the average *S*-wave velocity model. Grey curves in (b) are the dispersion curves calculated from the last 3000 accepted models. Note the good fits between the predicted dispersion curves from the final models and the observed dispersion curve.

3.4 Results

3.4.1 Crustal architecture from receiver functions

The H-κ stacking results (Figure 3.3) show strong variations of Moho depths in the mountainous area with an averaged crustal thickness of ~46 km, relatively thicker than global averaged

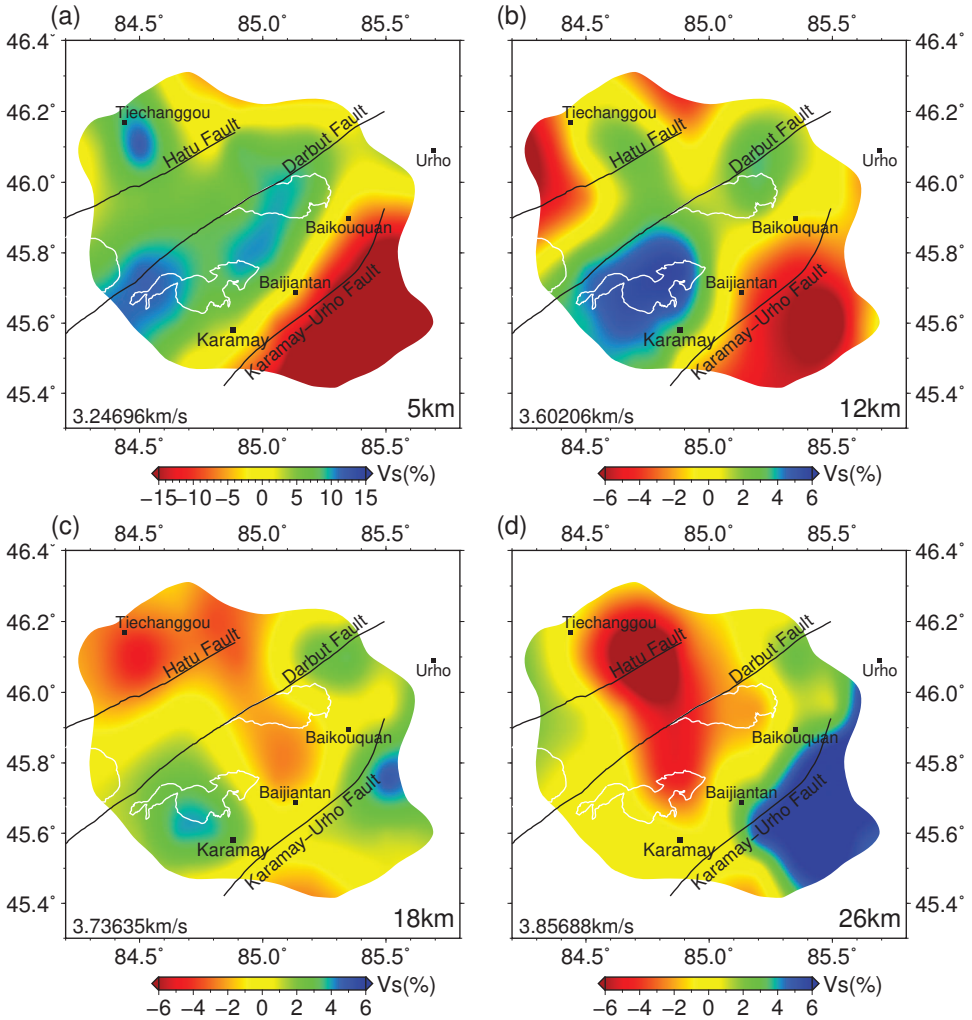

FIGURE 3.11: *S*-wave velocity maps of the western Junggar at the depths of 5, 12, 18 and 26 km. Major geological features are superimposed. Average *S*-wave velocities for individual depths are shown at the left bottom of each map.

value compiled by Mooney [2010]. The thickest crust in this region is in the area between the Karamay and Hongshan intrusions where the Moho depth reaches 51 km, and the thinnest crust of 41.9 km is in the southmost region.

Owning to the denser seismic stations along the three profiles (Figure 3.1), the Moho interface is clear and pronounced in the CCP images along all three profiles (Figure 3.6). Along profile AA', the Moho is relatively flat with a depth of ~42 km. Along profile BB', the deepest Moho is observed between Darbut and Karamay-Urho faults. Contrary to profile AA', a Moho offset is visible nearly beneath the Karamay-Urho fault, corresponding to the transition zone of basin and mountain areas. The CCP image of profile CC' shows the similar features as that of profile BB'. However, a larger Moho offset slightly migrates to the northwest of Karamay-Urho fault (Figure 3.6c), implying a possible change of dipping angle

along the Karamay-Urho fault.

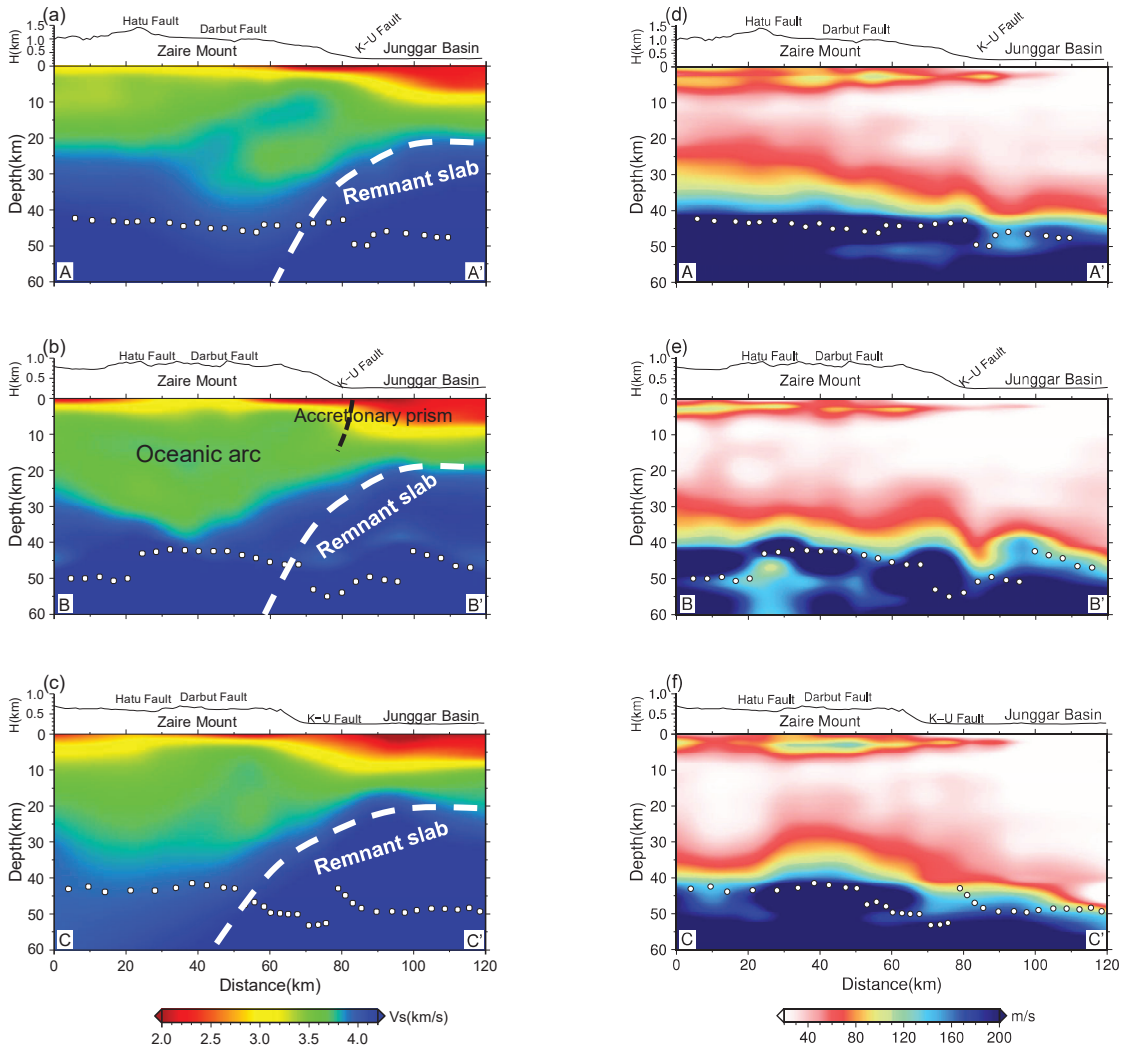

FIGURE 3.12: (a)-(c) Three vertical cross-sections of *S*-wave velocities along profile AA', BB' and CC' with their locations shown in Figure 3.1. (d)-(f) Corresponding uncertainties of *S*-wave velocities in the three transects. The interpretation of major velocity features is denoted in (b) with details discussed in the main text.

3.4.2 3D *Vs* model

Due to the limitation that the longest period of surface waves extracted from ambient noise is 18 s, the resolution decreases with depths and the uncertainties of shear velocity increase quickly at depths greater than ~30-40 km (Figure 3.12). To assess the robustness of our inverted velocity features, we plot the uncertainties of shear velocities accompanying the three *Vs* profiles in Figure 3.12. The uncertainties at depths over ~40 km reach ~0.2 km/s,

close to the range of lateral variations of our *Vs* model at these depths. Thus, we do not interpret the velocity structures below 40 km even though we plot our model up to 60 km depth in order to accommodate the Moho depths from receiver functions.

As shown in Figure 3.11 and Figure 3.12, large *Vs* contrasts are observed in the shallow crust between the Junggar basin and the Zaire mountain with the boundary following the hidden Karamay-Urho Fault (K-U fault). Low *Vs* anomalies dominate the upper crust beneath the Junggar basin with the velocities varying from ~1.5 km/s in the surface to ~3.0 km/s around 10 km depth. As surface waves are insensitive to sharp velocity boundaries, the exact thickness of the Junggar basin sedimentary layer cannot be well constrained. To the northwest of the K-U Fault, relatively high *S*-wave velocities (> 3.5 km/s) are seen in the upper crust beneath the Hongshan and Karamay intrusion (Figure 3.11). With depths increasing to ~15 km, the patterns of velocity anomalies are very different from those in the upper crust. Very high velocities (3.7 - 4.1 km/s) occupy most area beneath the Junggar basin, which is more pronounced in the three transects plotted in Figure 3.12. These high velocities are nearly flat under the Junggar basin but dip northwestward with depth as seen clearly in the transect BB'. Within the Darbut belt, ranging from the Karamay-Urho Fault to the Hatu Fault, intermediate velocities ranging from 3.0 - 3.5 km/s are observed in the center of Zaire mountain beneath the Darbut fault along three profiles.

3.5 Discussion

Although there is increasing evidence for a subduction dominated settings in the western Junggar by most recent studies [e.g., Ma et al., 2012, Xu et al., 2016, Yin et al., 2013, Zhang et al., 2011a,b, 2017], the detailed geometry of the subducting slab is still not imaged before. Our results of seismic imaging provide a good constraint on the geometry of a possible slab. In our tomographic model shown in Figure 3.12, the high shear-wave velocity body is nearly flat beneath the western Junggar basin and gradually dips northwestward with depths. This geometry of the high velocity body likely reveals a northwestward fossil subduction beneath the western Junggar, consistent with the interpretation of MT results that suggests a fossil oceanic subducting slab and a well-preserved intraoceanic arc system in the Darbut belt [Xu et al., 2016, Zhang et al., 2017].

In addition to examining the shape of high velocities, we also investigate if the value of

observed high velocities is consistent with the shear velocity of a remnant oceanic slab trapped in the crust with a typical chemical composition of mid-ocean ridge basalt (MORB). To do so, we compute the seismic velocity of several metamorphic facies of the MORB as well as that for an averaged global continental mid/lower crust and then compare the calculated velocities with the observed velocities at 15 - 35 km depths beneath the western Junggar. Following Hacker et al. [2003], we calculate the *S*-wave velocity for various stable metamorphic facies of MORB, such as greenschist, garnet amphibolite and garnet granulite facies, under the specific temperature and pressure beneath the western Junggar. As comparison, we also calculate the seismic velocity of a typical continental crust. The minerals of average continental middle and lower crust is calculated from the chemical composition suggested by Rudnick and Gao [2003] using CIPW normative mineralogy calculation program developed by Kurt Hollocher (Geology Department, Union College, Schenectady, New York). The temperature of the middle and lower crust in the western Junggar region is estimated by the average geothermal gradient of 21.3±3.7 °C/km as proposed by Rao et al. [2013] and the pressure is estimated based on the density given by the *S*-wave inversion.

We adopt the MATLAB toolbox developed by Abers and Hacker [2016], which allows the calculations of seismic velocity for a large range of crustal and upper mantle minerals at relevant pressure and temperature, to calculate seismic velocities of various metamorphic facies of MORB and the average continental crust. The calculated results are plotted in Figure 3.13. The inverted *S*-wave speed beneath the region with a possible remnant oceanic slab increase significantly across 15 km depth and become much higher than the speed of averaged continental mid-lower crust but are close to the calculated velocities of various metamorphic facies of MORB at depths over 20 km. This calculation suggests that the composition of the high velocity bodies are mostly mafic, similar to that of MORB, supporting the interpretation that this high velocity body under the western Junggar may represent parts of the remnant Paleo-Asia oceanic slab since the subduction failed in the late Paleozoic.

One thing we notice is that the thickness of high velocity layer beneath the west Junggar basin is about 25 km, much thicker than the typical oceanic crust of 7 - 10 km. In regardless of the uncertainties in defining the present-day crustal base, i.e. Moho discontinuity, the deviation in the crustal thickness is significant and must be addressed. We propose three possible causes: 1) the crustal thickness increases at the out-rise zone by plate bending, 2) the crust thickens through the subsequent lithosphere deformation, 3) the Moho is dynamic,

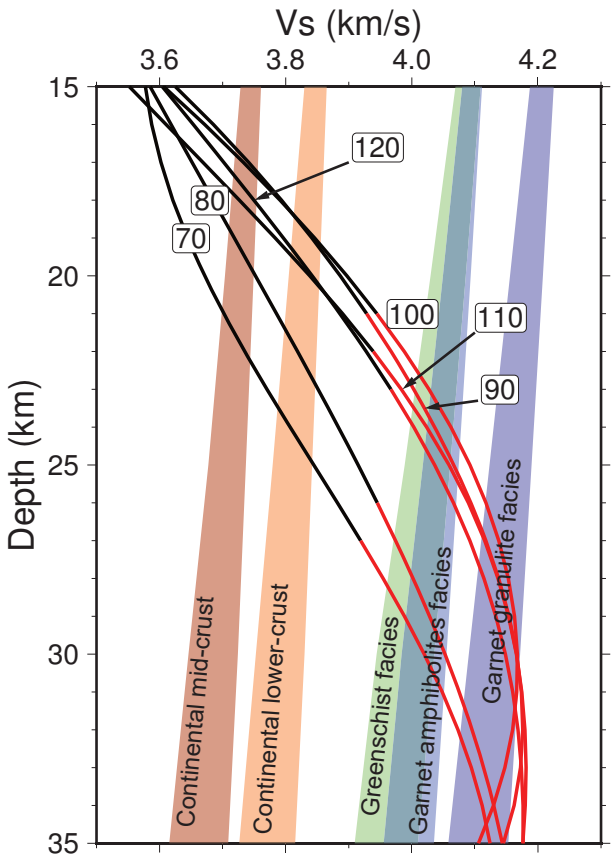

FIGURE 3.13: Observed 1D *Vs* profiles compared to the calculated Vs speeds of several metamorphic facies of the MORB and the averaged global continental mid-lower crust. These *Vs* profiles are extracted from BB' profile shown in Figure 3.12b with their locations denoted on the curves. The denoted numbers correspond to the x-axis (distance in km) in BB' profile shown in Figure 3.12b. Different color zones represent different rocks used for the velocity calculations. In general, colder colors represent more mafic rocks.

and the crust may be thickened by subsequent underplating of basaltic intrusions [O'Reilly and Griffin, 2013]. As has been widely identified that a large igneous province developed in the Tarim basin and Central Asian Orogenic Belt (CAOB) during the Permian [Yu et al., 2011, Zhang et al., 2010], the third mechanism in conjunction with the effect of plate bending is the most possible candidate to thicken the Moho beneath the western Junggar Basin. One more thing we also notice is that our result of Moho variations shown in Figure 3.6 does not reflect a northwest subduction, which could also be ascribed to the above mechanism, i.e., the underplating and cooling of basaltic intrusions could change the Moho dynamically [O'Reilly and Griffin, 2013].

The interpretation of a remnant oceanic slab for the high velocity body is also supported by our CCP imaging as shown in Figure 3.6, where a clear Moho offset is visible slightly

to the right beneath the Karamay-Urho fault (Figure 3.12b). This Moho offset is likely to be associated with the paleo-subduction interface. And, the Karamay-Urho fault can be interpreted as one of the major thrust fault separating the arc from the accretionary prism in the southeast. The intermediate velocity zone between the western Junggar basin and Zaire mountains (Figure 3.12) can be interpreted as the accretionary prism in the forearc, corresponding the depression zone of Moho interface.

Both of the 3D crustal model and the Moho variations revealed by receiver functions strongly supports the northwestward paleo-subduction zone model for shaping the western Junggar. Based on a presumption that the basement of Junggar basin was a continental block, Chen et al. [2014] suggested the entire Darbut belt is a remnant ocean basin. However, the velocity features as described before do not support their model. Moreover, most geochemical studies suggested that there may exist an oceanic ridge-related subduction during late Paleozoic [Choulet et al., 2012, Tang et al., 2010, Zhang et al., 2011a,b]. However, our velocity model is too shallow to rule out the possibility. Deep imaging with a broader seismic array is required in the future in order to investigate if the subduction is a ridge-related subduction or not.

3.6 Conclusions

In this study, we deploy a regional-scale seismic array consisting of 31 stations in Western Junggar, Xinjiang, northwestern China. We conduct *P*-wave receiver functions to determine Moho depths beneath all stations using the H-κ stacking method and image the Moho variations along three profiles using the CCP stacking method. We also perform ambient noise tomography to construct a 3D model of crustal shear velocities. Our results show that the Moho depths range 41 - 52 km with an average of 46 km. In the transition zone of the Zaire mountains and the western Junggar basin, the Moho is markedly depressed, probably associated with the paleo-subduction interface. The *Vs* model reveals strong vertical variations of seismic speed beneath the western Junggar Basin with the high velocity mid/lower crust underlying the low velocity upper crust. The high velocity body in the mid/lower crust extends and dips northwest into the Zaire Mountains. The speed of this high velocity body is matched with the calculated seismic speed of various metamorphic facies of MORB. We suggest that the northwest dipping high velocity bodies may be a remnant of Paleozoic oceanic slab and

the regions of Zaire mountains and western Junggar basin is a well-preserved subduction system which had developed before the Carboniferous and failed in the late Paleozoic [Xu et al., 2016].

3.7 Supplementary materials

Network	Station name	Longitude (°E)	Latitude (°N)	Elevation (m)
WJ	W01	84.6336	45.4568	636.974
WJ	W02	84.4763	45.5837	985.927
WJ	W03	84.2923	45.7144	1207.29
WJ	W04	84.22	46.1584	1011.99
WJ	W05	84.3948	46.0323	1286.92
WJ	W06	84.5713	45.9028	1053.4
WJ	W07	84.7483	45.7722	969.454
WJ	W08	84.9245	45.6412	434.901
WJ	W09	85.0998	45.5096	271.032
WJ	W10	85.30025	45.3996	280
WJ	W11	85.499	45.4335	283.597
WJ	W12	85.4135	45.5048	268.562
WJ	W13	85.3375	45.5673	268.316
WJ	W14	85.2395	45.6336	265.657
WJ	W15	85.1499	45.7	292.017
WJ	W16	85.0676	45.7676	663.633
WJ	W17	84.982	45.8346	835.545
WJ	W18	84.8971	45.9019	907.767
WJ	W19	84.8109	45.9687	865.543
WJ	W20	84.7248	46.036	868.149
WJ	W21	84.6477	46.0976	895.236
WJ	W22	84.4685	46.2384	796.112
WJ	W23	84.6598	46.3278	720.111
WJ	W24	84.8411	46.2007	607.287
WJ	W25	85.023	46.0714	671.03
WJ	W26	85.2047	45.9441	624.318
WJ	W27	85.382	45.8136	260.998
WJ	W28	85.551	45.7003	272.362
WJ	W29	85.7386	45.5564	281.302
WJ	W30	85.6668	45.9974	311.884
WJ	W31	85.303	46.2598	474.494

Table 3.1: Information for seismic stations used in the chapter 3.

Station	lat/lon/dep	Num. of RF	Tps	H(km)	κ(Vp/Vs)
W01[3222]	45.5/ 84.6/636	14	5.7	41.9±2.6	1.82±0.07
W02[3470]	45.6/ 84.5/985	36	6.0	45.4±1.5	1.80±0.04
W03[3126]	45.7/ 84.3/1207	26	6.0	42.0±1.8	1.86±0.06
W04[3140]	46.2/ 84.2/1011	42	5.8	46.5±1.9	1.75±0.04
W05[3474]	46.0/ 84.4/1286	34	5.9	45.6±2.0	1.78±0.04
W06[3142]	45.9/ 84.6/1053	34	6.1	46.0 -	1.79 -
W07[3137]	45.8/ 84.7/969	36	6.0	45.7 -	1.79 -
W08[3162]	45.6/ 84.9/434	52	5.6	45.5±1.6	1.75±0.03
W15[3070]	45.7/ 85.2/292	23	6.6	50.0 -	1.79 -
W16[2227]	45.8/ 85.1/663	19	6.5	46.4±1.7	1.85±0.05
W17[2223]	45.8/ 85.0/835	27	6.0	51.0±2.2	1.70±0.05
W18[3136]	45.9/ 84.9/907	35	6.1	48.6±3.1	1.75±0.06
W19[3129]	46.0/ 84.8/865	21	5.8	46.7±2.1	1.75±0.04
W20[3464]	46.0/ 84.7/868	28	5.7	41.4±1.7	1.84±0.04
W21[3466]	46.1/ 84.6/895	43	5.7	45.6±2.0	1.75±0.04
W24[2219]	46.2/ 84.8/607	29	5.9	45.0 -	1.79 -
W25[2213]	46.1/ 85.0/671	31	5.7	46.5±2.5	1.74±0.05
W26[2222]	45.9/ 85.2/624	26	6.5	48.0±2.3	1.82±0.07

TABLE 3.2: Station locations and crustal thickness from H-κ and *Vp/Vs* estimates.

Station	Thickness(km)	Vs1(km/s)	Vs2(km/s)	κ(Vp/Vs)
W09[2216]	4.0	0.6	3.0	2.06
W11[3143]	4.1	0.9	3.0	2.11
W12[3163]	8.2	1.3	2.0	2.14
W13[2214]	7.0	1.0	2.1	2.14
W14[3152]	6.2	1.1	3.0	2.65
W22[3113]	3.0	0.7	3.0	2.00
W23[2226]	4.4	1.1	3.0	2.16
W27[3469]	3.2	0.9	3.0	2.00
W28[3215]	8.4	1.0	2.8	2.00
W29[3463]	6.4	0.8	1.9	2.00
W30[3138]	5.2	0.9	3.0	2.24
W31[3139]	1.6	0.7	2.5	2.14

TABLE 3.3: Station locations and sedimentary layer thickness from neighborhood algorithm and *Vp/Vs* estimates. Vs1 and Vs2 represent the *Vs* at the top and bottom of the sedimentary layer.

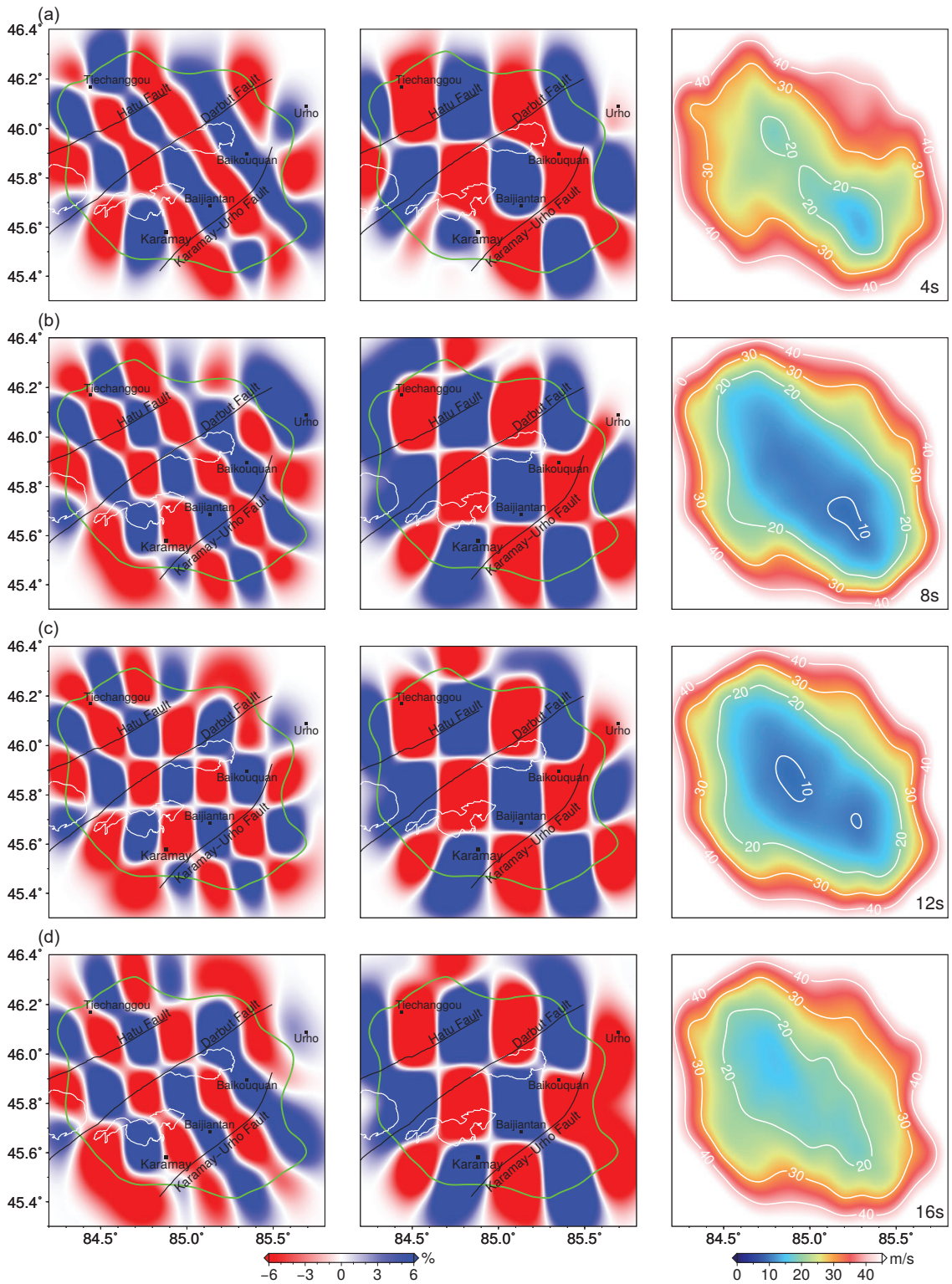

FIGURE 3.14: Synthetic checkerboard tests for (a) 4s, (b) 8s, (c) 12s, and (d) 16s with the anomaly sizes of 0.2° × 0.2° (left column) and 0.3° × 0.3° (middle column). Green contours indicate the boundary of the area with good resolutions. The uncertainties of the phase velocity at corresponding periods are plotted in the right column.

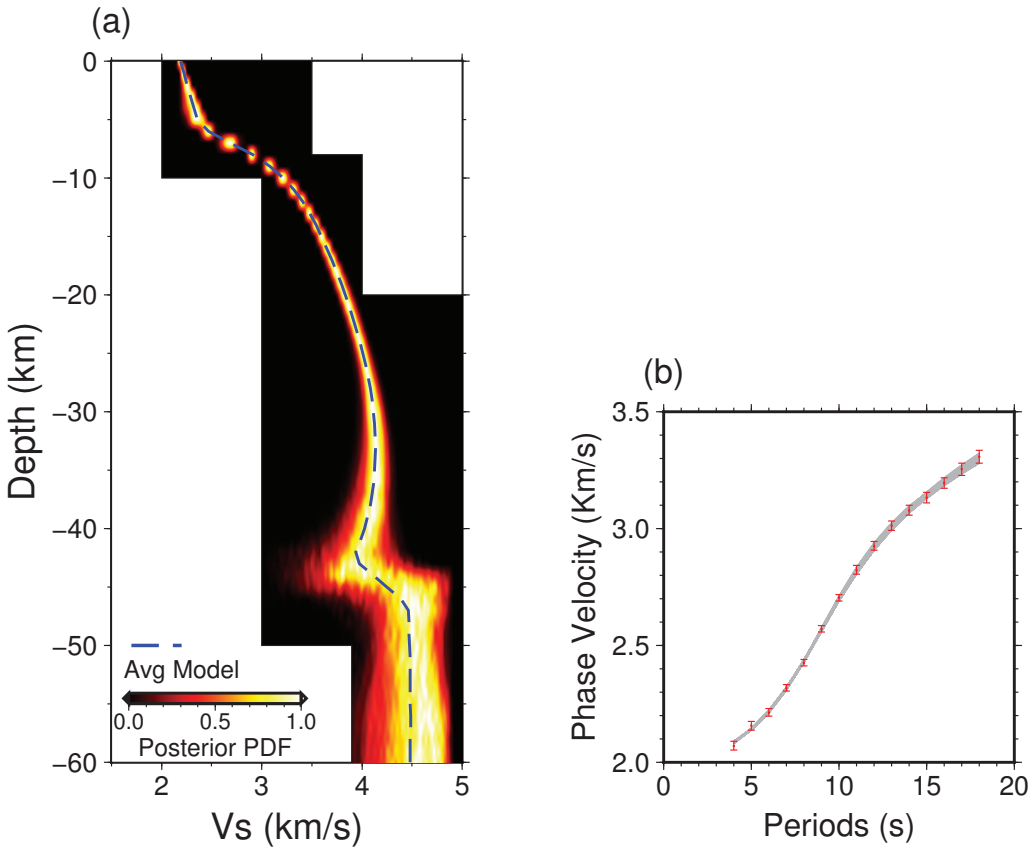

FIGURE 3.15: Example of the MCMC based Bayesian inversion at the grid point of 45.5°N, 85.3°E located in the basin. (a) Inverted 1-D shear wave velocity model from the regional phase velocity dispersion curve shown in (b) with red error bars. Brighter zones in (a) represent a higher possibility of the *Vs* distributions and the blue dash line is the average *S*-wave velocity model. Grey curves in (b) are the dispersion curves calculated from the last 3000 accepted models. Note the good fits between the predicted dispersion curves from the final models and the observed dispersion curve.

4

Imaging the Fossil Subduction Slab in the Junggar Region, Northwest China

4.1 Summary

The Junggar terrain is one of the most intriguing place to study the accretionary orogenic processes as multiple subduction systems are believed to operate the Junggar during Paleozoic time. The lack of significant subsequent tecto-thermal events makes it possible for us to image the Paleo-subduction structure through geophysical approaches. A regional seismic array consisting 49 stations were deployed across the Junggar terrain and a 3D *S*-wave velocity model of the crust and upper mantle are constructed. Our model shows that the Junggar basin is underlain by a high-velocity body and this high-velocity body gradually dips towards northwest with depth beneath the Zaire mountains (western Junggar). We interpret the high-velocity anomaly as the trapped fossil oceanic lithosphere with its last stage of subduction preserved beneath the western Junggar. The geometry of the trapped slab demonstrates the

subduction polarity in the western Junggar before the subduction terminate is northwestard. The high *Vs* anomaly disappears beneath the western Junggar at depths over ~150 km, this feature could be explained by a slab break-off model and/or a possible mid-ocean ridge subduction model during the late Carboniferous time.

4.2 Introduction

Modern style subduction tectonics may begin at the late Proterozoic [Stern, 2005] or as early as the Archean times [Smithies et al., 2007]. The sinking of cold and dense oceanic lithosphere, which directly pull the attached plate and also cause mantle convections, are thought to be the main driving force of the plate tectonics throughout Earth's history [Conrad and Lithgow-Bertelloni, 2002]. The present-day subducting oceanic lithosphere is characterized by high seismic velocities globally, such as the western Pacific subduction zones along the eastern coast of Japan [van der Hist et al., 1991, Zhang et al., 2004, Zhao et al., 1992], the Cascadia subduction zone in the northwestern coast of US [Calkins et al., 2011, Porritt et al., 2011] and etc. Similarly, some fossil oceanic lithospheres, although subducted a long period of time ago, can still be recognized by high velocity anomalies through a variety of tomographic techniques [Gorbatov et al., 2000, Jiang et al., 2018, Sol et al., 2002, Van der Voo et al., 1999]. Studying these fossil subductions can provide very important clues for reconstructing the past tectonics.

The Central Asian Orogenic Belt (CAOB), also known as the Altaids, is one of the world's largest accretionary orogeny which is believed to grow from 1.0 Ga [Khain et al., 2002] to about 250 Ma when the Paleo-Asian ocean closed [Windley et al., 2007]. Bounded by the Siberian Craton in the north, the East European Craton in the west, the Tarim and North China blocks in the south, this wide range orogenic collage offers an ideal place to study the process of accretion and continental growth throughout the Earth's history [Jahn, 2000, Şengör et al., 1993, Xiao et al., 2015b, Yakubchuk, 2004]. Although numerous studies have been published on the evolutionary history of central Asia, the mechanism of the accretionary growth during the closure of Paleo-Asian ocean is still a subject of controversy [Han et al., 1997, Han and Zhao, 2017, Yakubchuk, 2004].

The Junggar region of northwestern China (Fig. 1.1b), seated in the southern margin of the CAOB, is characterized by a triangular shaped Junggar basin in the center (~134,000 km^2)

with lens of Paleozoic ophiolites and granitoids present at the margins of the basin [Xiao et al., 2008, Zheng et al., 2007]. Since the excellent exposure of ophiolites, magmatic arcs and accretionary wedges [Xiao et al., 2015b], this region is regarded as one of the most crucial area in the CAOB to investigate the subduction, accretion and collision processes during the late Paleozoic times and can potentially provide important clues on the final stage of the accretionary processes of the entire CAOB. Previous studies all indicate complex multiple subductions accompanied with different types of intracontinental arc and/or intraoceanic arc systems developed in the Junggar region at the Paleozoic time [Choulet et al., 2016, Liu et al., 2016, Yin et al., 2013, Zhang et al., 2011a]. However, it is still not clear about the polarity of the subductions, the nature of basement beneath the Junggar basin and the possible existence of a ridge subduction in the western part of Junggar [Geng et al., 2009, Ma et al., 2012, Xiao et al., 2008, Zhang et al., 2011a,b]. Because the lack of subsequent tecto-thermal events in the western Junggar region, the detailed geometry of the fossil subduction system in this specific region may be preserved since the last subduction and thus it is possible to investigate the nature of past subduction system using geophysical approaches. Previous studies of magnetotelluric [Xu et al., 2016] and ambient noise tomography [Wu et al., 2018] both indicate an ancient intraoceanic arc and a trapped oceanic slab are well preserved in the crust of the western Junggar region since the subduction failed in the late Paleozoic. However, a high-resolution model of the upper mantle structures is not viable due to the lack of board and dense arrays in this region. Imaging the possible subducted slab in the upper mantle is vital to inspect whether the stagnant slab is still trapped in the upper mantle or has detached and sunk to greater depths. Building a model of the upper mantle structures will allow us to further determine the final subduction mode in the Junggar terrain.

As a commonly used technique, surface wave tomography has become a well-established approach to image lateral heterogeneities and anisotropy of the Earth's interior for multiple scales [Jiang et al., 2014, Lin et al., 2008, Shapiro and Ritzwoller, 2002, Trampert and Woodhouse, 1996, Yang and Forsyth, 2006a,b, Zhou et al., 2006]. With the widely applied passive and teleseismic tomography, regional shear wave velocity (*Vs*) anomalies can be well constrained. The combination of Ambient noise tomography (ANT) and Two-plane surface wave tomography (TPWT) has shown its advantage in producing high-resolution *Vs* structures of crust and upper mantle beneath regional scale seismic arrays [Guo et al., 2016b, Yang and Forsyth, 2006a, Yang et al., 2008, 2011b]. In this study, we apply ANT and TPWT

to a regional seismic array in the Junggar region to invert for the crustal and upper mantle 3D velocity structures.

4.3 Data and method

In chapter 3, we imaged the crustal structures based on data from a relatively small seismic array deployed in the western Junggar region (Fig. 3.1). Here, to image mantle velocity structures, a new seismic array is designed occupying a larger spatial region across the Junggar terrain (Fig. 4.1). This array consist of 28 newly deployed broadband seismic stations from July 2016 to September 2017 and 21 permanent stations from China Earthquake Administration (CEA) Array (Fig. 4.1). ANT and TPWT analyses are carried out from the continuous seismic data and the selected events based on data from these 49 seismic stations.

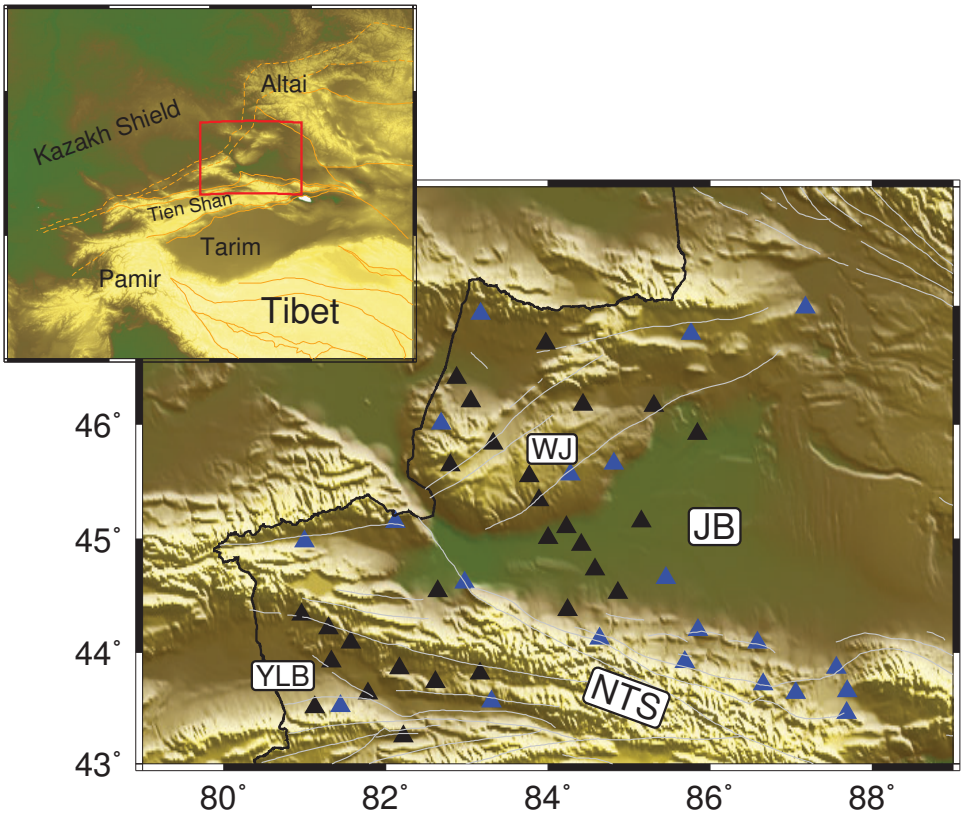

FIGURE 4.1: Location of the study region (red rectangle) and the broadband seismic stations. Blue triangles represent the 21 fixed stations from CEA and black triangles indicate the 28 deployed stations. Tectonic blocks around study region are outlined by orange lines, gray solid lines are the location of major faults, and the black solid line is the Chinese national border. WJ: West Junggar (or the Zaire mountains); YLB: Yili Block; JB: Junggar Basin or Dzungarian Basin; NTS: Chinese northern Tien Shan (or the Borohoro Mountains).

4.3.1 Ambient noise tomography

We follow the data processing procedures of ANT as described by Bensen et al. [2007]. Because several different types of sensors are mounted in different stations in this array, instrument responses are firstly removed from each station. Then, continuous seismic data are decimated from 40 Hz to 1 Hz, bandpass filtered to 3-150 s and cut to one-day segments for subsequent processing. To reduce the influences caused by earthquakes and/or other irregularities, we apply a running absolute mean time-domain normalization to each daily segment. As the amplitude spectra of ambient noise are generally not flat, spectral whitening is also performed to flatten the interested period band of ambient noise signals. After all these steps, cross-correlation is carried out on daily basis between each station pairs. Finally, all the daily cross-correlations are stacked by a time-frequency domain phase-weighted stacking (tf-PWS) approach based on S transform [Li et al., 2018, Schimmel et al., 2011]. The tf-PWS can be formulated as:

$$S_{pws}(\tau, f) = |c_{ps}(\tau, f)|^{\nu} \frac{1}{N} \sum_{j=1}^{N} S_j(\tau, f), \tag{4.1}$$

where $c_{ps}(\tau, f)$ with a power ν is a coherence dependent weighting term that vary from 0 to 1, N and j represent the total number and index of trace, $S_j(\tau, f)$ denotes the elapse time spectrum for jth trace at elapse time τ and it is calculated through the generalized S transform. The $S_{pws}(\tau, f)$ function is then transformed back to the time domain to generate the stacked trace by the frequency domain inverse S transform. Detailed description about this tf-PWS technique can be found at Li et al. [2018]. Because this stacking technique measures the signals that are more phase coherent, it has a great advantage over traditional linear stacking when dealing with weak signals in cross-correlations and can boost signal-to-noise ratio (SNR) remarkably. Fig. 4.2a shows an example of record section of cross-correlations using only vertical components. Due to the uneven distribution of the ambient noise sources, cross-correlations are usually asymmetric. We generate the so-called 'symmetric component' [Bensen et al., 2007] by further stacking the positive and negative lags.

Owning to smaller uncertainties, phase velocity measurements are superior over the group velocity measurements [Bensen et al., 2007, Luo et al., 2015, Yang et al., 2008]. Thus, phase velocities of the symmetric cross-correlations are measured by adapting a frequency-time analysis technique (FTAN) [Levshin and Ritzwoller, 2001]. In FTAN, group velocities are firstly measured by applying a Gaussian narrow band filter to the cross-correlations and

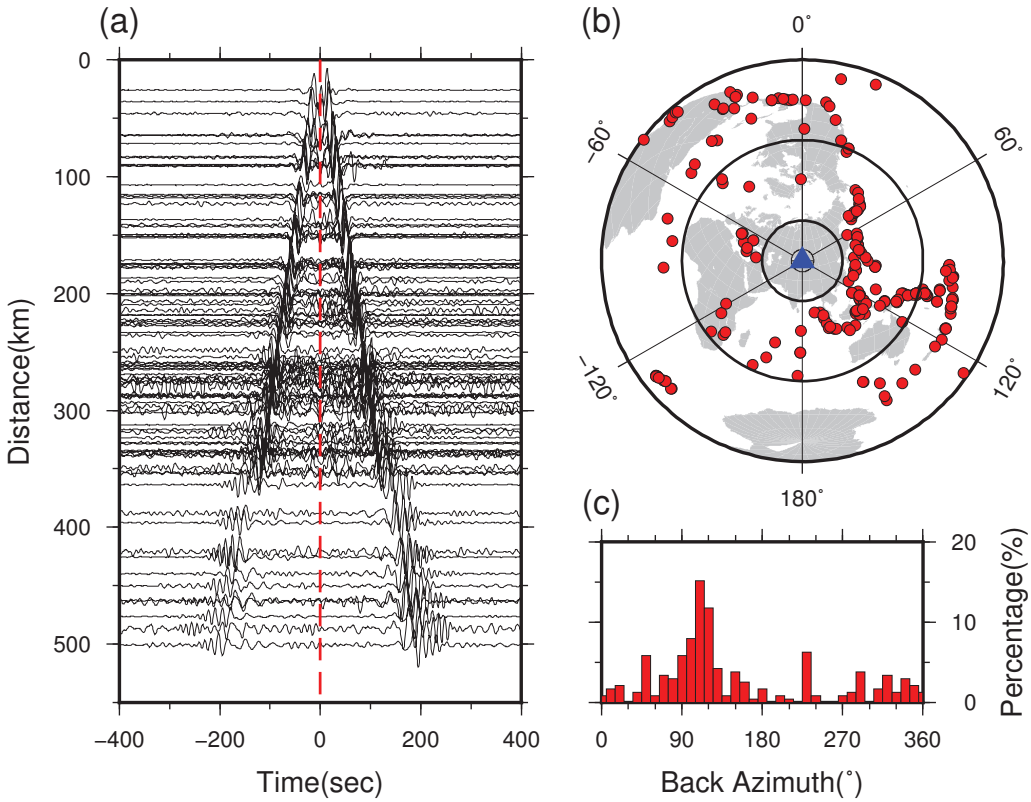

FIGURE 4.2: (a) Cross-correlations between station S04 and all the other stations, a bandpass filter between 8 s and 50 s is applied here for displaying purpose. (b) Distribution of 238 events used for two-plane surface wave tomography at period of 30 s. (c) Histogram of back azimuth distribution of the tele-seismic events in (b).

calculate the ratio between the interstation distance (r) and the arrival time (t_{max}) of the peak amplitude. Then, phase velocity at instantaneous frequency ω can be calculated by [Lin et al., 2008]:

$$c = \frac{r\omega}{\varphi(t_{max}) + \omega t_{max} - \pi/4 - 2\pi \cdot N - \lambda}, N = 0, \pm 1, \pm 2, \cdots, \tag{4.2}$$

where λ is the initial phase, $2\pi \cdot N$ represents the intrinsic phase ambiguity term, $\varphi(t_{max})$ is the phase of the estimated Green's function observed at time t_{max}, and $\pi/4$ is a phase correction term. To account for the intrinsic ambiguity problem here (i.e. the selection of N), a GDM52 global surface wave dispersion model [Ekström, 2011] is applied as a reference model when measuring phase velocities.

Quality control of the phase velocity measurements is essential. In this study, only those cross-correlations with SNR larger than 10 are retained. Here, it should be noted that SNR is period dependent and calculated as follows. A series of Gaussian narrow band filters centred at each individual periods are first applied to cross-correlations, SNR is then estimated for each of the band-bass filtered cross-correction by taking the ratio of the peak amplitude of

the filtered signals and the root-mean-square of the tailing noise. Another crucial criterion is the cutoff of the interstation distance. Usually, interstation distances of cross-correlations are required to be longer than three wavelengths. However, a recent study of Luo et al. [2015] on USArray data demonstrates that high-quality phase velocities can be measured by FTAN from cross-correlations with interstation distance as short as one wavelength. By relaxing the threshold of interstation distance, ray path coverage can be significantly enhanced, which can lead to an improvement of resolution. Conservatively, we choose 1.5 wavelengths as the cutoff of the inter-station distance for our dataset. Third, only measurements coherent with others are accepted. A smoothed tomographic model is used to test if phase velocities are coherent with each other. Any data with phase traveltime misfits larger than 6 s are discarded during this procedure. Furthermore, all the measurements are visually inspected to guarantee the reliability of our phase velocity measurements. After all these data selection steps, a total number of 655 paths at 10 s period and 898 paths at 20 s period are retained.

We adopt a fast marching surface wave tomography (FMST) method developed by Rawlinson and Sambridge [2005] in inverting the selected phase velocity measurements for 2D phase velocity maps on a $0.25° \times 0.25°$ grid. A grid-based numerical algorithm called fast marching method (FMM) [Rawlinson and Sambridge, 2005] is adopted in FMST for the forward calculation. This algorithm is a rapid and robust scheme for directly solving the eikonal equation using finite differences [Rawlinson and Sambridge, 2005]. Traveltimes to every point on a grid can be calculated through FMM approach and this makes the FMM superior to traditional ray-tracing methods. To solve the inverse problem, a subspace inversion scheme [Kennett et al., 1988] is adapted in FMST to tune the model parameters to satisfy the observed traveltimes with regularization constraints. In detail, the inversion can be formulated as minimizing an objective function $S(m)$ shown below [Rawlinson et al., 2003]:

$$\begin{aligned} S(m) &= \frac{1}{2}[(\mathbf{g}(\mathbf{m}) - \mathbf{d}_{obs})^T \mathbf{C}_d^{-1} (\mathbf{g}(\mathbf{m}) - \mathbf{d}_{obs}) \\ &+ \varepsilon(\mathbf{m} - \mathbf{m}_0)^T \mathbf{C}_m^{-1} (\mathbf{m} - \mathbf{m}_0) \\ &+ \eta \mathbf{m}^T \mathbf{D}^T \mathbf{D} \mathbf{m}], \end{aligned} \tag{4.3}$$

where $\mathbf{g}(\mathbf{m})$ represents the predicted traveltimes depending on an unknown model parameter vector $\mathbf{m}$ and $\mathbf{d}_{obs}$ is the observed traveltimes. $\mathbf{C}_d$ is the *a priori* data covariance matrix and it is best referred as a data weighting matrix in this case. Similarly, $\mathbf{C}_m$ is the *a priori* model covariance matrix best referred as a model weighting matrix. $\mathbf{m}_0$ is the initial model

parameters and **D** denotes a smoothness matrix. Damping (ε) and smoothing (η) are the regularization terms used to stabilize the inversion and to reduce the non-uniqueness. The inversion scheme is performed iteratively to account for the non-linearity of the forward problem.

We select the damping (ε) and smoothing (η) regularization terms by carefully inspecting the trade-off curves (or L curves) of root-mean-square (RMS) misfit vs. model variance and RMS vs. model roughness (Fig. 4.3). A bunch of separate inversion tests with different ε or η are carried out to construct these tradeoff curves. The inflection points on the curves represent a balance between resolution and model variance and roughness, in another word, indicating an optimum choice of ε and η (10 and 100 respectively in this study as shown in Fig. 4.3). Then, phase velocity maps a 6-30 s periods are constructed by FMST after six iterations.

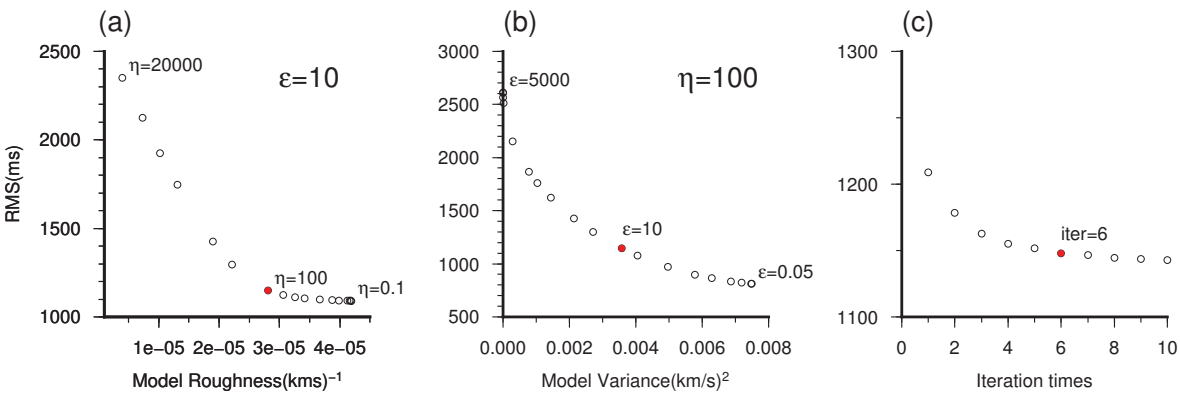

FIGURE 4.3: Trade-off curves at period of 20 s between (a) RMS and model roughness by fixing ε to 10; (b) RMS and model variance by fixing η to 100; (c) RMS and iteration number after ε and η are selected. The optimum choices of the parameters are illustrated by the red solid dots in each subfigure.

4.3.2 Two-plane surface wave tomography

We adopt the two-plane surface wave tomography (TPWT) technique [Forsyth and Li, 2005, Yang and Forsyth, 2006a,b] to invert earthquake surface wave data for phase velocity maps at periods from 25 s to 150 s. In TPWT, each incoming teleseismic surface wave is modelled as two interfering plane waves (a primary and a secondary wave) with unknown amplitude, initial phase and propagation direction [Forsyth and Li, 2005]. Using these six parameters to represent the nonplanar incoming surface waves shows a great advantage over conventional two-station approach in a situation where scattering and multipathing caused by lateral

heterogeneities between source and receivers are observed [Yang and Forsyth, 2006a]. Finite-frequency effects are considered in TPWT for each plane wave, represented by 2D sensitivity kernels with the Born approximation [Yang and Forsyth, 2006b].

A total number of ~150 events that occurred between Jul 2016 and Sep 2017 with magnitudes larger than 5.5 Mb, epicentral distances from 30° to 150° and focal depths shallower 100 km are collected. To avoid the interference of Love and/or shear waves, only vertical component seismograms are used. A series of narrow-band 4th order, zero-phase shift Butterworth filters with a width of 0.01 Hz centred at each individual period between 25 s and 150 s are applied to the vertical component seismograms and then the filtered data are windowed to isolate fundamental mode Rayleigh waves. Records with SNR smaller than 10 are discarded from the dataset. Like ANT, SNR here is also period-dependent and the calculation is similar except that the noise window starts at one hour later than the earthquake occurred. Furthermore, we only retain data recorded by at least 10 stations in this study for a reliable tomographic result. An example of selected seismic events used at period of 30 s is illustrated in Fig. 4.2b, the nearly uniform distribution of the back azimuth of selected events (Fig. 4.2c) ensured a good path coverage in our study region.

During the inversion, the best fitting parameters used to describe each incoming surface wave are inverted first by a simulated annealing method. Then, a standard linear inversion approach [Tarantola and Valette, 1982] is utilized to invert for phase velocities as well as the correction for the wave parameters. This two-step scheme is iterated twice for the final 2D phase velocity maps. A Gaussian weighting function (i.e. smoothing or averaging function) with a characteristic length (L_w) is employed to smooth the 2D phase velocity maps and the 2D sensitivity kernels for the purpose of resolution control. Generally, decreasing L_w leads to an increase in the resolution and bringing in more detailed velocity variances. However, it may also introduce some unrealistic and artificial short-wavelength features in phase velocity maps. Therefore, the smoothing length should be carefully chosen by balancing the tradeoff between resolution and model variance in any particular tomographic studies. In our case, we set the L_w regularization term as 40 km after a series of tests with different L_w and compare the results with ANT at the overlapped periods (25 s - 30 s). The averaged phase velocities for each individual period are then inverted first and the resulting 1D velocities are used for updating sensitivity kernels and act as the starting model for the inversion of the phase velocities on a 0.25° × 0.25° grid. After this process, records with misfit larger than 8s are

removed and the inversion is repeated to generate the final 2D phase velocity maps.

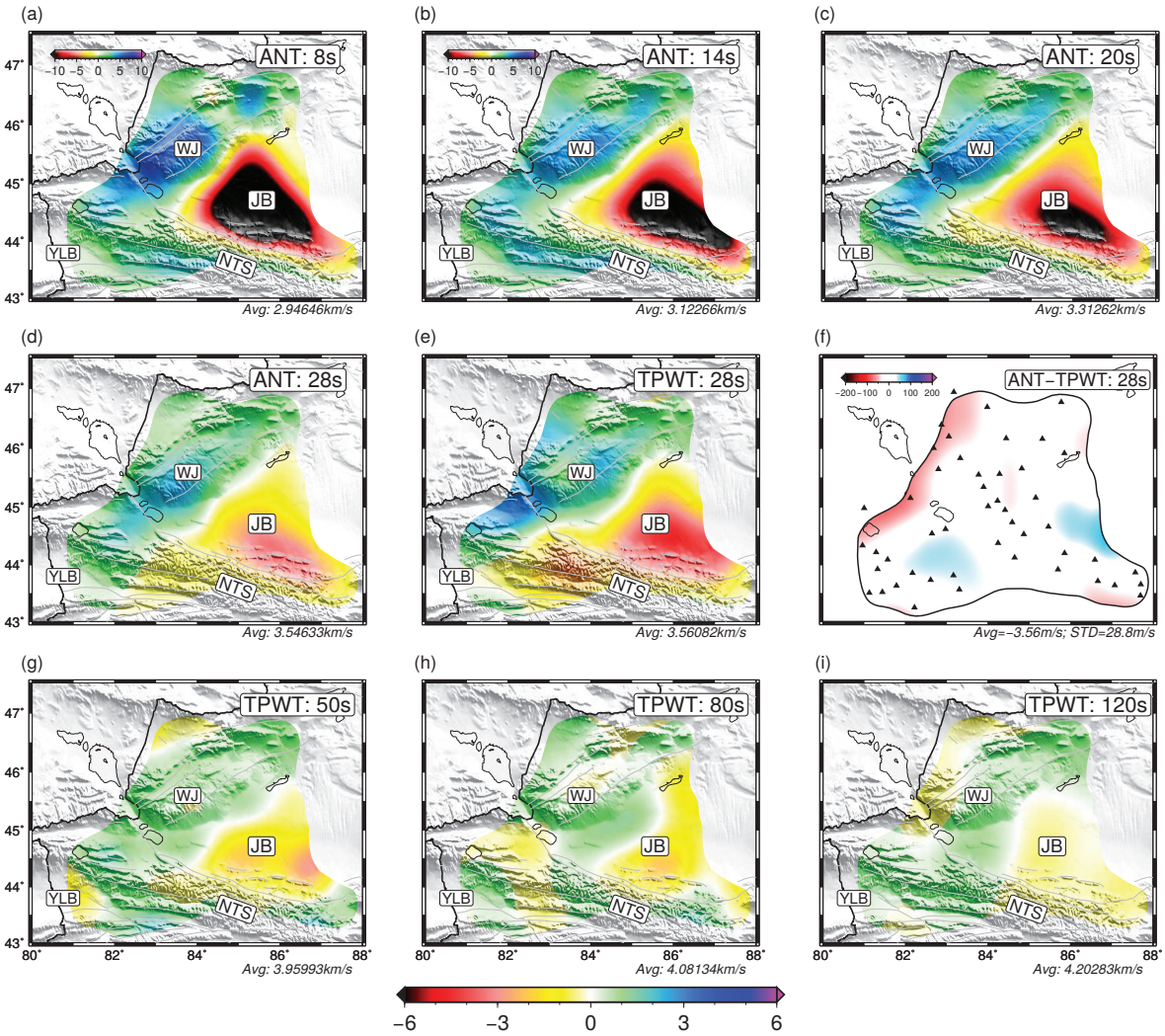

FIGURE 4.4: Examples of 2D phase velocity maps from ANT (a-d) and TPWT (e, g-i). The anomalies are relative to the average phase velocities shown at the bottom of each figure. Note that color bar for period 8 s and 14 s is different from others and plotted in the top-left corner in the subfigure. (f) Phase velocity difference between ANT and TPWT at period of 28 s with mean and STD is written in the bottom.

4.4 Phase velocity maps

The phase velocity maps from ANT and TPWT are then combined to produce phase velocity maps from 6 s to 120 s period with an overlapping band of 25 s - 30 s. Although these two techniques both focus on getting phase velocities, different sources and procedures are employed. With the assumption of diffusive and homogeneous distributed noise wavefields, ANT excludes the earthquake data and treat these data as disturbances, while TPWT utilizes surface waves from the earthquakes. For the overlapped periods, ideally the phase velocity

maps from ANT and TPWT should be identical. Since completely different data and methods are used in these two methods, differences in the phase velocity maps always exist. Examples of the phase velocity maps and the comparison at 28 s period are plotted in Fig. 4.4d-f. For most of our study region covered by seismic stations, the phase velocity map at 28 s from ANT and TPWT agree with each other within their uncertainties. The mean and standard deviation between them is ~3.56 m/s and 28.8 m/s respectively. Major differences mainly appear at the margins of the study region and/or the areas with sparse station coverage where resolution is relatively low for both two tomography methods. From the checkerboard tests shown in Fig. 4.5, it is clear that the anomalies in the unmatched areas are significantly smeared and this can further explain the differences between ANT and TPWT at such areas.

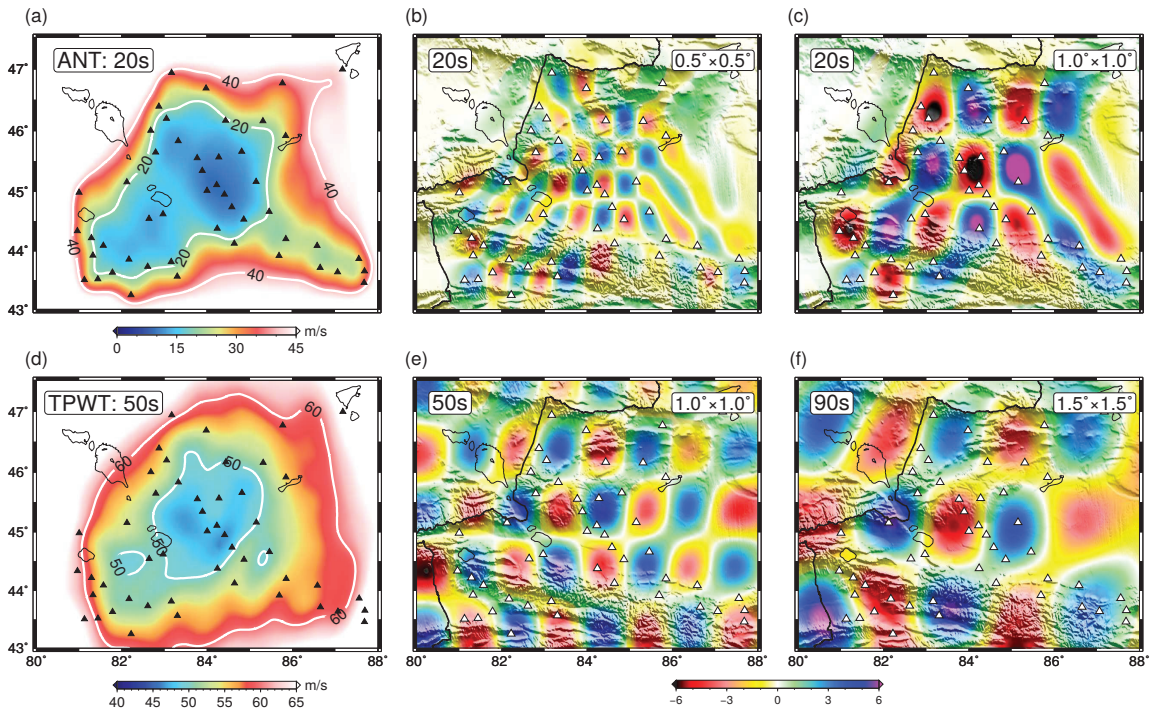

FIGURE 4.5: Uncertainty maps (a, d) and checkerboard tests (b, c, e and f) at period of 20 s, 50 s and 90 s. Different input anomaly sizes in checkerboard tests are written at the top right corner.

At periods less than 20 s, phase velocities are mainly sensitive to the upper and middle crust structures. A significant low velocity zone is observed in the Junggar basin. With the velocity reduction more than 10% at the shorter periods, this feature can be explained by the presence of a thick sedimentary layer of the basin, especially in the southern part. Meanwhile, high velocity anomalies are observed in mountainous areas and the velocities beneath the western Junggar region (WJ) are faster than the Chinese northern Tien Shan (NTS; or known as the Borohoro mountains) at shorter periods. At the longer periods, part of the NTS shows

a low velocity feature and the velocity variations become smaller with increasing period.

The uncertainties of the phase velocities obtained from FMST can be calculated by taking the diagonal elements of the *a posteriori* model covariance matrix $\mathbf{C}_M$:

$$\mathbf{C}_M = \varepsilon(\mathbf{G}^T\mathbf{C}_d^{-1}\mathbf{G} + \varepsilon\mathbf{C}_m^{-1})^{-1}, \tag{4.4}$$

where $\mathbf{G}$ is the Fréchet derivative sensitive kernel, ε is the damping factor to tune the inversion, $\mathbf{C}_d$ and $\mathbf{C}_m$ are the *a priori* data and model covariance matrix respectively [Rawlinson et al., 2003]. Because $\mathbf{C}_d$ and $\mathbf{C}_m$ used in the inversion only act as weighting parameters and do not truly reflect the prior errors of data and model, the absolute values of the uncertainties are actually imprecise, but their relative values are still useful to indicate the accuracy of the solution between different nodes. Uncertainties from TPWT are calculated in a similar way as follows:

$$\sigma_v^2 = \mathbf{q}(\mathbf{G}^T\mathbf{C}_d^{-1}\mathbf{G} + \mathbf{C}_m^{-1})^{-1}\mathbf{q}^T, \tag{4.5}$$

where $\mathbf{q}$ stands for the vector of weights for all the grid points for a particular position and σ_v is the standard deviation [Forsyth and Li, 2005], the uncertainties are represented by two times of this standard deviation. A common drawback of the uncertainty estimation for both ANT and TPWT is that they are derived from linear theory and cannot fully represent the non-linearity of the inversion problems here. Checkerboard tests are also conducted to examine the resolution power of the tomographic scheme, we model the input velocity field with perturbations of ±6% in a dimension from 0.5° × 0.5° to 2° × 2° for both FMST and TPWT. Synthetic input data are calculated based on the same ray path with Gaussian noises added and then inversions are carried out with the same parameters used in real data, including damping, smoothing and inversion grid size of 0.25° × 0.25°. Fig. 4.5 shows the uncertainty maps and checkerboard resolution tests at periods of 20 s, 50 s and 90 s. Uncertainties at 20 s period from ANT are less than 20 m/s for the most part of the study region, while for TPWT, the uncertainties are larger and increase with period, reaching ~50 m/s at 50 s period. In the checkerboard tests, it is clear that the resolution power of ANT at shorter periods are much better than that at longer periods of TPWT. At 20 s period, ANT successfully recovers the anomaly with a dimension of 0.5° × 0.5° at the center of the study region where we have the best ray path coverage. However, at longer periods where TPWT is employed, the size of recoverable anomaly is limited to 1° × 1° for 50 s and 1.5° × 1.5° for 90 s due to the fast decrease of the number of teleseismic events used (196 events at 50 s

and 110 at 90 s). After a variety of checkerboard tests with different anomaly sizes, we only retain the phase velocities at periods shorter than 120 s by taking resolution and our interest structure size into consideration.

4.5 Shear wave velocity inversion

Local phase velocities at each grid node and their uncertainties are extracted by combining the phase velocity tomographic maps at different periods. All the local phase velocity dispersion curves are visually inspected and phase velocity data with large oscillations over period, especially at shorter periods (< 8 s), are discarded. Then, a probabilistic (Bayesian) inference nonlinear inversion approach [Afonso et al., 2013a, Guo et al., 2016b] is employed to invert the local dispersion curves for 1D shear wave velocities. In the past, the Bayesian inference approach is successfully applied in many geophysical studies [e.g. Duijndam, 1988a,b, Mosegaard and Tarantola, 1995, Tarantola and Valette, 1982]. The solution of the Bayesian inference inversion is represented by a posterior probability density function (PDF), also known as the *a posteriori* PDF. This posterior PDF can be simply represented as:

$$\sigma(m) = k\rho(m)L(m), \tag{4.6}$$

where $\rho(m)$ is the prior (or *a priori*) PDF containing our prior knowledge on the model parameters. In our case, it represents the possible distribution range of shear wave velocities and reasonable thickness of the crust and/or sedimentary layer according to previous studies or global model; $L(m)$ is the so-called $likelihood\ function$ which relates model parameters to the observed data. It measures how well a particular set of model parameters can generate the observed data; and k is a normalization constant. Thus, the posterior PDF can be concluded as how our prior information on the model space are updated by the observed data.

To sample the posterior PDFs, which is usually with a large parameter space and no closed form, a Markov chain Monte Carlo (MCMC) algorithm based on Delayed Rejection and Adaptive Metropolis (DRAM) [Haario et al., 2006] is used. This chain can be separated into two parts. The first part is called the burn-in period, during which model parameters are randomly generated to produce the proposed model and a selection based on acceptance criterion ratio is employed to determine whether to accept or reject this model. After nth models are proposed, we enter the second part of the chain. Now the proposal distribution starts to be updated according to all the previous proposals at a fixed interval. Finally, the

first part of the chain is discarded and the last samples on the second part are treated as the 'important samples' which usually provide a relatively good estimation of the posterior distribution for the model parameters. The number of initial samples during the burn-in period and the updating intervals during the second part of the chain are strongly experiential and protean for different problems [Guo et al., 2016b, Haario et al., 2006, Shen et al., 2013]. If the algorithm is allowed to run long enough, we can get a very stable estimation, but at the same time, a higher computational effort is required. So, as a balance, we set 60,000 samples for the burn-in period and 10,000 for the following update interval in this study after numerous tests has shown these numbers are large enough. The last 3,000 models in the chain are saved to construct the accepted posterior PDF or the so-called 'ensemble solution'. The average value and standard deviation (STD) is calculated on the last 3,000 accepted models to represent the final 1D shear wave velocity profile and its uncertainty.

The prior shear wave velocity model parameterization is similar to Guo et al. [2016b] and Shen et al. [2013]. When constructing the prior models, B-splines are usually used to describe the shear velocities in the crustal and mantle layer. Generally, using more B-splines to describe shear velocities leads to a smaller misfit between the inverted and observed data, but it may also bring in overfitting effects with possible artificial and unrealistic features. Therefore, based on a series of tests with different numbers of B-splines ranging from 3 to 8, four B-splines are finally chosen in this study to represent the crustal layer and five B-spline for the mantle layer as it can produce a relatively smoothed solution with reasonable misfits. The total thickness of the model is parameterized to 300 km and the prior shear wave velocities searching range are set to ±20% from the PREM global model. The Moho depth is taken from receiver function study [Li et al., 2014] with a variation of ±5 km added to account for the large Moho perturbation observed in the study region, and velocities are forced to increase across the Moho interface. For the nodes located in the Junggar basin, a sedimentary layer is also considered and modelled with three parameters including the thickness and the velocities at the top and bottom of the sedimentary layer. The thickness of sedimentary layer is taken from Crust 1.0 [Laske et al., 2013] with ±3 km variation and the searching range of shear velocity is set between 1.5 km/s to 3.0 km/s. In summary, there are a total 10 or 13 (dependent on if a sedimentary layer is present or not) unknown free parameters in the inversion.

Because phase velocities are most sensitivity to *Vs*, the solution for *P*-wave velocity (*Vp*)

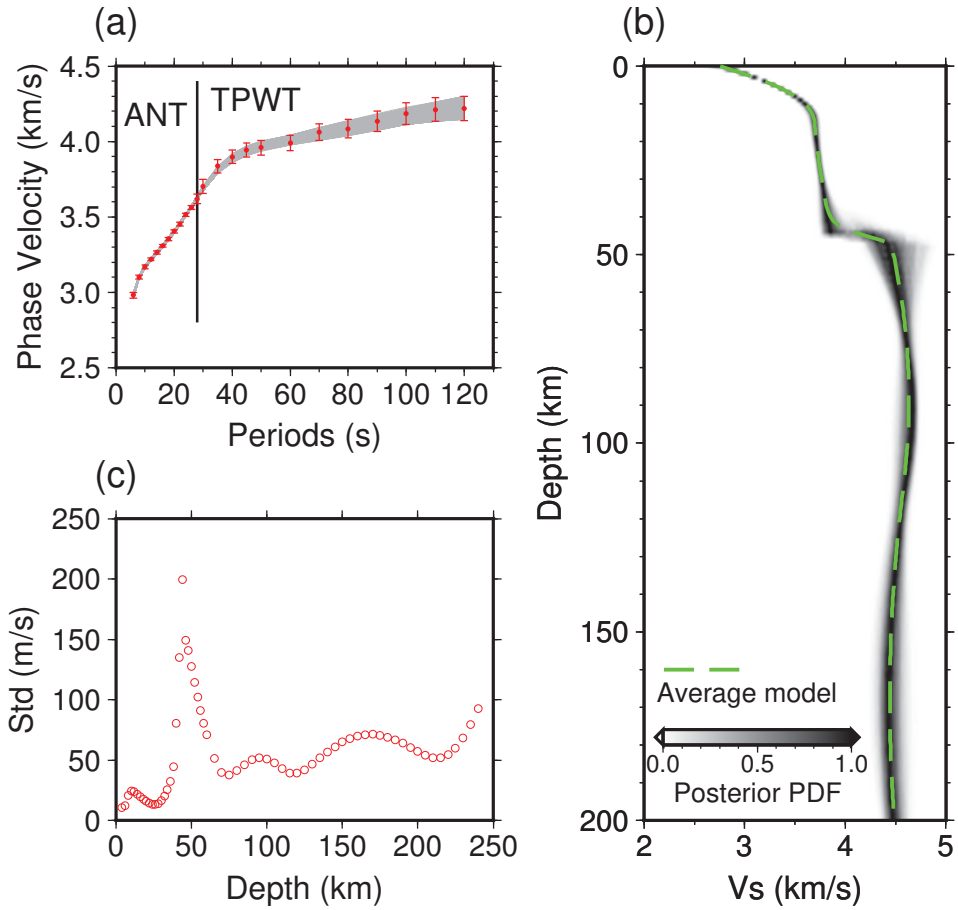

FIGURE 4.6: 1D MCMC based probabilistic inversion at 84°E, 45.5°N. The red dots with error bars and gray lines in (a) represent the observed and predicated phase velocity dispersion curves respectively. (b) Shear wave velocity profile inverted from the phase velocities in (a), the background colors denote the normalized posterior PDF, darker color means a higher probability distribution of the shear wave velocity. The averaged model is indicated by green dash line. (c) Standard deviations of all the models used to construct the posterior PDF.

and density (ρ) in the inversion are calculated based on an empirical function [Brocher, 2005]:

$$V_p = 0.9409 + 2.0947V_s - 0.8206V_s^2 + 0.2683V_s^3 - 0.0251V_s^4, \tag{4.7}$$

$$\rho = 1.6612V_p - 0.4721V_p^2 + 0.0671V_p^3 - 0.0043V_p^4 + 0.000106V_p^5. \tag{4.8}$$

While, in the sedimentary layer, the V_p/V_s ratio is set to a value of 2.0 and the density is guided by the Gardner's rule [Gardner et al., 1974]:

$$\rho = 1.74V_p^{0.25}. \tag{4.9}$$

Also, **Q** value from PREM model is introduced to correct the physical dispersion of shear wave velocity model. An example of the 1D shear wave inversion is illustrated in Fig. 4.6 (for grid nodes located in the JB, an exampled 1D *Vs* inversion is given in supplementary materials Fig. 4.10), predicated phase velocities fit the observed data well with very small

misfits. As surface waves are insensitive to horizontal interface, the Moho cannot be accurate constrained in the inversion. Thus, in Fig. 4.6c, the largest uncertainties are observed around the expected depth of Moho (~50 km). The shear wave velocity uncertainties also slightly increase with depth, possibly caused by the larger errors from longer periods surface wave phase velocities.

4.6 Results

A 3D shear wave velocity model is constructed by combining all the 1D *Vs* profiles at each grid node. Fig. 4.7 shows *Vs* maps at several depths ranging from 10 km to 200 km. The velocity perturbations are mapped relative to the regional averaged *Vs* at the corresponding depth.

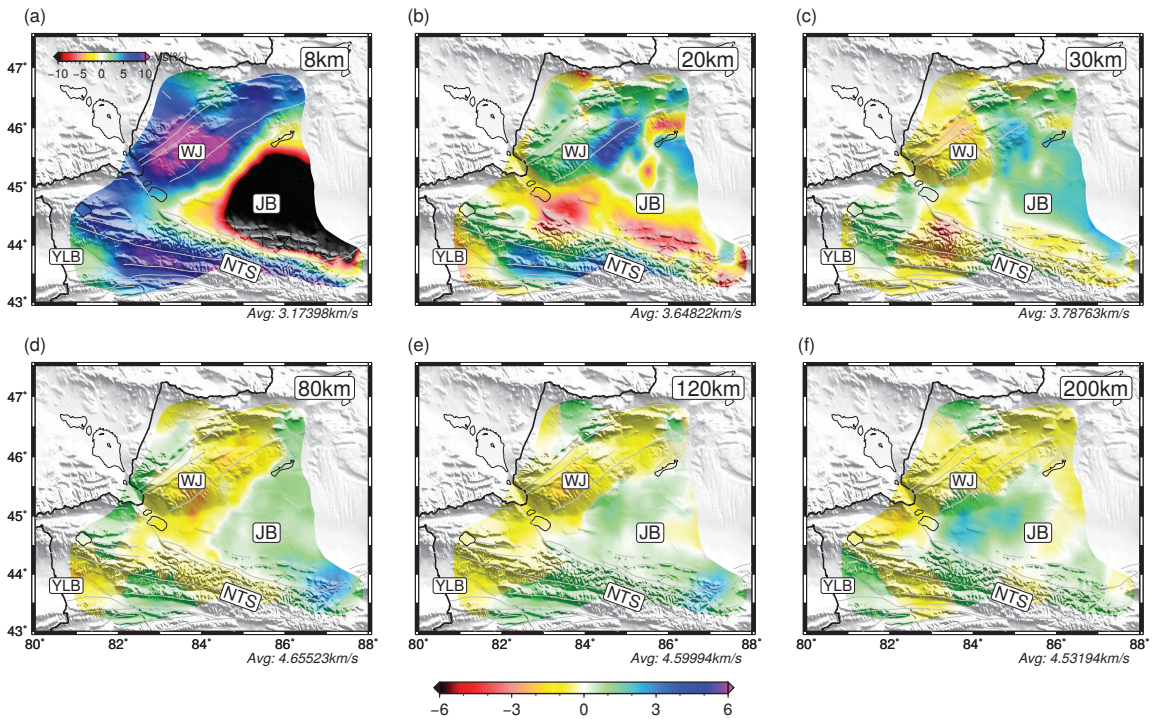

FIGURE 4.7: *Vs* perturbation maps at six different depths ranging from 8 km to 200 km. Color pattern for the depth of 8 km is different from others and plotted in the top of (a). The average *Vs* is labeled at the bottom right of each subfigure.

In the upper crust, such as 8 km depth (Fig. 4.7a), the patterns of velocity anomalies agreed well with the geological units. A large triangular shaped low velocity zone dominates the entire Junggar basin region (JB), and low velocities are also observed in the shallow crust beneath the Yili block (YLB). These low velocities are believed to be associated with the

sedimentary layers, especially the JB where thick sedimentary layer exists. According to previous seismic reflection/refraction survey [Zhao et al., 2003], the sedimentary layer of JB reaches ~8-9 km in the north and over 10 km in the southern margins. The thick sediments in the JB are highly related to the rapid uplift of the NTS in the south after the collision between Indian and Eurasian plate [Xu et al., 2017]. In contrast, high velocity anomalies appear in the WJ in the northwest and the NTS in the south. From the middle to lower crust (20-40 km), inverse velocity features compared to those at the shallow crust characterize the study region. The entire JB is characterized by high velocities. This mid/lower crust velocity anomaly is consistent with our previous local crustal tomographic results based on a smaller seismic array in WJ [Wu et al., 2018]. The most significant velocity feature in the uppermost mantle is the wide spread high velocities beneath the JB. This high velocity body stretches into the NTS at depths over ~80 km. In contrast, low velocities are found along the WJ and continues towards the southwest into YLB. At depths over 120 km, high velocity anomalies beneath the JB start to extend northwestward towards WJ with increasing depth and the JB is characterized by two different parts with high velocities in the west and low velocities in the east.

Several vertical profiles are plotted in Fig. 4.8 and supplementary materials Fig. 4.12 to better illustrate the vertical variations of *Vs*. The AA' profile starts at the northern foothill of NTS and runs northwestward through the entire JB and all the way to WJ. This ~400 km cross-section shows several interesting features. In the upper crust, the JB is imaged as a prominent low *Vs* zone, with shear velocities much lower than 3.0 km/s. The thickest part of this low velocity body is found beneath the southern margin of the JB. At the depths of middle to lower crust, *Vs* beneath JB increases significantly, reaching ~3.9 km/s to ~4.0 km/s in the lowermost crust. The mid/lower crust high velocities extend into the NTS in the south, and dip toward northwest with depth underneath the WJ. The uppermost mantle is dominated by a high velocity body beneath JB and NTS. The thickness of this high velocity layer is ~60 km and with *Vs* higher than 4.65 km/s. In the margin between JB and WJ, this high velocity body slightly dips northwest, reaching a depth around 150 km. High velocities are also observed to the west of WJ with a thickness of only ~30 km, thinner than the high velocity layer beneath the WJ and NTS. The uppermost mantle of WJ is dominated by a relatively low velocity anomaly extending down to the depth of ~240 km.

The north-south trending BB' profile traverses the central JB and the east part of WJ.

The velocity features are similar to the AA' profile. The uppermost mantle of JB and the north NTS is characterized by high velocities, while the upper mantle of WJ is imaged as low velocities. The thickness of the uppermost mantle high velocities drops from 150 km in WJ to 120 km in NTS and the highest velocity is found in the southern JB.

4.7 Discussion

4.7.1 The nature of the high velocity upper mantle beneath JB

The nature of the JB basement is a contested topic over the past decades. Characterized by high seismic velocity anomalies, the basement is interpreted either as the Precambrian micro-continent [Watson et al., 1987, Zhang et al., 1984] or the fragments of the Paleozoic oceanic crust [Chen and Jahn, 2004, Feng et al., 1989]. In our previous research, by examining the shape and the absolute velocity values, we interpret the mid- and lower crustal high velocities beneath JB as the remnant oceanic crust of the late Paleozoic times [Wu et al., 2018], this interpretation is also supported by multidisciplinary study in the Junggar region [Xiao et al., 2008, Zheng et al., 2007]. Despite it is extremely tough for a fragment of fossil oceanic crust to be well-preserved to the present, the western Junggar region seems to be a perfect exception where the ancient subduction characteristics are still intact.

In both AA' and BB' profile (Fig. 4.8), nearly flat high velocities are observed both in the lower crust and uppermost mantle of JB. Xiao et al. [2008] suggest that the entire JB is a trapped small ocean during the Carboniferous to Permian and the WJ is an ancient intraoceanic arc. Also, magnetotelluric and Bouguer anomaly both support this assumption [Xu et al., 2016]. Therefore, we interpret these high velocities beneath JB as the remnant of the ancient oceanic lithosphere beneath the ancient Junggar Ocean. In the AA' profile beneath WJ, the upper mantle high velocity body slightly dips northwestward and then terminates at a depth of around 150 km. According to the geometry of the high velocity body, it is reasonable to deduce the polarity of the late Paleozoic subduction in WJ is northwestward. Although it is widely accepted that multiple subductions took place in WJ at different episodes throughout Paleozoic [Xiao et al., 2015a], it should be noted that our current *Vs* model can only retrieve the last subduction event in this region.

In addition, the present-day temperature in the study region is inverted from a multi-observable, probabilistic method [Afonso et al., 2013a,b, 2016, Guo et al., 2016a]. By jointly

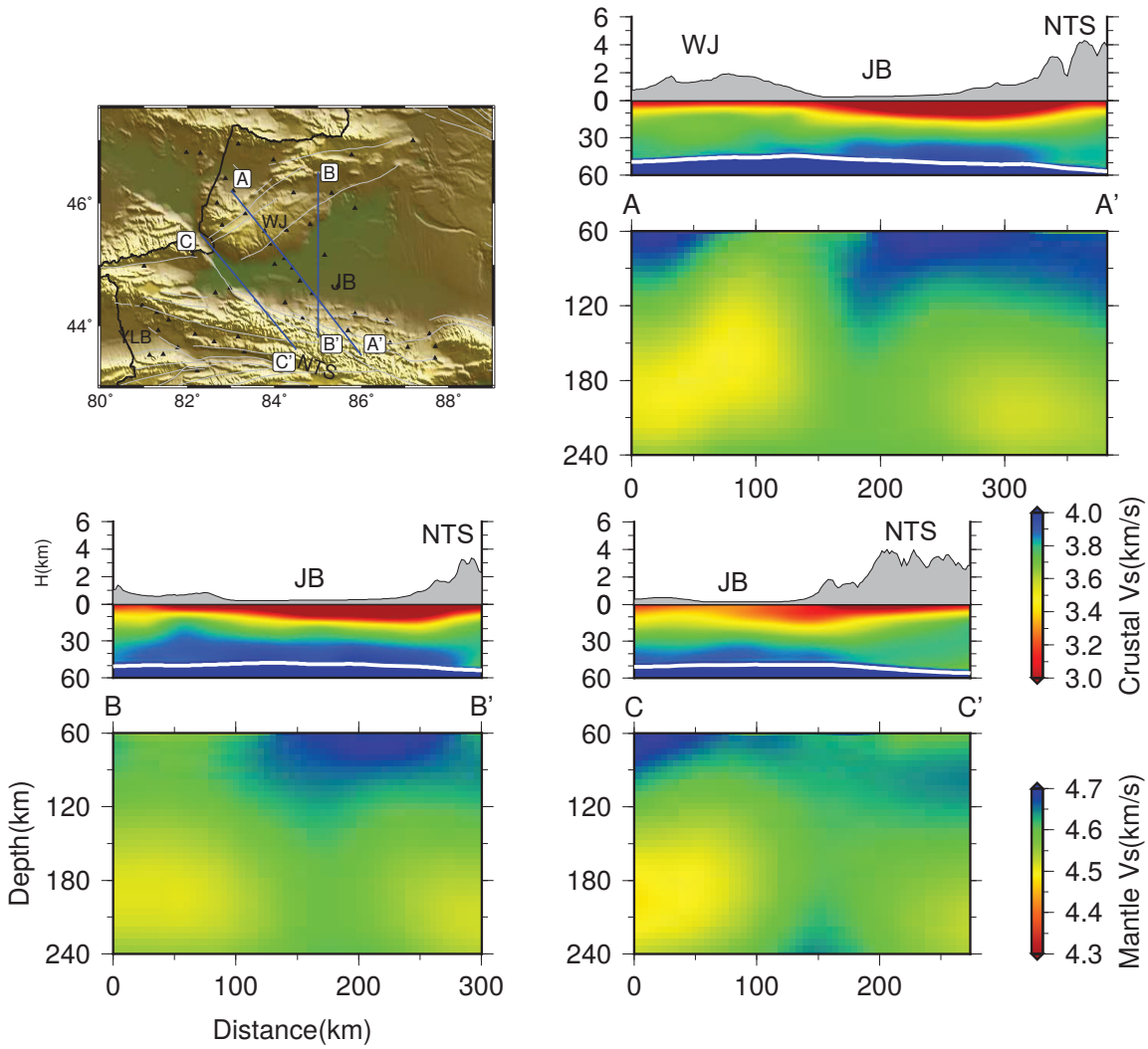

FIGURE 4.8: Three vertical cross-sections with their locations marked in the topographic map. Note that two different color patterns are used to plot the crustal and mantle structures.

inverting our Rayleigh wave dispersion data, surface heat flow, Geoid, and topography, this method can provide a self-consistent thermal and compositional model of the lithosphere and sub-lithospheric mantle. In the Bayesian framework, a MCMC scheme based on the DRAM algorithm [Haario et al., 2006] is used to sample the posterior distribution [Tork Qashqai et al., 2016]. For the geotherm, the temperature in the lithosphere are obtained by solving 1D steady-state heat transfer equation, while the geotherm for sub-lithospheric mantle mainly depends on seismic data. All final acceptable thermal models are constrained by all observables, albeit different relative weight [Afonso et al., 2013a]. This inversion technique has been successfully applied to North China Craton [Guo et al., 2016a], south Africa [Jones et al., 2017], south China craton [Shan et al., 2014] and etc. The detail about the inversion is beyond the scope of this study and will be presented in a separate paper [Zhang et al. in preparation].

The calculated geothermal map at the depth of 120 km is given in Fig. 4.9b (geothermal maps at other depths are shown in supplementary materials Fig. 4.13), it is obvious that the JB is characterized two domains with high temperatures (~950 °C) in the east and low temperatures (~840 °C) in the west. The entire WJ is featured by high temperatures around 960 °C.

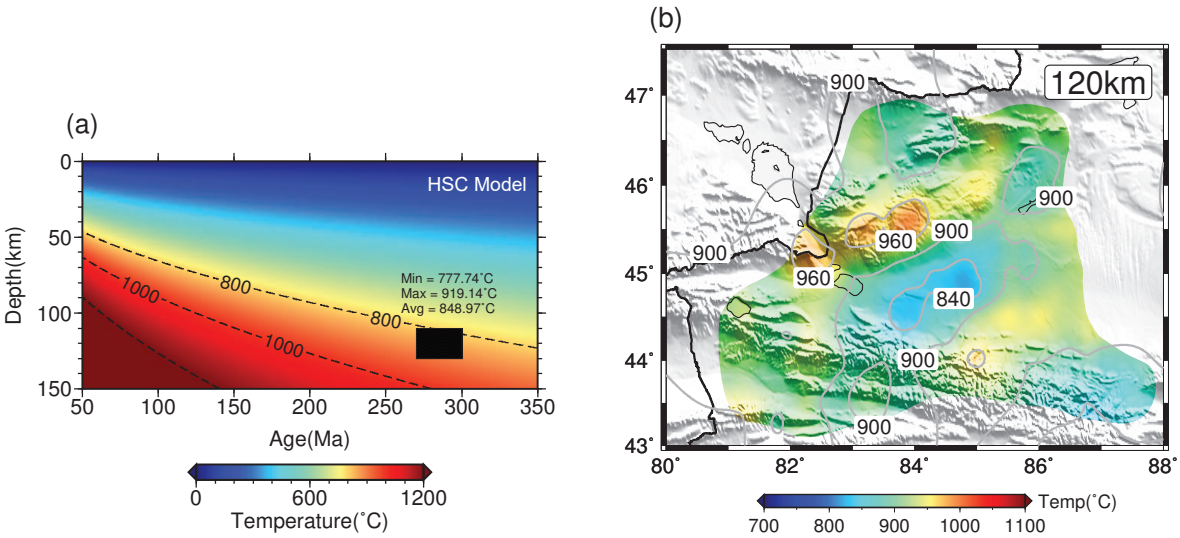

FIGURE 4.9: (a) Calculated age-dependent temperatures of an oceanic lithosphere based on the half-space cooling (HSC) model. Black dotted box indicates the theoretical temperature range for a piece of mid-late Permian oceanic slab at depth around 120 km. Maximum, minimum and average temperature within the box are written beside the box. (b) Present-day geothermal map at depth of 120 km from multiple observational MCMC inversion.

Assuming no further reheating or tecto-thermal events occurred in the WJ after the subduction ceased, we can assume the upper mantle of JB cools following the half space cooling model (HSC). With this assumption, we can estimate the present geotherm of the JB upper mantle and compare the predicted temperatures with the inverted temperatures from the multi-observable, probabilistic method described in the preceding paragraph. The calculation of HSC temperature can be simply formulated as:

$$T(z,\tau) = (T_m - T_0) erf\left(\frac{z}{2\sqrt{\kappa\tau}}\right) + T_0, \tag{4.10}$$

where $T(z,\tau)$ is the temperature at depth z with age τ, T_0 and T_m are the temperature at surface and the initial mantle temperature, and κ is the thermal diffusivity factor. In this study, we set T_0, T_m and κ to 0 °C, 1350 °C and $1 \times 10^{-6}\ m^2\ s^{-1}$, respectively. The calculated HSC temperature as a function of age and depth is shown in Fig. 4.9a.

Determining the final subduction age is vital as a change in the age leads to different calculated HSC temperature. Most previous studies (e.g. paleontology, paleomagnetism,

geochronology and geochemistry) suggest that the complex multiple subduction settings probably terminated during Permian (no later than end Permian) after the Tarim block collided with NTS [Xiao et al., 2008, Yang et al., 2012a]. Thus, we estimate the age of the JB lithosphere to be around 270 Ma to 300 Ma old by assuming the prior subduction age of the oceanic lithosphere is around several tens of million years. Then, we extract the HSC temperature between depths 110 km to 130 km at ages of 270 Ma to 300 Ma (gray box in Fig. 4.9a). The geotherm in the gray box range from ~780 °C to ~920 °C with an average geotherm of 849 °C. This averaged temperature exactly match the low geotherm anomaly in the western part of JB at the depth of 120 km (Fig. 4.9a). Since the HSC model is mainly used for estimating the cooling of an oceanic lithosphere, the good match further supports our previous interpretation of the bent remnant oceanic slab beneath the margin between JB and WJ.

In general, when an oceanic lithosphere gets colder, it becomes denser and subducts into the deep mantle. One crucial question we need to address is why the trapped oceanic lithosphere can still survive beneath JB for hundreds of million years without deformation and delamination. As discussed above, the JB originated from a trapped ocean (Junggar ocean) during the late Paleozoic times [Carroll et al., 1990, Xiao et al., 2008] and the subduction of Junggar oceanic slab beneath WJ failed and terminated after the final closure of Paleo-Asia ocean. Based on our present-day *Vs* model, the high *Vs* anomaly disappears beneath WJ at depths over ~150 km, possibly indicating the missing of the already subducted slab under WJ. Thus, no matter what mechanism causes the disappearance of the subducted slab, the unsubducted flat oceanic lithosphere under JB lost the pulling force and the strain rate within the remnant slab decrease. These effects result in a relatively stable system slowing down sinking or deformation of the remnant unsubducted oceanic lithosphere. Then, the lack of subsequent thermal events in this region further provide an undisturbed environment allowing the slab to stay alive till the present.

4.7.2 Upper mantle low velocities beneath WJ

One of the appealing feature in our velocity model is the upper mantle low *Vs* anomaly beneath WJ (Fig. 4.8a) with low velocities reaching ~4.5 km/s, slightly dipping northwestward. The late Paleozoic magmatic associations in WJ (e.g. A-type and I-type granitoids, adakites, tholeiites, charnockites, Nb-enriched and magnesian dikes) are thought to be related to the

upwelling of asthenosphere materials though the slab window after the ocean ridge subducted into WJ in the late Carboniferous era [Yin et al., 2013]. In recent years, a ocean ridge related subduction and an opened slab window in WJ during late Paleozoic times are drastically disputed [Geng et al., 2009, Ma et al., 2012, Tang et al., 2012a, Windley and Xiao, 2018, Yin et al., 2013, 2010].

In this study, only based on our 3D velocity structures, it is difficult to find some clues of the possible ancient ridge subduction. When a spreading ridge subducts beneath the overriding plate, hot upwelling sub-oceanic mantle partially melt at the either side of the ridge and then cause slab window widening with depth and time [Kinoshita, 2002, Thorkelson, 1996]. This process make it extremely hard for us to image the structure and the location of the subducted ridge over a long period of time. Although low velocities are observed beneath WJ in AA' profile, we cannot simply ascribe these low velocities to the upwelling asthenosphere through a slab window. The upwelling asthenosphere can also be generated after the subducted slab break-off, which is also a possible explanation in this case since the slab break-off model is widely accepted for subducted slabs [von Blanckenburg and Davies, 1995] and believed to be the final fate of the slab due to the force of the gravitational pull [Wortel and Spakman, 2000]. Thus, the past subducted Junggar oceanic slab beneath the WJ may have already detached and sunk deeper after subduction ceased. Thus, the absence of continuous high *Vs* structures in the current tomographic image at the deeper mantle (> 150 km) of WJ could either be ascribed to the widening of the slab window after the ridge subduction, or the slab detachment and subsidence, or even the combination of both two mechanisms (e.g. slab rollback and subsidence after ridge subduction).

4.8 Conclusions

Using a regional broadband seismic array consisting of 49 stations deployed in Junggar region, northwestern China from Jul 2016 to Aug 2017, we perform surface wave tomography combining ANT and TPWT techniques to generate high-resolution 3D shear wave velocity model of the crust and upper mantle in the Junggar region. The model indicates that the entire JB is underlain by high velocity upper mantle. We interpret the high velocity upper mantle as the remnant Junggar oceanic lithosphere, which is trapped till now since the late Paleozoic times after the ancient subduction of Junggar ocean ceased. The good match in temperature

between the theoretical calculation from HSC model and the inverted present-day geotherm further supports the interpretation of a trapped fossil slab underneath JB. According to the geometry of the high velocity body in the western margin of JB, we conclude that the last subduction scenario of Junggar Ocean in the WJ is northwestward. The lack of continuous high velocity anomaly beneath WJ in the deeper mantle indicates that the fossil subducted slab have already broken off after the subduction ceased and/or molten after mid-ocean ridge is involved in the subduction.

4.9 Supplementary materials

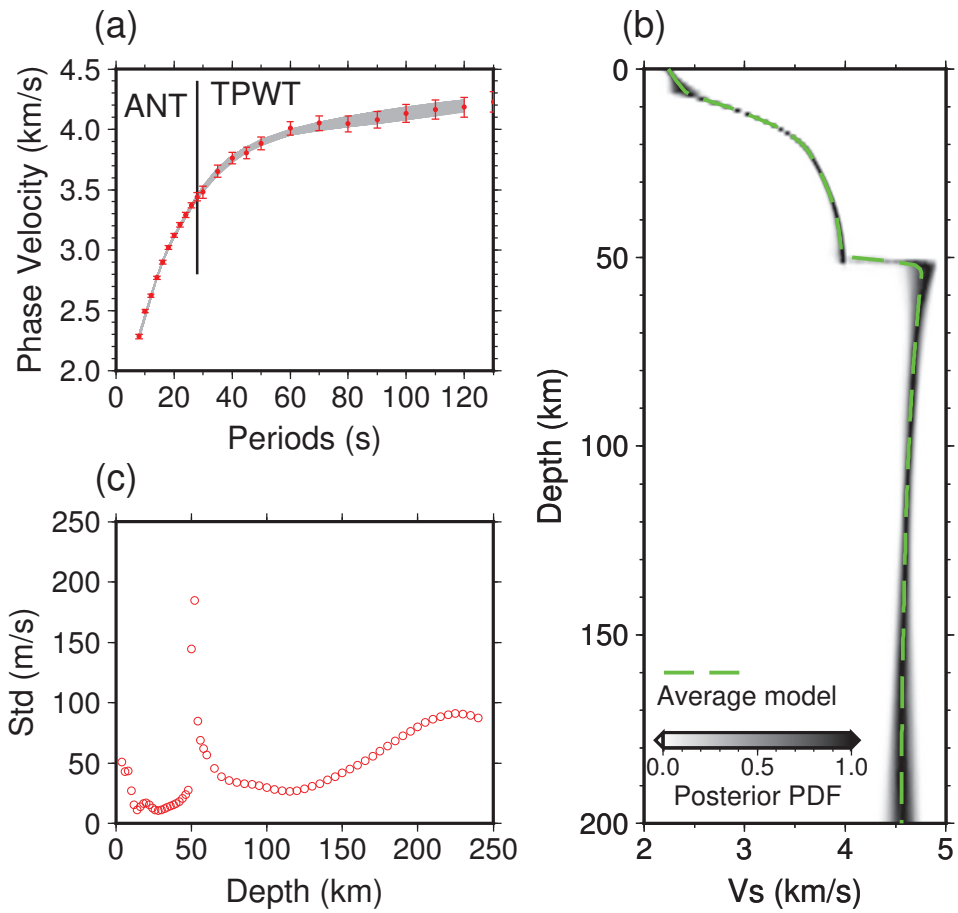

FIGURE 4.10: 1D *Vs* MCMC probabilistic inversion at 85°E, 44.5°N. The red dots with error bars and gray lines in (a) represent the observed and predicated phase velocity dispersions respectively. (b) *Vs* profile inverted from the phase velocities in (a), the background colors denote the normalized posterior PDF, darker color means a higher probability distribution of the shear wave velocity. The averaged model is indicated by green dash line. (c) Standard deviations of the posterior PDF as a function of depth.

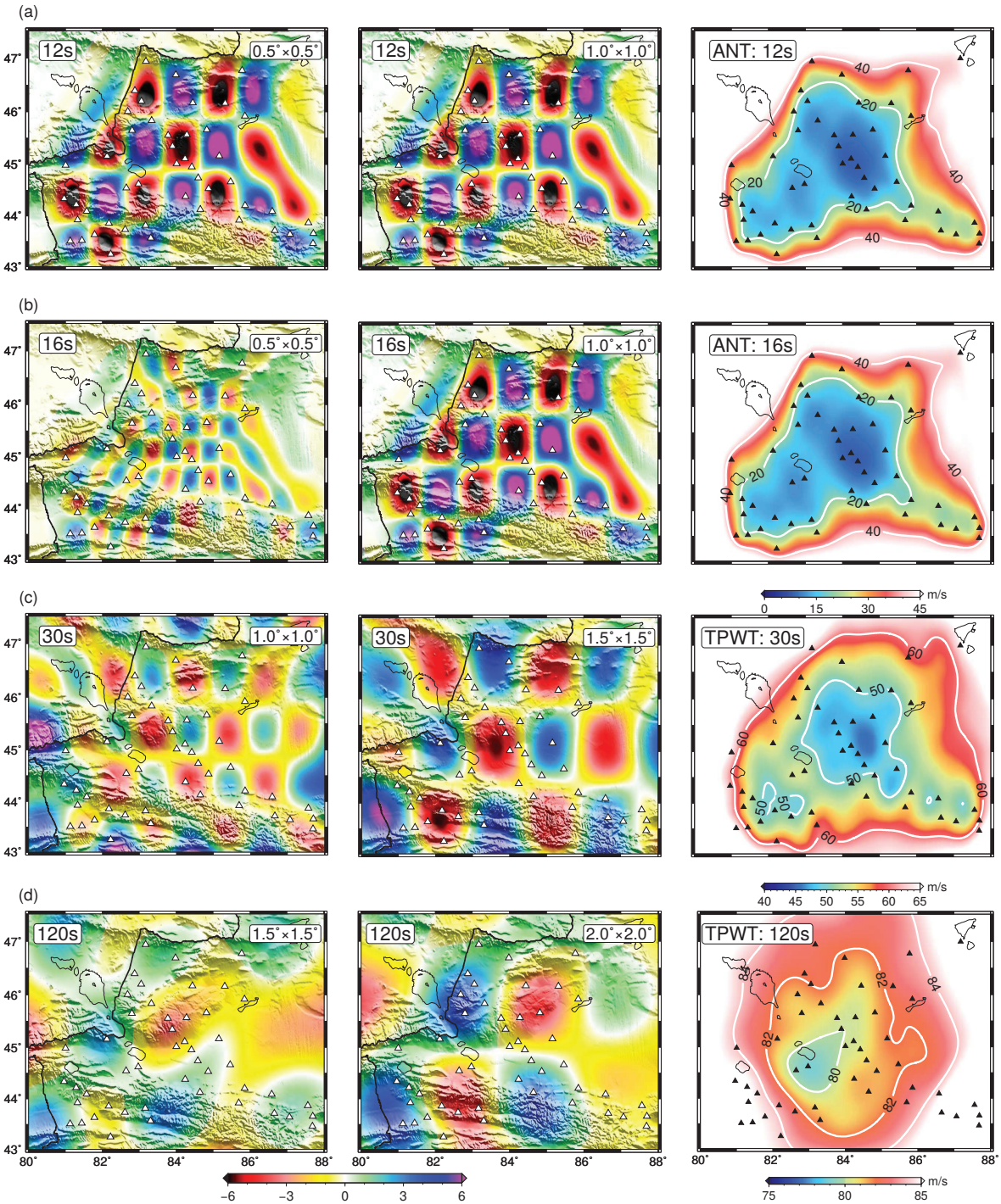

FIGURE 4.11: Examples of uncertainty maps and checkerboard tests at period of 12 s, 16 s, 30 s and 120 s.

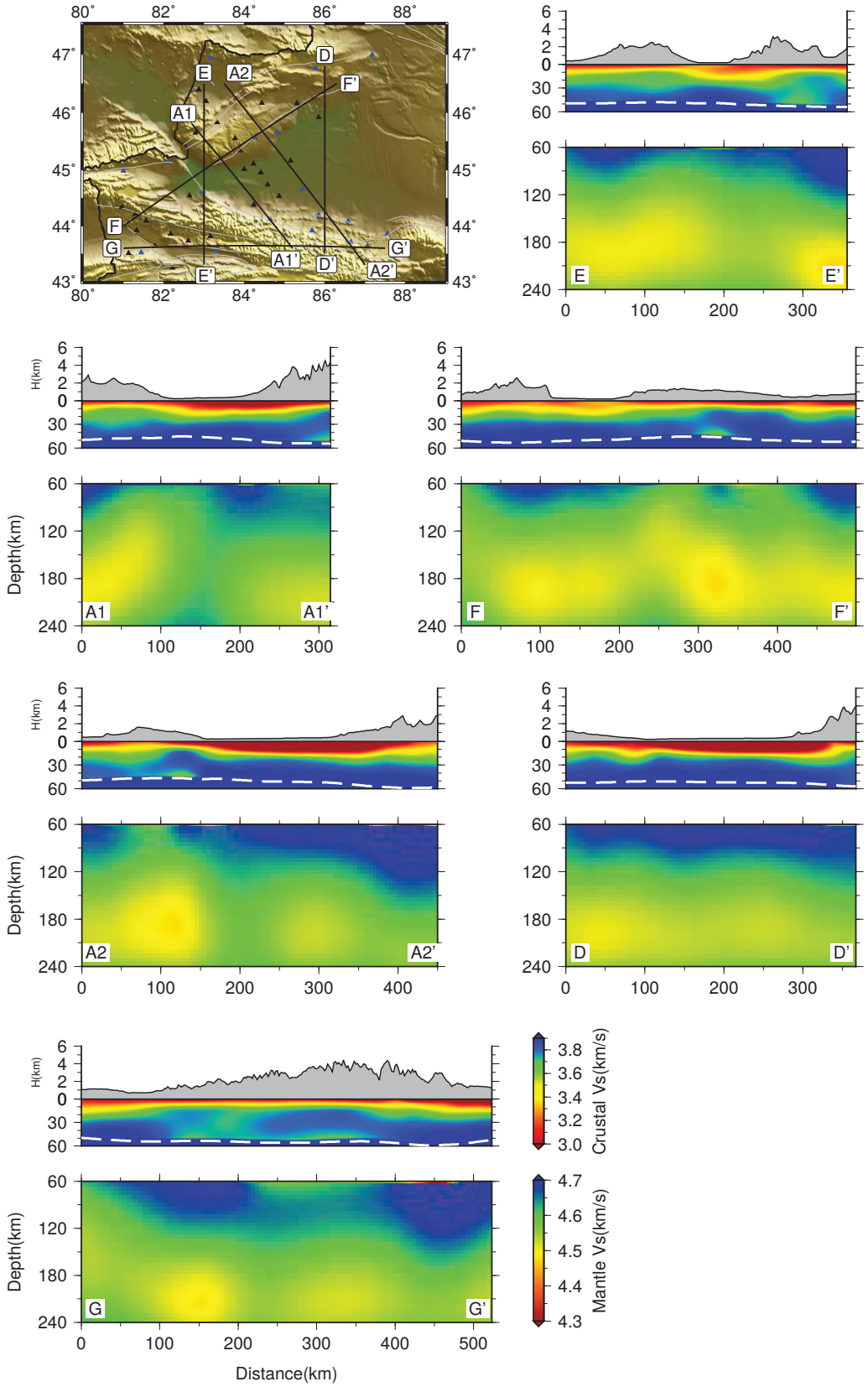

FIGURE 4.12: Supplementary *Vs* vertical slices.

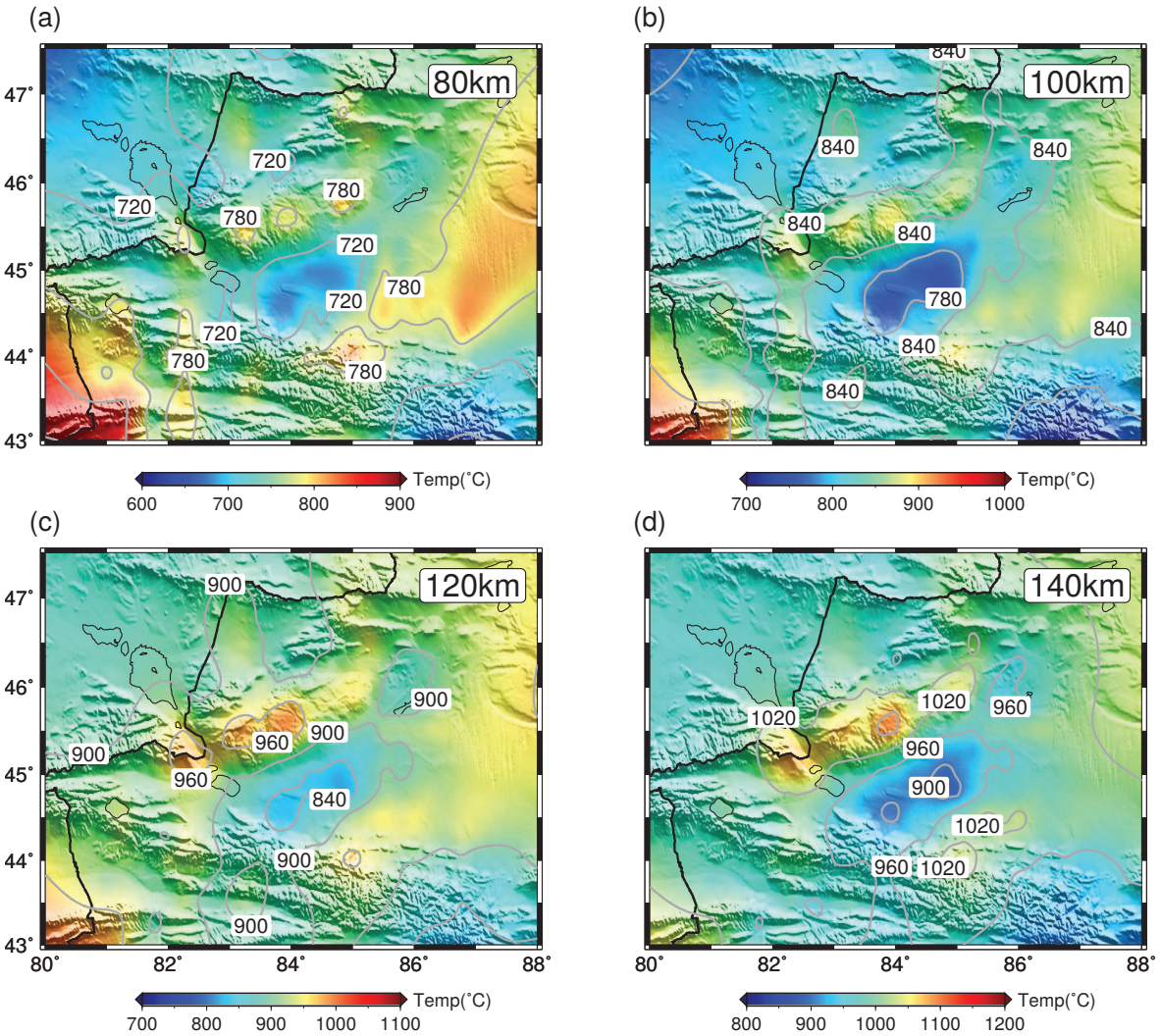

FIGURE 4.13: Temperature slices at depth of 80 km, 100 km, 120 km and 140 km.

Network	Station name	Longitude (°E)	Latitude (°N)	Elevation (m)
CEA	ALS	82.1190	45.1530	1215.00
CEA	CBC	81.4392	43.5211	1591.00
CEA	FUH	87.1790	46.9930	665.00
CEA	HEF	85.7680	46.7700	1224.00
CEA	HTB	86.5844	44.0869	928.00
CEA	JHE	82.9700	44.6200	387.00
CEA	KMY	84.8149	45.6565	610.80
CEA	LHG	87.0606	43.6378	1621.00
CEA	LSG	84.2750	45.5639	1250.00
CEA	RGN	87.5614	43.8653	755.00
CEA	SCH	85.6869	43.9172	1262.00
CEA	SHZ	85.8500	44.2000	644.00
CEA	STZ	86.6531	43.7133	2260.00
CEA	TAC	83.1670	46.9380	951.00
CEA	WMQ	87.6950	43.6544	970.00
CEA	WNQ	81.0000	44.9800	1391.00
CEA	WSC	87.6853	43.4569	1500.00
CEA	WSU	84.6408	44.1231	1830.00
CEA	XNY	83.3030	43.5640	1045.00
CEA	XYD	85.4570	44.6590	317.00
CEA	YUM	82.6810	46.0020	1312.30
XJ17	S01	83.9758	46.6876	662.70
XJ17	S02	85.3109	46.1567	433.60
XJ17	S03	85.8457	45.9163	336.10
XJ17	S04	82.8724	46.3945	435.00
XJ17	S05	84.4361	46.1657	798.60
XJ17	S06	85.1508	45.1582	282.50
XJ17	S07	82.7935	45.6432	1770.00
XJ17	S08	83.7691	45.5514	1681.10
XJ17	S09	84.2420	44.3780	489.30
XJ17	S10	84.0002	45.0113	251.40
XJ17	S11	84.4081	44.9489	282.20
XJ17	S12	80.9595	44.3355	1113.60
XJ17	S13	81.2897	44.2160	1281.90
XJ17	S14	81.3259	43.9218	656.70
XJ17	S15	81.1243	43.5081	1613.20
XJ17	S16	82.1708	43.8564	1034.80
XJ17	S17	81.5673	44.0905	980.30
XJ17	S18	82.6099	43.7336	1182.00
XJ17	S19	83.1593	43.8139	1516.30
XJ17	S20	81.7807	43.6339	708.40
XJ17	S21	82.2194	43.2463	1005.50
XJ17	S22	82.6398	44.5421	332.30
XJ17	WJS04	83.0496	46.1965	739.00
XJ17	WJS10	83.3228	45.8315	1442.50
XJ17	WJS24	83.8877	45.3397	1044.30
XJ17	WJS31	84.2285	45.1043	260.00
XJ17	WJS41	84.5804	44.7352	313.40
XJ17	WJS44	84.8631	44.5311	382.10

Table 4.1: Information for seismic stations used in the chapter 4 and 5.

5

Upper Mantle Velocity Model of the Junggar Terrain from Body Wave Finite-frequency Tomography

5.1 Summary

The Junggar terrain of northwestern China, with its unique evolutionary history, allows the preservation of late Paleozoic subsurface features. Relicts of the late Paleozoic subducted oceanic slabs are identified previously at crustal and uppermost mantle depths by variety of tomographic techniques. Here we present a new upper mantle shear wave velocity model based on body wave finite-frequency tomography. Teleseismic *S* wave traveltime residuals of three different frequency bands are collect on the data from 49 seismic stations deployed in the Junggar terrain from 2016 to 2017. The newly generated Vs model revels similar high velocity anomaly features in the crust and uppermost mantle which support the preservation of

fossil subducted slabs in the western Junggar. At depths from 150 km to 350 km, distinct low velocity anomalies with magnitude of ~-2% are found beneath western Junggar. Underlying this low velocity body, high velocity anomalies with magnitude of 1% to 2% are imaged in and above the mantle transition zone beneath western Junggar. This mantle transition zone high velocity body beneath western Junggar is discussed as either the detached slab or part of the mantle convection system in the Junggar region, while the above low velocities are interpreted as the upwelling asthenospheric mantle which possibly triggered by the opening of the slab window or the subsidence of the detached oceanic slab beneath western Junggar.

5.2 Introduction

Accretionary orogens are usually found at convergent plate boundaries side by side with subductions [Cawood and Buchan, 2007, Cawood et al., 2009, Isozaki et al., 2010, Xiao et al., 2008]. These accretionary processes are the most significant mechanism contributing to the global continental growth. However, the detailed geodynamics are still poorly understood due to the absence of continuous geological records [Condie, 2000, Rudnick, 1995]. In general, an accretionary orogen is a complex association of microcontinents, accretionary complexes and magmatic arcs [Choulet et al., 2016]. They can vary largely in special scales (from hundreds of kilometers to several thousand kilometers) and geological times (up to 3.2 Ga or even earlier) [Cawood et al., 2009, Xiao et al., 2010]. Understanding the detailed mechanisms and dynamics related to these orogeny is a crucial scientific conundrum as it can help to gain better knowledge of continental growth and also reconstruct global tectonics.

Among all the accretionary orogens, the Central Asian Orogenic Belt (CAOB, or the Altaid tectonic collage) is one of the largest orogenic belt that occupies a large area in the central and northern Asia (~9 million km^2) [Şengör et al., 2013]. It largely contributed the continental growth in central Asian from the Paleozoic with a complex closure of Paleo-Asian ocean [Eizenhöfer et al., 2014, Xiao et al., 2009] to the early Mesozoic. The present-day CAOB is surrounded by the eastern European craton to the east, the Siberian craton to the north, the Tarim and north China craton in the south [Jahn, 2000, Kröner et al., 2008, 2007, Şengör et al., 1993]. The accretionary growth mechanism, evolutionary history of the CAOB, and the closure time of Paleo-Asian ocean are still hotly debated. Several contradictory evolutionary models have been proposed in the past few decades to explain the tectonic mystery of CAOB

[e.g. Coleman, 1989, Şengör and Natal'In, 1996, Şengör et al., 1993, Windley et al., 2002, Yakubchuk, 2002, 2004]. Geologically, the CAOB can be divided into the eastern and western parts [Şengör and Natal'In, 1996, Şengör et al., 1993]. The eastern part was assembled by the convergence of the Siberian craton, the North China craton and the Mongolia block during the early Mesozoic; whereas the western part was formed by the convergence of the eastern European craton, the Siberian craton and the Tarim craton from the late Proterozoic to the late Paleozoic - early Mesozoic [Xiao et al., 2010].

The Junggar terrain, situated in the south of the western CAOB, is regarded as an ideal place to investigate the complex accretion and subduction processes during the Paleozoic because of the exposure of geological units, e.g. ophiolites, intrusions, accretion wedges, etc., and the well-preserved late Paleozoic subsurface structures [Ma et al., 2012, Wu et al., 2018, Xiao et al., 2008, 2015a, Xu et al., 2016, Zhang et al., 2011b]. Currently, there is no consensus on the evolutionary models in this region and various hypotheses are proposed. For instance, the subduction patterns in western Junggar (WJ) at the late Paleozoic are highly disputed.Contradictory models are discussed such as a double-sided subduction system [Yin et al., 2015, Zhang et al., 2011a,b], a single developed subduction with polarity either northwestward or southeastward [Jiang et al., 2010, Ma et al., 2012, Tang et al., 2010, Wang et al., 2003], a ridge-related subduction [Geng et al., 2009, Jiang et al., 2010, Tang et al., 2012b], and a failed northwestward subduction [Wu et al., 2018, Xu et al., 2016].

A high-resolution seismic model of the lithosphere and asthenosphere in this area helps discriminate among the different models. Benefit from the recently deployed broadband seismic array across the Junggar terrain, we can generate high-resolution seismic tomography images of the subsurface structures in this region. Previous works based on surface wave tomography have revealed the detailed shear wave velocities of the crust and upper mantle down to the depth of ~250 km in the Junggar terrain. In this model, high shear wave velocities are imaged in the uppermost mantle and lower crust of Junggar basin (JB), possibly associated with the trapped oceanic lithosphere [Wu et al., 2018, Xu et al., 2016]. Based on this velocity model, a failed northward subduction is suggested for the Paleozoic evolution in the Junggar region. However, due to the limitation of vertical resolution of fundamental Rayleigh waves, the structures at deeper depths (> 250 km) is not well imaged. Having a velocity model of the deeper structure is crucial since it helps further rebuild the tectonic processes in the Junggar terrain and trace the plausible past subducted slabs. In this chapter, we construct a shear

wave velocity model down to the depth of ~500 km in Junggar terrain based on body wave finite-frequency tomography technique.

5.3 Data

The data used in this study are collected from a regional seismic array deployed in the Junggar terrain from July 2016 to August 2017. This seismic array consists of 49 broad band seismic stations (21 temporary and 28 permanent stations from China National Seismic Network), covering the entire WJ and some parts of JB in the east and Chinese Northern Tien Shan (NTS) in the south (Fig. 5.1). Information for the seismic stations are listed in table 4.1. Continuous seismic data recorded by this seismic array are utilized previously for surface wave tomography (chapter 4). In this chapter, we use teleseismic *s* wave traveltime residuals in the body wave finite-frequency tomography.

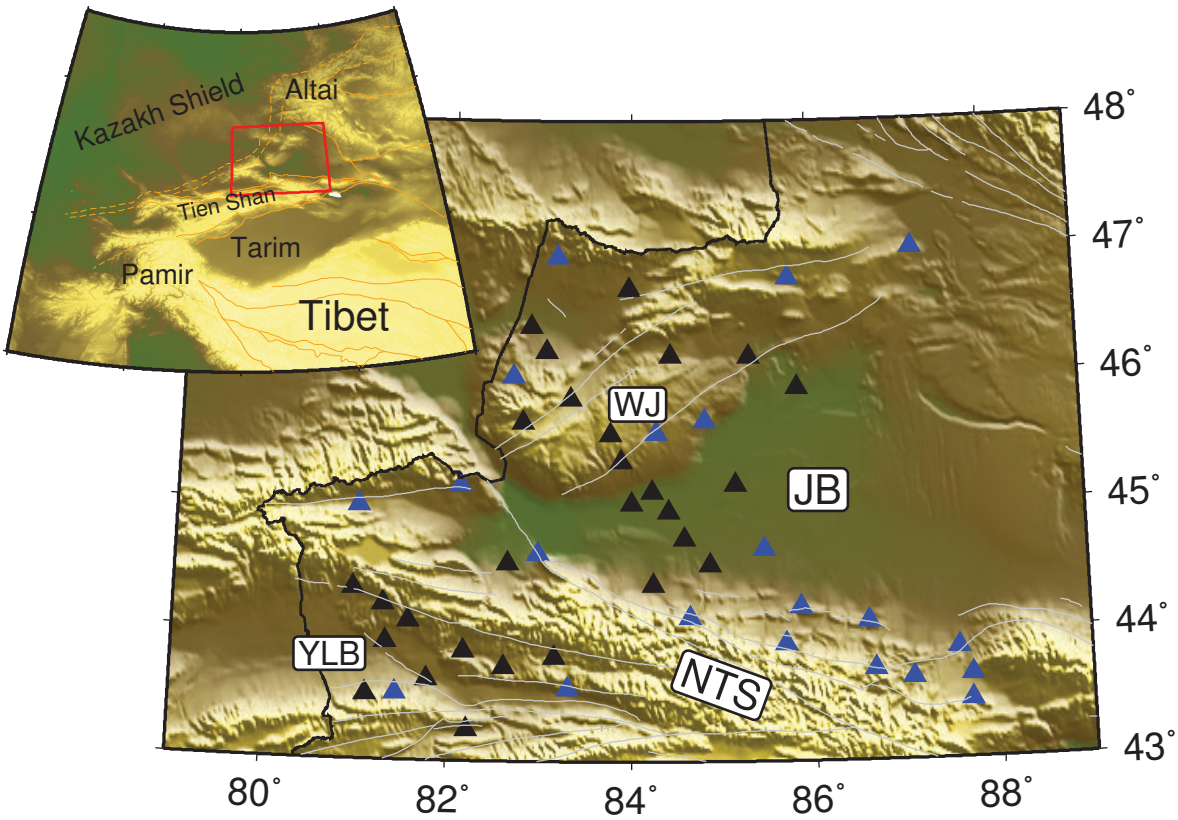

FIGURE 5.1: Topography map of the study region and the distribution of seismic stations used in this study. Blue triangles represent the 21 fixed stations from CEA and black triangles indicate the 28 deployed stations. Orange lines indicate the major boundaries for tectonic blocks, gray lines denote the major faults in the study region, black solid line is the Chinese national border. Abbreviations in the topography map are WJ (western Junggar or the Zaire mountain), YLB (Yili Block), JB (Junggar Basin or the Dzungarian Basin), NTS (Chinese northern Tien Shan or the Borohoro Mountains).

Numerous studies demonstrate that body wave traveltimes are also frequency-dependent due to the diffractive wave-front healing effects [Guo et al., 2018, Hung et al., 2004], i.e. traveltimes with different frequencies are sensitive to heterogeneities with different spatial ranges [Hung et al., 2011]. The lower frequency components are generally sensitive to a larger area away from the geometrical ray path and non-sensitive to the structure along and close to the path. Thus, we filter the raw transverse component recordings into three different frequency bands of 0.02-0.05 Hz, 0.05-0.1 Hz and 0.1-0.5 Hz, which correspond to the low, medium and high frequencies. Then, the teleseismic *S* wave relative traveltimes are measured from the data within these three different frequency bands separately. In this study, the relative traveltimes are picked by using an Automated and Interactive Measurement of Body-wave Arrival Times (AIMBAT) software package [Lou et al., 2013]. In the AIMBAT software, relative traveltimes are calculated by applying the multi-channel cross-correlation (MCCC) technique [Vandecar and Crosson, 1990]. As a semi-automated scheme, the MCCC shows a great advantage in efficiency, reducing labor efforts and visual errors compared with picking arrival times manually. The MCCC scheme measures the traveltime delay at each station relative to the mean traveltime in the study region, eliminating the hypocenter mis-location and timing errors but also removing the absolute velocity information within the study region. Therefore, unlike surface wave tomography which directly invert for the absolute shear wave velocities, our body wave traveltime tomography do not achieve the absolute velocity values. The relative traveltime at each station for each event is then transformed into traveltime residual by subtracting the regional averaged theoretical arrival times calculated from 1D reference model.

Strict criteria are employed when selecting traveltime residuals. Only signals with correlation coefficients greater than 0.9 and SNR larger than 3 are retained. Also, we remove the residuals with absolute value larger than 3 s to avoid the cycle-skipping effect. The strict criteria result in that more than 50 percent of the traveltime residuals are discarded. Finally, 103 events are selected for *S* wave traveltime measurement with their epicentral distances ranging between 30° to 90° and magnitudes larger than 5.5 Mb (Fig. 5.2). To have an overview on the pattern of traveltime residuals in the study region, the averaged *S* wave traveltime residuals for each station at three independent frequency bands are illustrated in Fig. 5.3. Similar features are observed for the traveltime residuals at these three frequency bands. The fastest arrival times can be found along the northern NTS, while delayed arrival times are observed

beneath WJ. The average traveltime residuals in the northern WJ are smaller with values close to zero. These measured traveltime residuals are then utilized in the finite-frequency body wave tomography as presented in the following sections.

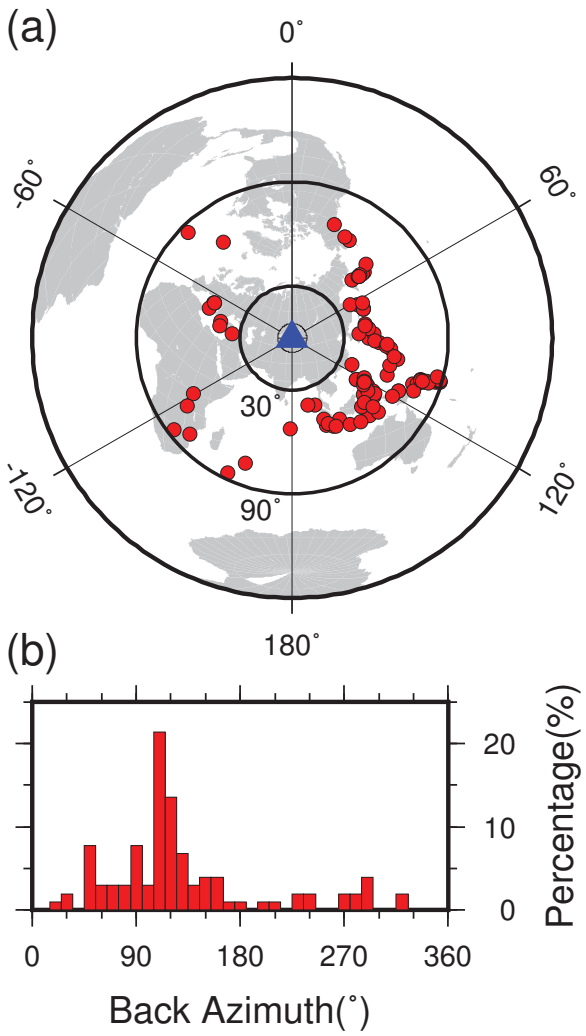

FIGURE 5.2: (a) Location of the seismic events used in the body wave traveltime tomography and (b) their back azimuth distribution.

5.4 Method

Conventionally, body wave traveltime tomography assumes that waves generated by teleseismic events travel along geometrical lines connecting each source and receiver. The differences between actual arrival times and theoretical arrival times calculated from reference Earth models (PREM, IASP91, AK135, etc.) are mainly caused by the heterogeneities along the geometrical paths. The traveltime shift $\delta(t)$ under the ray theory assumption can

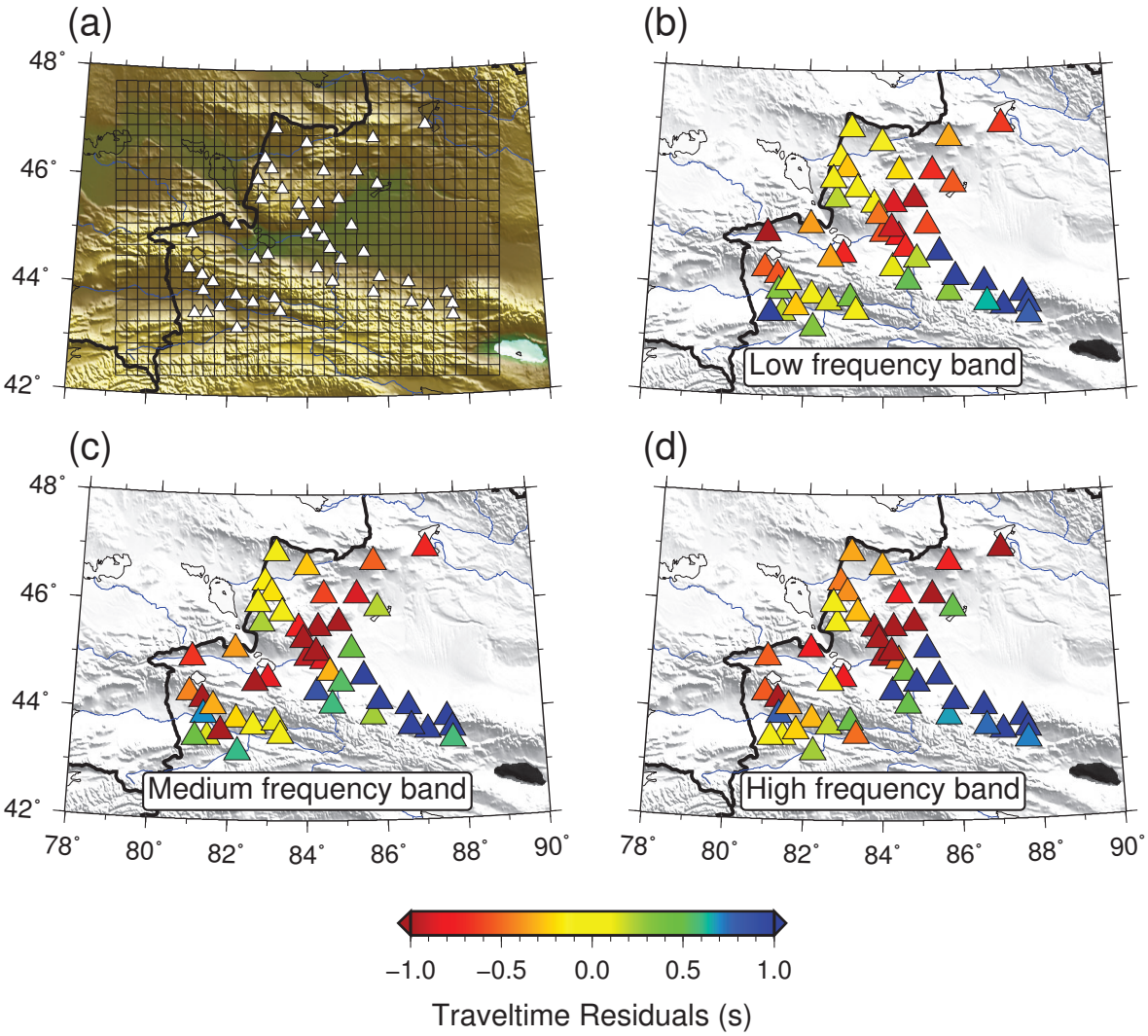

FIGURE 5.3: (a) Horizontal view of the parameterized mesh in the body wave traveltime tomography. (b), (c) and (d) Averaged traveltime residual at each station for three individual frequency bands.

be expressed as:

$$\delta(t) = -\int_{ray} c(\mathbf{x})^{-2}\delta c(\mathbf{x})dl, \tag{5.1}$$

where dl is the incremental length along the theoretical ray path in the unperturbed Earth structure, $c(\mathbf{x})$ refers to the wave velocity from a reference 1D Earth model, and $\delta c/c$ is the relative velocity anomalies to be imaged. In practice, an actual finite-frequency body wave is sensitive to 3D structures encircling a ray path, leading to the fact that actual traveltimes can vary as a consequence of wave front healing, scattering, and other diffraction effects off the ray paths. For example, a longer periods (> 20 s) teleseismic body wave is sensitive to a wider range of structures with a few hundred kilometers away from the ray path in the upper mantle [Hung et al., 2004]. Hence, a 3D finite-frequency sensitivity kernel with a wide sensitivity range must be considered in order to account for the off-ray

sensitivity characteristics of body waves and also eliminate the wave front healing effects. In general, the finite-frequency sensitivity kernel for teleseismic body wave traveltimes is shaped symmetrical around the geometrical ray path like a banana-doughnut, and the region between the two-sided symmetrical lobes with the strongest sensitivity are called the 'Fresnel zone'. The widths of the Fresnel zone are highly related to the frequency of the wave and the epicentral distance, which motivate us to introduce body wave traveltimes with different frequency bands into the tomography.

By considering the finite-frequency effect, the function 5.1 is then transformed into a 3D form:

$$\delta(t) = \iiint_{\oplus} K(\mathbf{x})\delta c(\mathbf{x})/c(\mathbf{x})d^3\mathbf{x}. \tag{5.2}$$

Here, the $K(\mathbf{x})$ is the 3D sensitivity kernel that relates the traveltime shift $\delta(t)$ to the perturbations in P- or S-wave relative velocities $\delta c/c$. Based on the Born single-scattering approximation together with the body wave propagation properties, the sensitivity kernel $K(\mathbf{x})$ is constructed in an efficient way following Dahlen et al. [2000]:

$$K = -\frac{1}{2\pi c}\left(\frac{\mathscr{R}}{c_r\mathscr{R}'\mathscr{R}''}\right)\frac{\int_0^\infty \omega^3|s_{syn}(\omega)|^2\sin(\omega\Delta T)d\omega}{\int_0^\infty \omega^2|s_{syn}(\omega)|^2 d\omega}. \tag{5.3}$$

In this function, we assume a scatterer exists off the geometrical ray path with the location $\mathbf{x}$, which location corresponds to the integration $\mathbf{x}$ in function 5.2. Thus, ΔT denotes the addition traveltime when the ray path takes a detour going through this scatterer. The c and c_r, which act as scaling factors here, are the 1D reference model velocity at the scatterer $\mathbf{x}$ and the receiver $\mathbf{r}$. $\mathscr{R}$, $\mathscr{R}'$ and $\mathscr{R}''$ represent the geometrical ray spreading factors for the unperturbed ray (geometrical lines linking source and receivers), the source-to-scatterer ray and the scatterer-to-receiver ray, respectively. The $\left|s_{syn}(\omega)\right|^2$ is the power spectrum of the Earth pulse at frequency ω. This power spectrum relates the body wave traveltime sensitivity kernels to frequency.

For regional tomographic problems, the general way to solve the inverse problem is to parameterize the wave velocity or slowness on a grid of nodes. The perturbation at each node is constrained by the traveltime data of the general data equation:

$$\mathbf{d}_i = \mathbf{G}_{ij}\mathbf{m}_j, \tag{5.4}$$

where $\mathbf{d}$ is the data vector matrix consisting Nth traveltime measurements, i.e. $\mathbf{d}$ =

$[\delta t_1, \delta t_2, \cdots, \delta t_N]^T$,and $\mathbf{m}$ denotes the model vector matrix containing Mth velocity parameters, i.e. $\mathbf{m} = [m_1, m_2, \cdots, m_M]^T$, where M corresponds to the total number of grid nodes. The $\mathbf{G}_{ij}$ represents sensitivity of the ith data to the jth node. More specifically, $\mathbf{G}_{ij}$ can be understood as the integrated volumetric kernel $Kd^3\mathbf{x}$. In this study, we parameterize our model space as a spherical cap which is slightly larger than our seismic array. The cap extends from 79°E to 89°E from east to west, 42°N to 48°N from south to north and from the surface down to 800 km depth. We then divide our model into ~0.25° grids horizontally (36×28 nodes) and 10 km grids (81 nodes) vertically, resulting in a total number of 81,648 grid nodes ($M = 36 \times 28 \times 81 = 81,648$). Using relative traveltime residuals in the tomography implies that the sensitivity to the structure outside the modelled box are identical for different events, preventing local contaminations caused by the unresolved anomalies outside the model space. Fig. 5.3a gives a horizontal view of the mesh in this study.

A standard damped least squares (DLS) scheme is employed when solving model parameter $\mathbf{m}$, the DLS solution with a minimum norm constrain can be expressed as:

$$\mathbf{m} = (\mathbf{G}^T\mathbf{G} + \theta^2\mathbf{I})^{-1}\mathbf{G}^T\mathbf{d}, \tag{5.5}$$

where $\mathbf{I}$ is the identity matrix with dimension of $M \times M$, θ^2 is a positive damping factor. The inverse of the matrix here is estimated by the iterative LSQR method of Paige and Saunders [1982].

For the data processing steps, we strictly follow the traveltime tomography workflow of Dahlen et al. [2000] and Hung et al. [2002, 2004]. First, a two-point ray tracing based on Bisection shooting method [Osborne, 1969] is adopted to calculate the theoretical linearized ray path between event-station pairs. AK135 continental 1D model [Kennett et al., 1995] is employed in the ray tracing as a starting reference model. Then, the tracked ray paths within the parameterized mesh are used to construct the 3D banana-doughnut shaped sensitivity kernels as described in function 5.3. Corrections relevant to the 3D crustal structures and topography are made by adding a free term at each station to account for the arrival time shifts. Corrections relevant to events baseline difference are also considered by introducing an event correction term during the inversion.

In tomographic problems, regularization terms are essential to stabilize the inversion. Because a 3D finite-frequency sensitivity kernel provides a natural smoothing regularization, to avoid the ad hoc smoothness effects, the only regularization term required here is the norm damping factor [Obrebski et al., 2011]. To select the appropriate damping parameter,

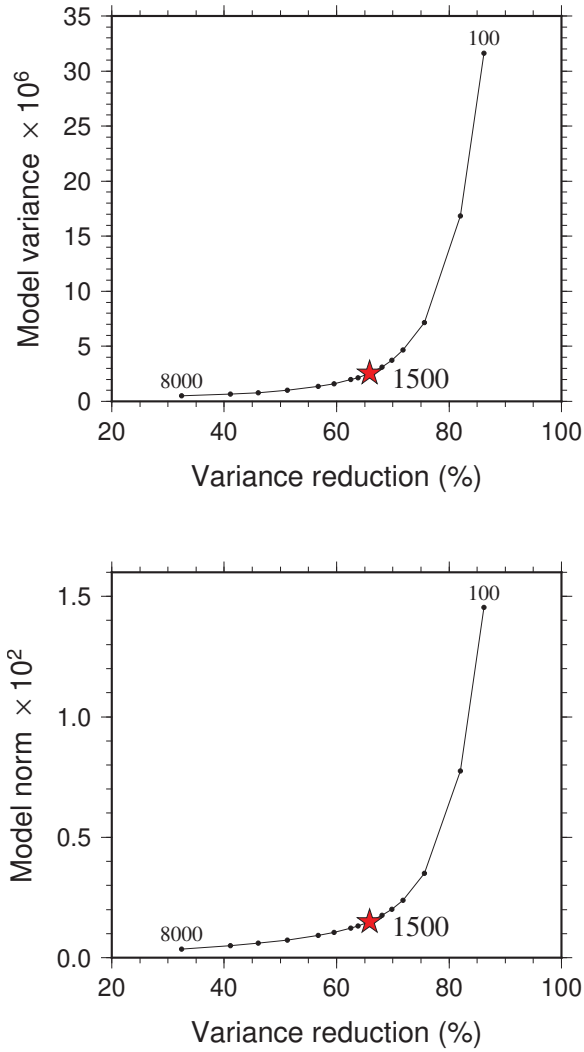

FIGURE 5.4: Trade-off curve between model norm, model variance and variance reduction rate for different damping parameters. The red star indicates the damping factor selected in this study.

we construct the conventional trade-off curve (or $L-$curve) of variance reduction rate versus model norm and model variance (Fig. 5.4). The trade-off curves are calculated by performing numerous individual tests with different damping factors ranging from 100 to 8000. By inspecting the inflection point of the $L-$curves and comparing the output velocity model with different damping factors, the optimum damping is selected as 1500 in this study. This selection can produce a relatively reasonable model without much contamination from observational errors. Finally, the choice of this damping factor in tomography gives the variance reduction rate of ~65.8% (Fig. 5.4).

The robustness of the tomographic results can be evaluated by the diagonal value of $\mathbf{G}^T\mathbf{G}$, where $\mathbf{G}$ is the Gram matrix in function 5.4, $\mathbf{G}^T$ is the transpose of the Gram matrix $\mathbf{G}$. Typically, $\mathbf{G}^T\mathbf{G}$ is analogous to the resolution matrix that can provide an estimation on

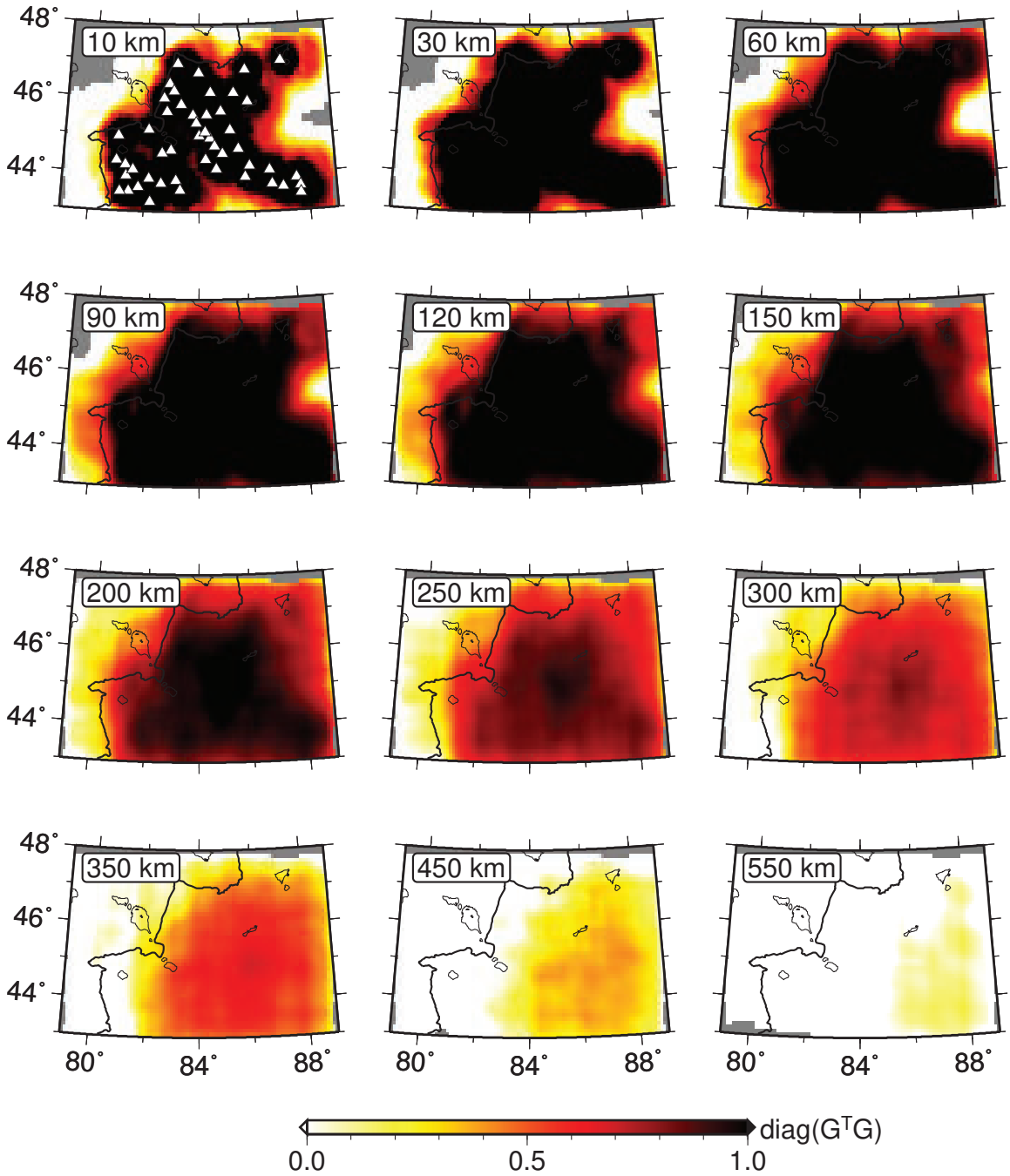

FIGURE 5.5: Maps of diagonal components of the matrix $\mathbf{G}^T\mathbf{G}$ on a logarithm scale at different depths, where $\mathbf{G}$ is the Gram matrix from 3D finite-frequency kernels. The value of $diag(\mathbf{G}^T\mathbf{G})$ represents the overall sensitivity of the traveltime data contribute to each grid node.

how the reveled model can be constrained by the input data. The spatial distribution maps of the diagonal elements of $\mathbf{G}^T\mathbf{G}$ on a logarithm scale are illustrated in Fig. 5.5 for 3D finite-frequency sensitivity kernels and in Fig. 5.6 for ray theory. In these $\mathbf{G}^T\mathbf{G}$ maps, if the value of $diag(\mathbf{G}^T\mathbf{G})$ is close to 1, that means the revealed model can be well-constrained by the input data and very close to the 'real model'. In contrary, the resolving power of the input data is extremely low when the $diag(\mathbf{G}^T\mathbf{G})$ approaches zero. In general, the 3D

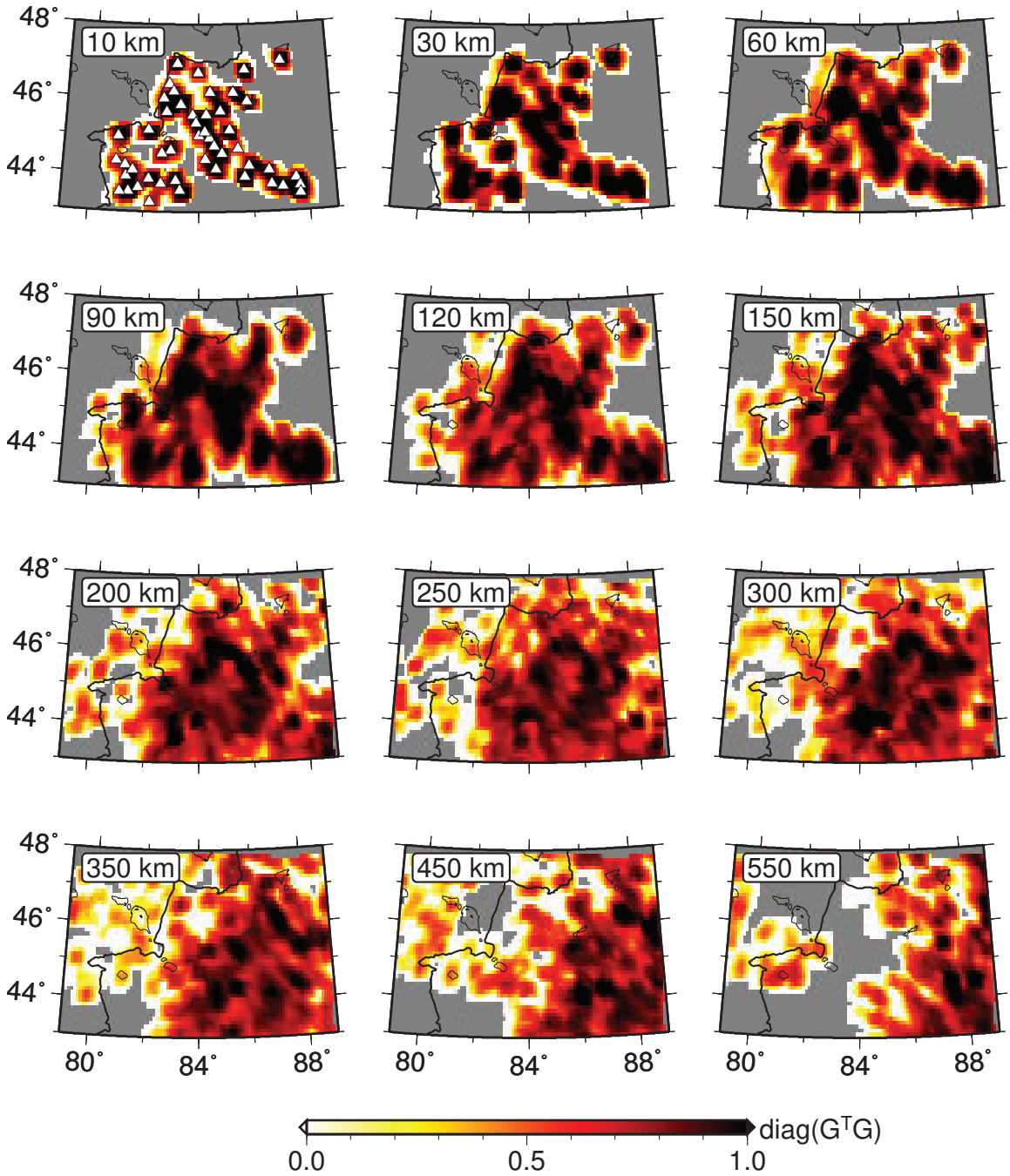

FIGURE 5.6: Same as figure 5.5 but the Gram matrix is built from ray theory. Note the distribution of the $diag(\mathbf{G}^T\mathbf{G})$ values are apparently localized beneath seismic stations compare to figure 5.5.

finite-frequency kernels sample a wider range of structures than geometrical rays assumed in traditional ray theory tomography, especially at shallow depths where ray theory only provides localized sensitivities near seismic stations (see Fig. 5.6). Meanwhile, the sensitivities from 3D kernels is more uniform across the entire study region compared to ray theory. Because ray theory assumes waves propagate along geometrical lines regardless of the perturbations off the ray path, while finite-frequency kernels accounts for the off-ray sensitivity, the value

of $diag(\mathbf{G}^T\mathbf{G})$ from the 3D kernels decreases sharply at deeper depths, contrary to ray theory.

5.5 Results

5.5.1 Resolution tests

To have a clear view on the resolution of this finite-frequency tomography, several checkerboard resolution tests are carried out (Fig. 5.7 to Fig. 5.11). The input velocity anomalies for all the checkerboard tests are set to ±2% from the regional average velocity, the modelled velocity anomaly sizes vary from approximately 100 km (4 × 4 nodes) to 200 km (8 × 8 nodes) horizontally and from 150 km (15 vertical nodes) to 200 km (20 vertical nodes) vertically. Checkerboard resolution tests are carried out based on the same ray paths and parameters as in the real input data. Fig. 5.7 plots the results of the checkerboard tests at shallower depths (< 100 km) with the horizontal anomaly size of ~100 km × 100 km. At shallow depths such as 20 km, the resolving ability is extremely poor and almost all the modelled anomaly cannot be recovered well by the input data (Fig. 5.7b). Even though we employ the 3D finite-frequency kernels, the sub-vertical rays and the relatively narrow width of Fresnel zone at shallow depths make the near surface structures almost unsolvable. The poor resolution at shallower depths is also reflected by the localized $diag(\mathbf{G}^T\mathbf{G})$ values in Fig. 5.5. When depths increase to 50 km (Fig. 5.7c), the input anomalies are well recovered in most of the study region covered by stations but faded towards the margins. Smearing effects are inevitable in body wave traveltime tomography when the sources are not homogeneously distributed. Since most of the events used in this study are located to the east and south of the array with the back azimuths between 90° to 180° (Fig. 5.2), smearing effects are observed in the checkerboard tests with anomalies smeared along the ray paths directions (along NW-SE). The smearing effects are more distinct in the vertical checkerboard profiles as shown in Fig. 5.10. Thus, particular attention should be paid when interpreting velocity perturbations. Checkerboard tests with larger anomaly sizes are illustrated in Fig. 5.8 (~150 km horizontally) and Fig. 5.9 (~200 km horizontally). The input anomalies are generally well recovered for depths shallower than 500 km. Therefore, we only focus on the velocity perturbations in the upper 500 km in the following discussion.

In addition, several resolution tests on vertical profiles with different anomaly sizes are shown in Fig. 5.10 and Fig. 5.11. In the east-west trending profile BB' in Fig. 5.10, the input

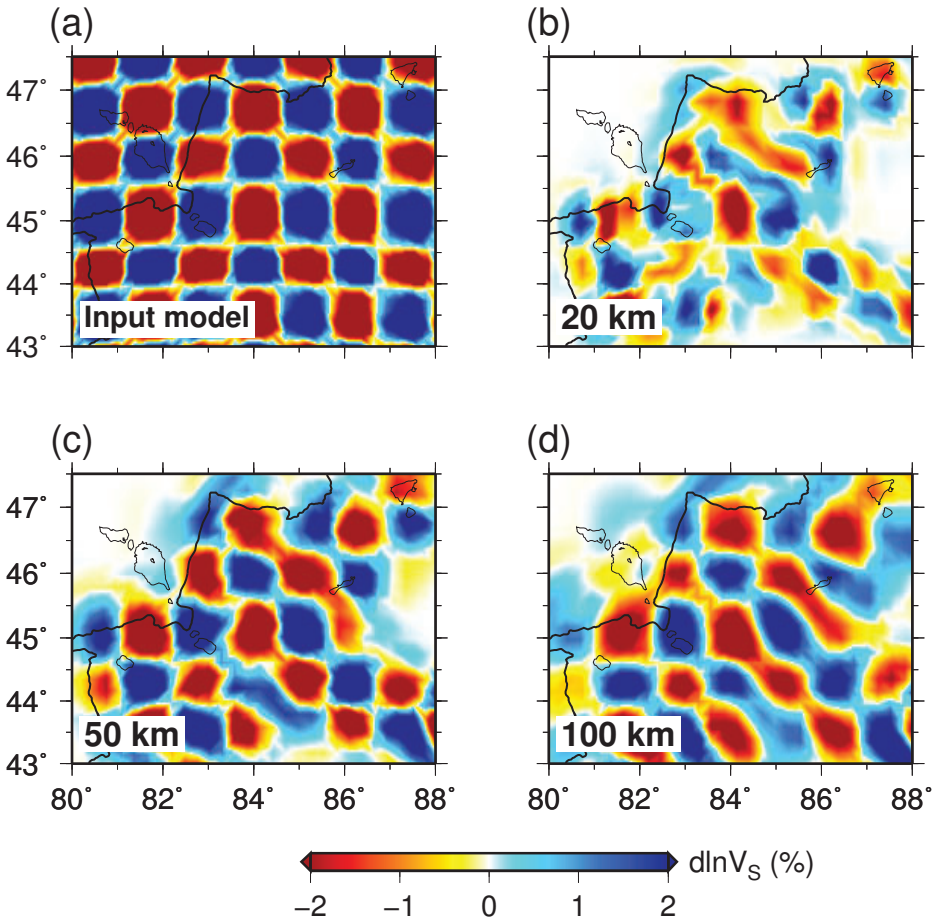

FIGURE 5.7: Checkerboard resolution test at shallower depths with the input anomaly shown in (a). The anomaly size is set to ~100km horizontally (4 × 4 nodes). (b), (c) and (d) The recovered anomaly at depth of 20, 50 and 100 km, respectively.

anomalies at longitude greater than 85° are heavily distorted toward east at depths deeper than 100 km due to the large number of event to the southeast . For the north-south trending profile in Fig. 5.11, the smearing effects are smaller, and nearly all the input anomalies with different sizes are well-constrained. A common feature shared in these profiles are the poor resolving ability at depths shallower than ~50 km and the damped perturbation values at depths over 300 km. Therefore, in the final velocity model, velocities in the upper 50 km should be not interpreted, while the velocities at greater depths may be underestimated and distorted along the ray paths.

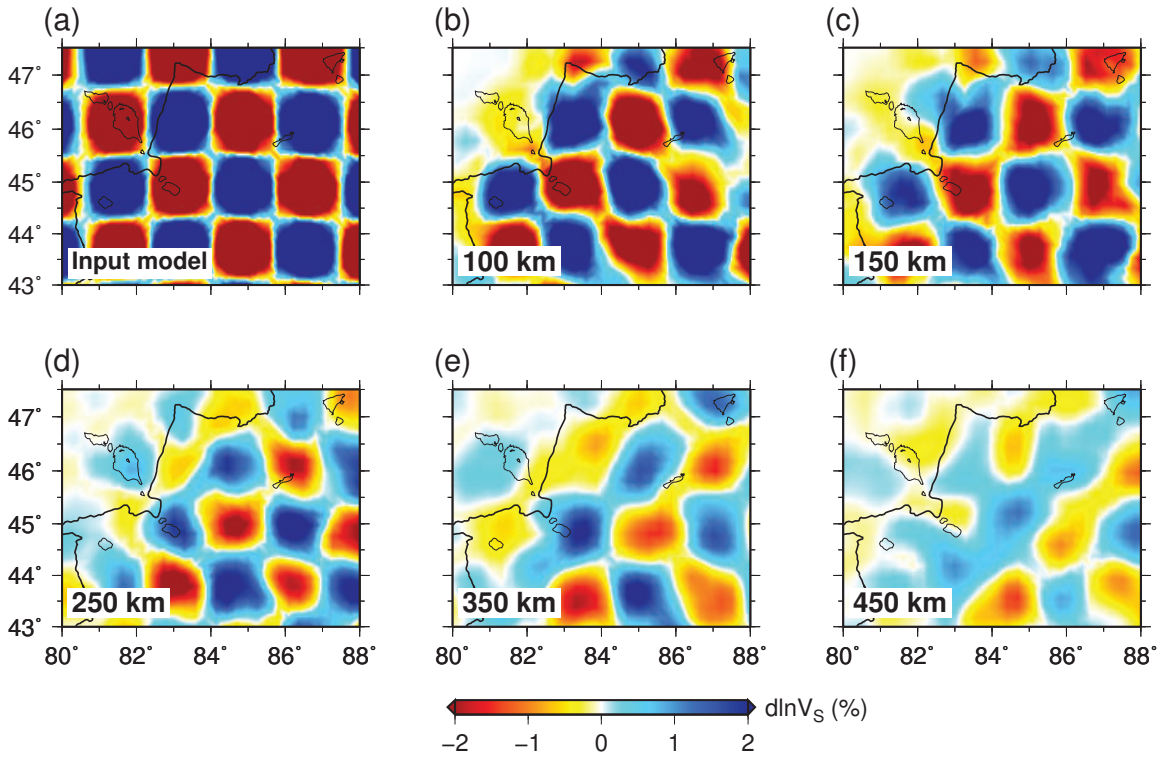

FIGURE 5.8: Checkerboard resolution test with input anomaly size of ~150km horizontally (6 × 6 nodes). The recovered anomaly at depth of 100, 150, 250, 350 and 450 km are illustrated in (b) to (f).

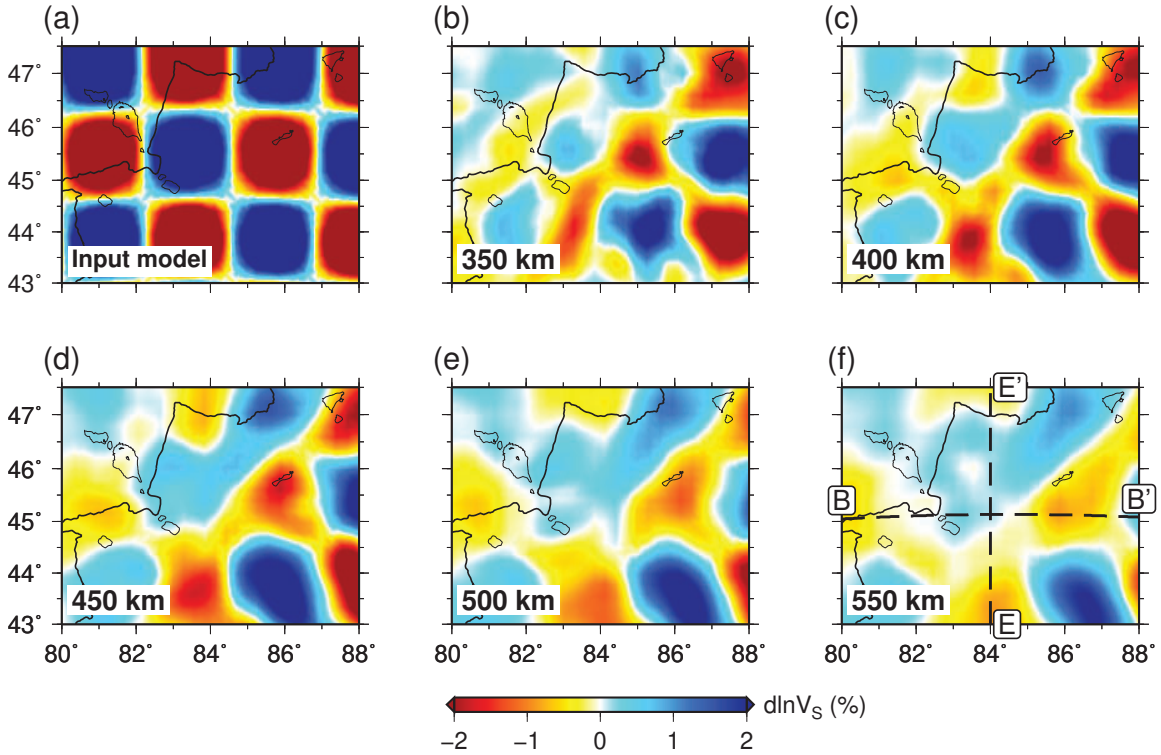

FIGURE 5.9: Checkerboard resolution test with larger input anomaly size of ~200km horizontally (8 × 8 nodes). The recovered anomaly at depth of 350, 400, 450, 500 and 550 km are illustrated in (b) to (f).

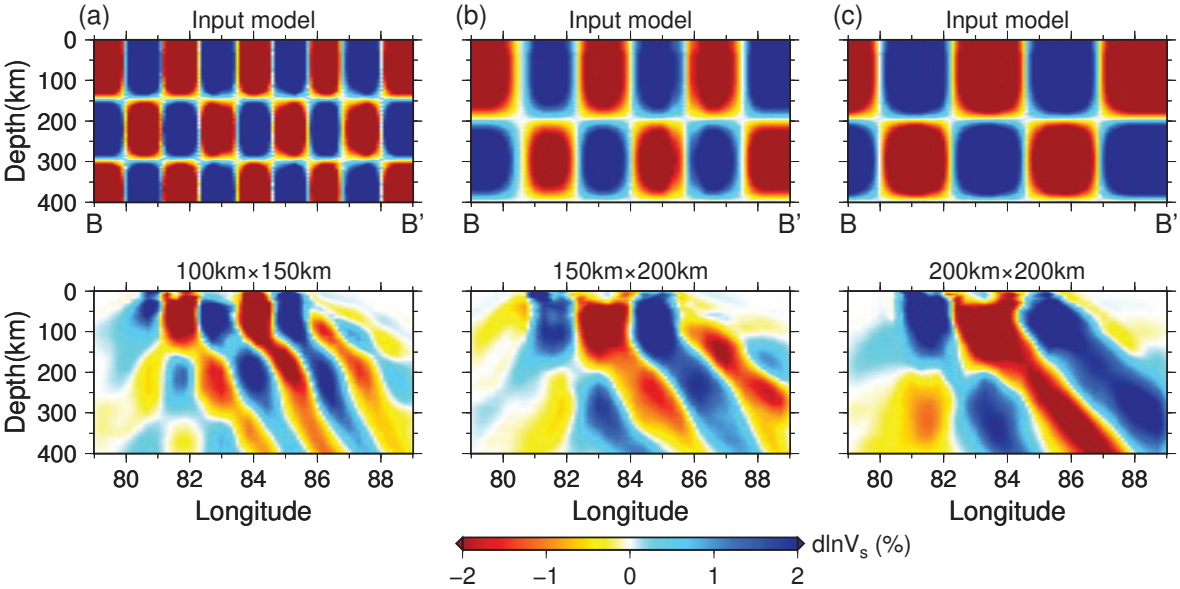

FIGURE 5.10: Checkerboard resolution test for vertical profile BB', the location of the profile is shown in figure 5.9f. The input anomaly size is given on top of each subfigure. Note that the recovered anomaly is heavily distorted at longitude greater than 85° due to the unevenly distributed sources.

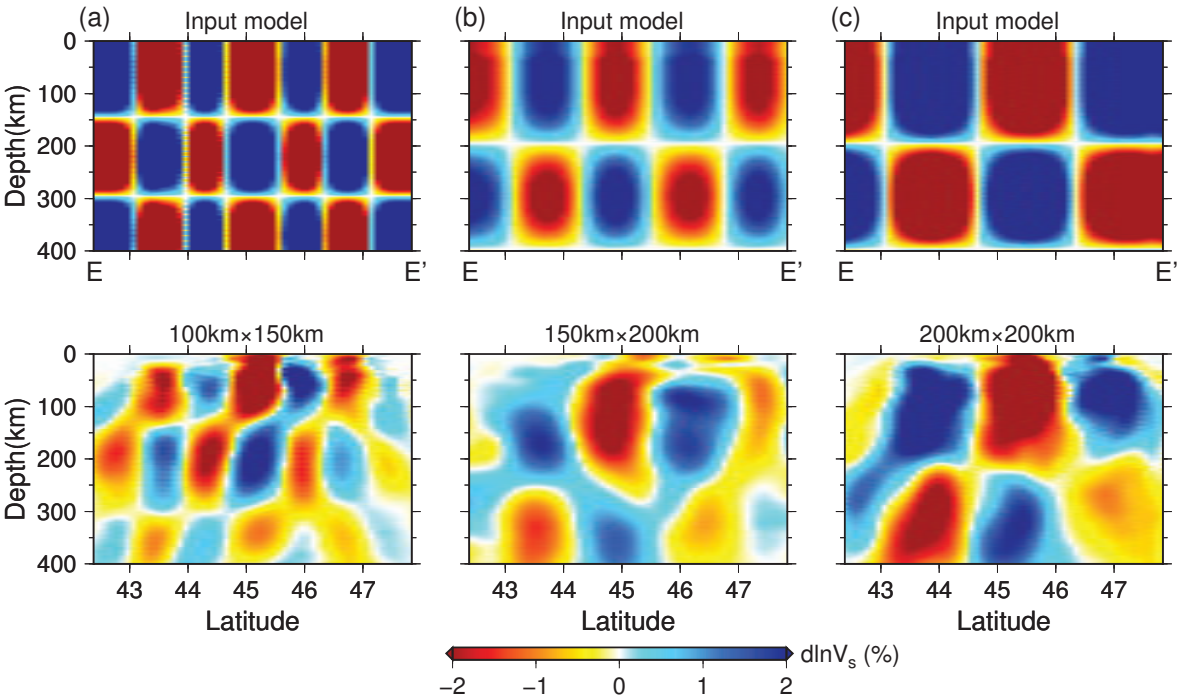

FIGURE 5.11: Same as figure 5.10 but for checkerboard test of vertical profile EE' with different input anomaly size.

5.5.2 3D *Vs* model

The inverted *Vs* model is given in Fig. 5.12 as horizontal slices and in Fig. 5.13 and 5.14 as vertical profiles. Because the data and methods applied in this study are not capable for

distinguishing small-scale anomalies (see resolution tests in section 5.5.1), anomalies with spatial lengths smaller than 50 km are filtered out by applying a Gaussian filter prior to plotting. Since the shallower structures are considered unreliable in the body wave traveltime tomography as described before, velocity structure of the shallower depths are not discussed here.

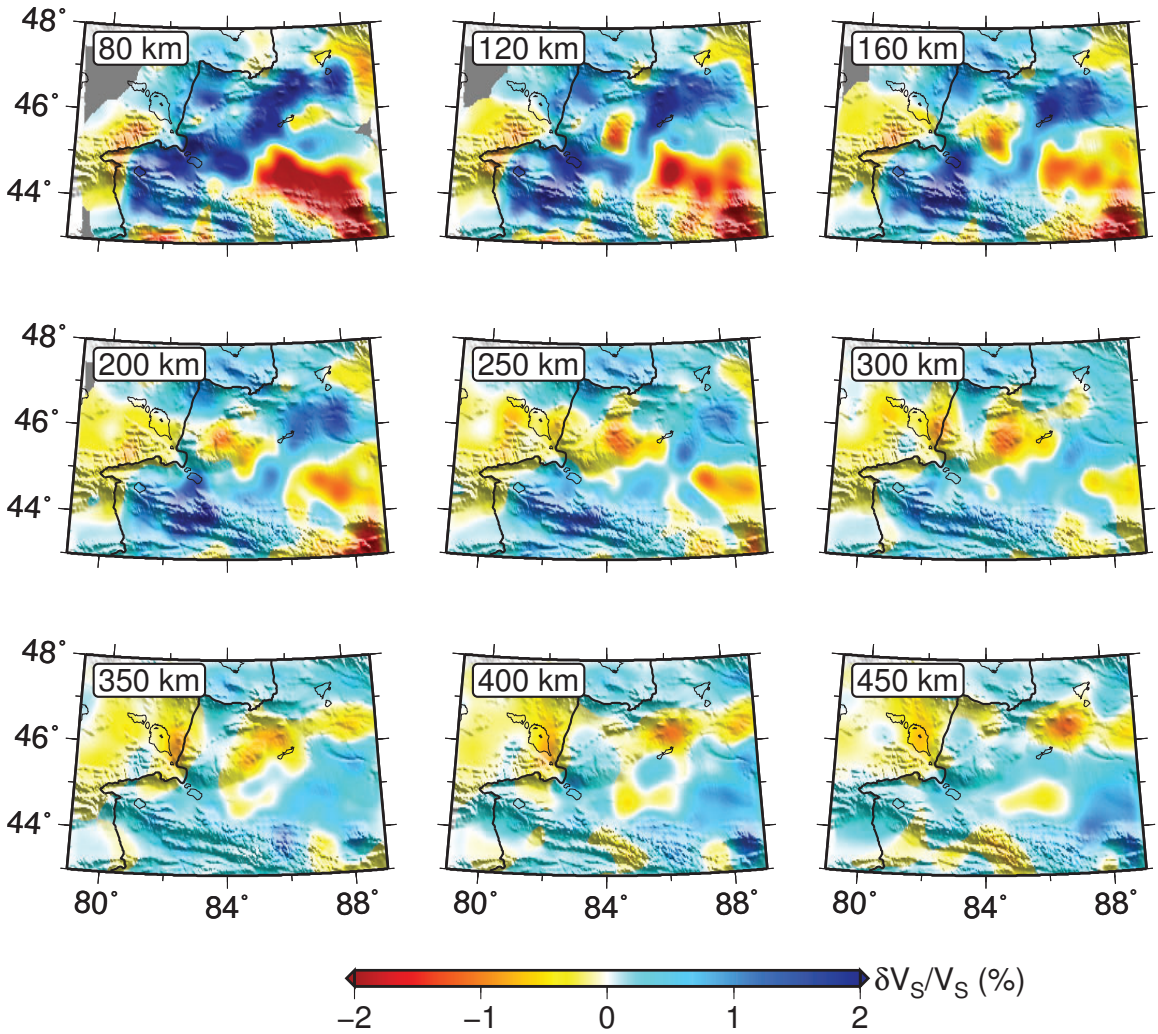

FIGURE 5.12: 3D shear wave velocity anomaly maps at different depths from body wave traveltime finite-frequency tomography.

At greater depths (> 80 km), one intriguing feature in the *Vs* model is the emergence of a low velocity anomaly beneath WJ. This low velocity anomaly begins to appear at depth of ~120 km and gets wider with increasing depth, and eventually disappears and is replaced by a high velocity anomaly over 350 km. Prominent and continuous high velocity anomalies are observed underlying the NTS at the upper mantle, the magnitude of this high velocity body decreases from over 2% at 120 - 200 km to less than 1% over 300 km. However, the variation at greater depths may be underestimated as shown in the checkerboard tests in Fig. 5.8. The

upper mantle structure (80 - 300 km) of JB can be divided into two parts, the east part with low velocities and the west with a narrow NE-SW striking high velocity belt. At depths over 350 km, low velocities in the eastern JB are then replaced by high velocity anomalies. In the western part of the study, continuous low velocities dominate the upper mantle of the Kazakh terrain. The low velocity beneath WJ at depths of 200 - 300 km is connected with the low velocities in the Kazakh terrain, but the reliability of this connection feature still needs to be investigated.

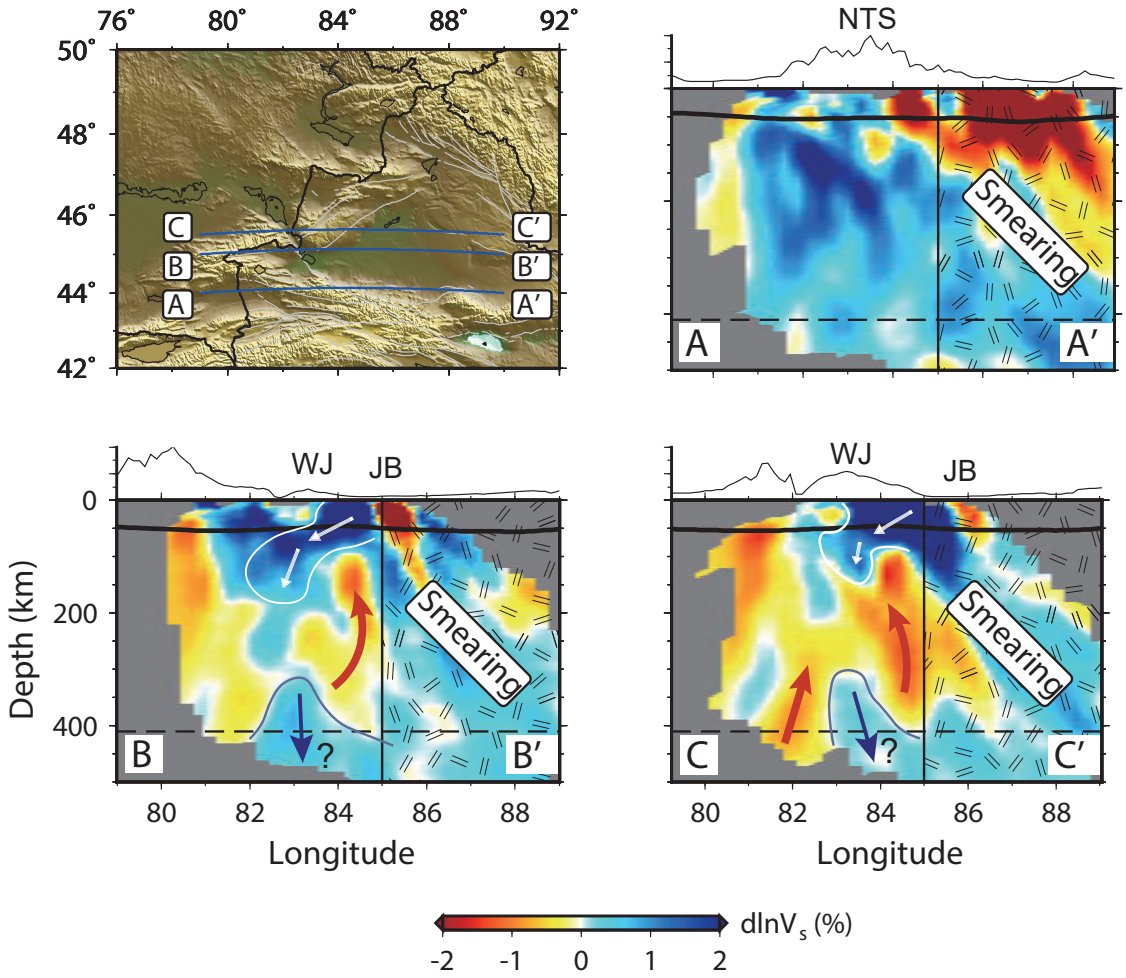

FIGURE 5.13: Vertical profiles of *Vs* along AA', BB' and CC', locations of these profiles are shown in the first subfigure. Major tectonic regions are given on top of each profile and the Moho interface in each profile is denoted as black bold lines. Arrows illustrate the possible fossil subduction slab and the upwelling materials. Areas heavily influenced by the smearing effect are covered by the gray boxes and neglected during interpretation.

Several vertical profiles are given in Fig. 5.13 and 5.14. In the AA' profile shown in Fig. 5.13, low velocities are imaged beneath the northern edge of NTS (also the southern margin of JB), and this low velocity body is obviously distorted towards east with depth. The

rest of the NTS is underlain by extensive high velocities as described in horizontal slices in Fig. 5.12. In BB' and CC' profiles, similar smearing effects are found for longitude larger than 85°. Therefore, in these profiles, velocity anomalies in the longitude greater than 85° are considered distorted and masked with gray boxes. Within the 'undistorted' area, a high velocity zone with the perturbation over 2% are found in the crust and uppermost mantle beneath the eastern part of WJ in BB' and CC' profile. This high velocity anomaly slightly dips towards west with depth but disappears at depths greater than 200 km in BB' and 150 km in CC' profile. Underlying these high velocities, a large low velocity anomaly with magnitude of -1% to -2% is found in both BB' and CC' profile. In the CC' profile, the low velocity body between 82° to 84° is connected with the low velocity in the Kazakh terrain at depths from 200 km to 300 km. However, this low velocity connection is not distinct in the BB' profile.

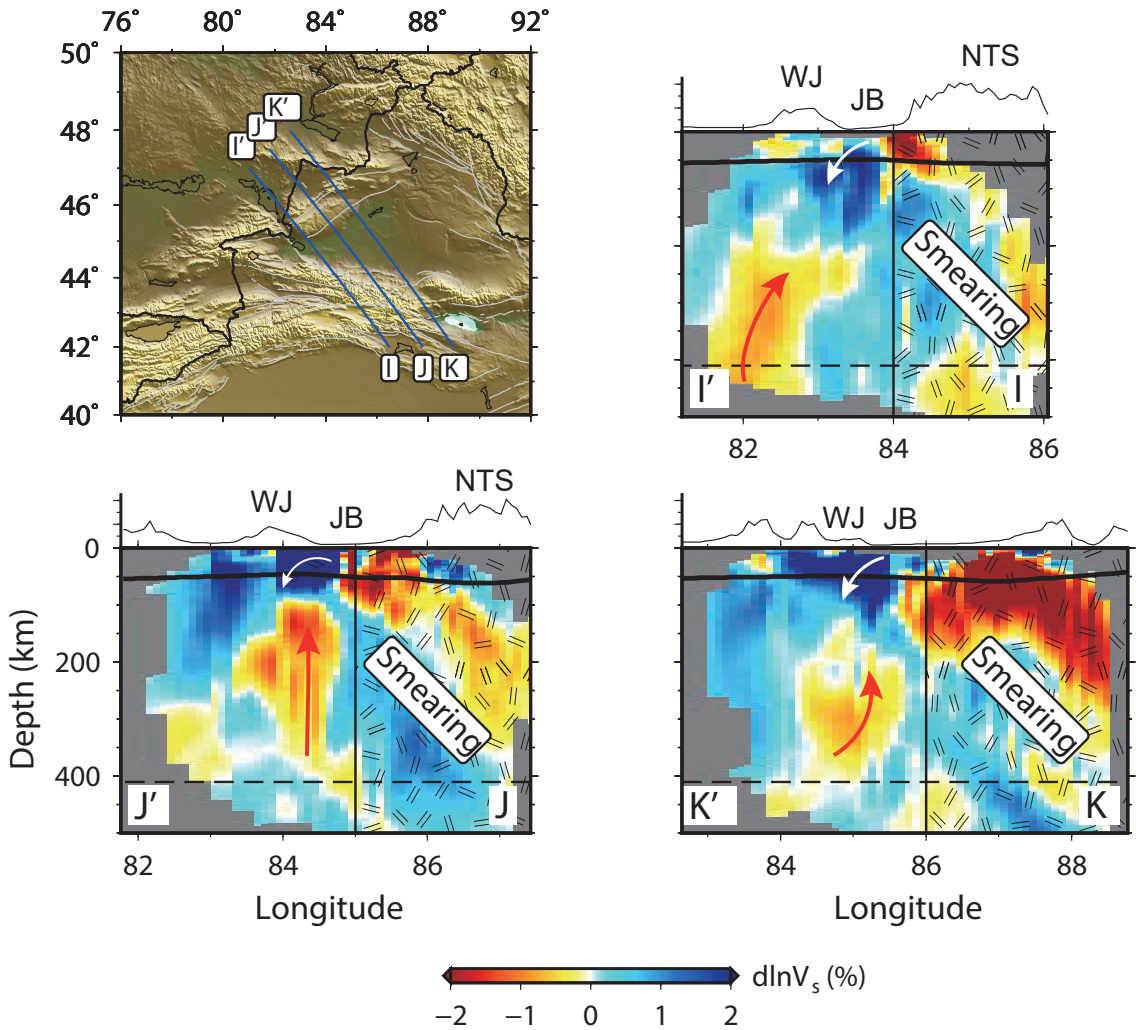

FIGURE 5.14: Same as figure 5.13 but for vertical profiles along II', JJ' and KK'.

Fig. 5.14 illustrates another three profiles across the WJ along the SE-NW direction.

Ignoring the distortion caused by smearing effects (masked by gray boxes in Fig. 5.14), the rest velocity features are very similar to BB' and CC' profiles. The strong low velocity body with magnitude of -1% to -2% is observed beneath WJ at depths from 150 km to almost 400 km. This low velocity anomaly is sandwiched by high velocities between the crust/uppermost mantle and deeper depths at ~400 km beneath WJ. Also, large high velocities dominate the northwestern part of WJ at all depths. Several other profiles along the S-N direction (DD', EE', FF') are given in the supplementary materials Fig. 5.15.

5.6 Discussion

Since the modern type of subduction process may begin at the late Proterozoic [Stern, 2005] or as early as the Archean [Smithies et al., 2007]. Some modern subduction features (such as the chemical composition for subducting slabs, density and subduction dynamic processes etc.) are similar for subductions in the CAOB at the late Paleozoic. It is well documented that the WJ region has experienced complex subduction processes during the late Paleozoic with contentious subduction models [Windley and Xiao, 2018, Xiao et al., 2010]. The emplacement of ophiolites along the Darbut fault (located in the central WJ) during the Paleozoic indicates that the WJ may be underlain by some remnants of oceanic crust or exhumed subducted rocks [Chen et al., 2014, Yan et al., 2015]. Within the crustal and uppermost mantle structures in this region, some relics of late Paleozoic subducted oceanic slabs are found mainly through the MT and surface wave tomography. In the MT images, low resistivity bodies are observed underlying the western margin of JB and penetrate northwestward into WJ [Xu et al., 2016, Zhang et al., 2017]. These low resistivity anomalies are interpreted as the result of dehydration and decarbonization processes together with greenschist breakdown [Jones, 1993, Wannamaker et al., 2009] or correspond to the hydrated basalts of the subducted slab.

From surface wave tomography images, high shear wave velocity bodies are imaged in the crust and uppermost mantle of WJ [Wu et al., 2018] and interpreted as the fossil subduction oceanic slabs in correspondence with MT conductors. Furthermore, borehole data suggest that the JB is underlain by Paleozoic oceanic crustal rocks [Zheng et al., 2007]. All these lines of evidence indicate the existence of a well-preserved Paleozoic subduction slab in the Junggar terrain. To reconstruct the tectonics in the WJ, a late Paleozoic failed subduction

model with polarity of northwest in the WJ are proposed [Wu et al., 2018, Xu et al., 2016]. The mechanism for the failed subduction of Junggar oceanic slab in the late Paleozoic is possibly related to the unique tectonic evolution in the final stage during the formation of the CAOB. The complicated Paleozoic amalgamations (including the oroclinal bending and collision of several adjacent blocks) at the Junggar terrain of CAOB make the ancient Junggar ocean (part of Paleo-Asian ocean) develop into a trapped small ocean [Xiao et al., 2008, 2015b], which is responsible for the termination of the subduction at the western margin of the ocean (current day WJ).

The fossil relicts of the failed subduction slab are imaged in our previous surface wave tomography model as a high velocity zone (Vs > 4.7 km/s) at the uppermost mantle of JB and WJ. A model of northwestward subduction with a detached or melted slab at greater depths beneath WJ is proposed based on the shear wave velocity model. We discuss possible mechanisms for the survival of this remnant slab in the upper mantle (see chapter 4). In the body wave model here, the high velocities in the crust and uppermost mantle depths (< 150 km) beneath WJ in profile BB' and CC' (Fig. 5.13) are also imaged and considered as the remnant slab which in consistent with our previous model. Because the velocity patterns in the eastern part of the study region (> 85° in BB' and CC') are severely influenced by the smearing effects and there is a lack of absolute velocity values from body wave tomography, we do not discuss much about the shallower velocity structures (< 150 km) from body wave tomography and only focus on deeper structures.

For the deeper velocity structures (> 200 km), an extensive low velocity anomaly (-1% to -2%) is observed beneath WJ and the Kazakh terrain in profile BB' and CC'. A high velocity anomaly with the magnitude of ~1% is found underlying the low velocities at the depth of ~400 km. By considering the slightly damped anomalies at greater depths as illustrated by checkerboard tests (Fig. 5.8), this high velocity body at 400 km depth may have an even higher magnitude. Two possible interpretations are proposed for the origin of this deep high velocity anomaly.

The first interpretation is that these deep high velocities are ancient subducted oceanic slab materials trapped and accumulated in and above the mantle transition zone. Based on our previous *Vs* model from surface wave tomography, a well-preserved remnant Paleozoic slab is revealed beneath JB, penetrating northwestward to the uppermost mantle of WJ but disappearing at depths deeper than 150 km. It is natural to postulate that the already subducted

slabs have sunk into the deeper mantle. The remaining question is whether these cold and dense oceanic slabs can accumulate and stagnate in the mantle transition zone for such a long-time span.

Numerous seismic tomography studies demonstrate that some modern subducting oceanic slabs are, in fact, flattened and broaden in the mantle transition zone with depths ranging from 400 km to 1000 km [Fukao et al., 1992, 2009, 2001, Li et al., 2013, van der Hist et al., 1991, Zhao et al., 2009]. These stagnant slabs, imaged with high seismic velocities, are widely distributed in western Pacific ocean [King et al., 2015]. Mechanisms to explain this phenomenon are proposed in terms of the increased mantle viscosity and the slow diffusion effect [King et al., 2015, Marquardt and Miyagi, 2015, van Mierlo et al., 2013]. High-resolution numerical simulations by King et al. [2015] demonstrates that the pyroxene in the interior of a cold subducting slab may maintain its original status and unlikely transform into garnet at equilibrium pressure and temperature. In another word, despite the great pressure and temperature at mantle transition zone depths, the slow diffusion effect inhibits the dissolution of pyroxene inside the subducted slab, and thus, the subducted slab may remain buoyant and resist further subsidence. Their simulation shows that the stagnant slab will remain sub-horizontal for tens of million years but eventually will penetrate into lower mantle [King et al., 2015]. Other modelling studies indicate that viscosity increase in the lower mantle across the transition zone is also one of the main reasons to explain the slab stagnation [Chen and King, 1998, Gurnis and Hager, 1988, Marquardt and Miyagi, 2015]. Modelling by Marquardt and Miyagi [2015] shows that the viscosity in the upper 900 km of lower mantle surrounding the subducting slabs may increase 2.3 orders of magnitude. This increase in the viscosity prevents the slabs sinking into the deeper mantle, resulting in the subducted materials accumulated in or near the mantle transition zone.

It should be noted that the above two mechanisms are proposed to account for the stagnation of modern subducting slabs. For ancient subductions that happened a long period of time ago in the CAOB, stagnation hypothesis then becomes challenging. Fortunately, a number of fossil subduction slabs are imaged by seismic tomography studies [Gorbatov et al., 2000, Sol et al., 2002, Van der Voo et al., 1999, Wang et al., 2013], which allow us to examine the geometry and behavior of the ancient subducted slabs. The discovery of the Mesozoic subducted slabs in Siberia [Van der Voo et al., 1999] demonstrates that a fossil slab can survive for a long period time in the mantle. By carefully examining the velocity profiles

by Van der Voo et al. [1999], we find that some of this fossil slabs are actually stagnant and become accumulated within and on top of the mantle transition before subducting to the lower mantle (high velocity bodies surrounding the mantle transition zone in figure 3 of Van der Voo et al. [1999]). Therefore, in this study, a more possible situation is the fossil slabs have already sinking to lower mantle but with some materials still trapped within and on top of the mantle transition zone. However, due to the limitation of research scale in this study, we cannot resolve the structure beneath 500 km, which hinders the verification of this assumption.

Another interpretation for the deep high velocities in the profile BB' and CC' is that they could be related a downwelling limb within a small-scale mantle convection system in the study region. Since the discovery of widely distributed ridge-generated magmas in WJ [Windley and Xiao, 2018], numerous contradictory ridge subduction models are proposed [e.g. Geng et al., 2009, Jiang et al., 2010, Ma et al., 2012, Tang et al., 2010, Zhang et al., 2011b]. Most features of ancient ridge subductions are similar to the modern ongoing ocean ridges, involving subductions such as in the north and south America [Windley and Xiao, 2018]. The upwelling of asthenospheric mantle through the opened slab window (subducted ocean ridge) triggers local upper mantle convections, and partial melting of the subducted oceanic crust and lower continental crust, forming the special ridge-generated magmas at the forearc and/or near trench locations. Therefore, the low velocities in BB' and CC' profiles at 150 to 350 km depths may correspond to the remnant recordings of the hot upwelling asthenospheric mantle triggerred by the opening of slab window beneath WJ, while the underlying high velocities may correspond to a downwelling limb in response to the upwelling. Because body wave tomography utilizes relative traveltimes, we cannot get the absolute mantle velocity values and therefore cannot estimate the temperature in the study region. Further evidence is needed to rule out the possibility of this convection hypothesis.

5.7 Conclusions

Based on the seismic data recorded by 49 stations across the Junggar terrain, a new upper mantle shear wave velocity model is constructed from body wave traveltime finite-frequency tomography technique. This model reveals a high velocity anomaly beneath WJ and we interpret it as the remnant of the Paleozoic subduction oceanic slabs subducting northwestward in

the past. High velocity anomalies are also observed beneath WJ at depth of ~400 km, which are considered as the trapped ancient subducted slabs or a downwelling limb within a small-scale mantle convection system beneath WJ. Above the 400 km depth high velocity bodies beneath WJ, low velocities with magnitude of -1% to -2% are imaged at depths between 150 km to 350 km. These low velocities are possibly the relicts of upwelling asthenospheric mantle materials through the slab window.

5.8 Supplementary materials

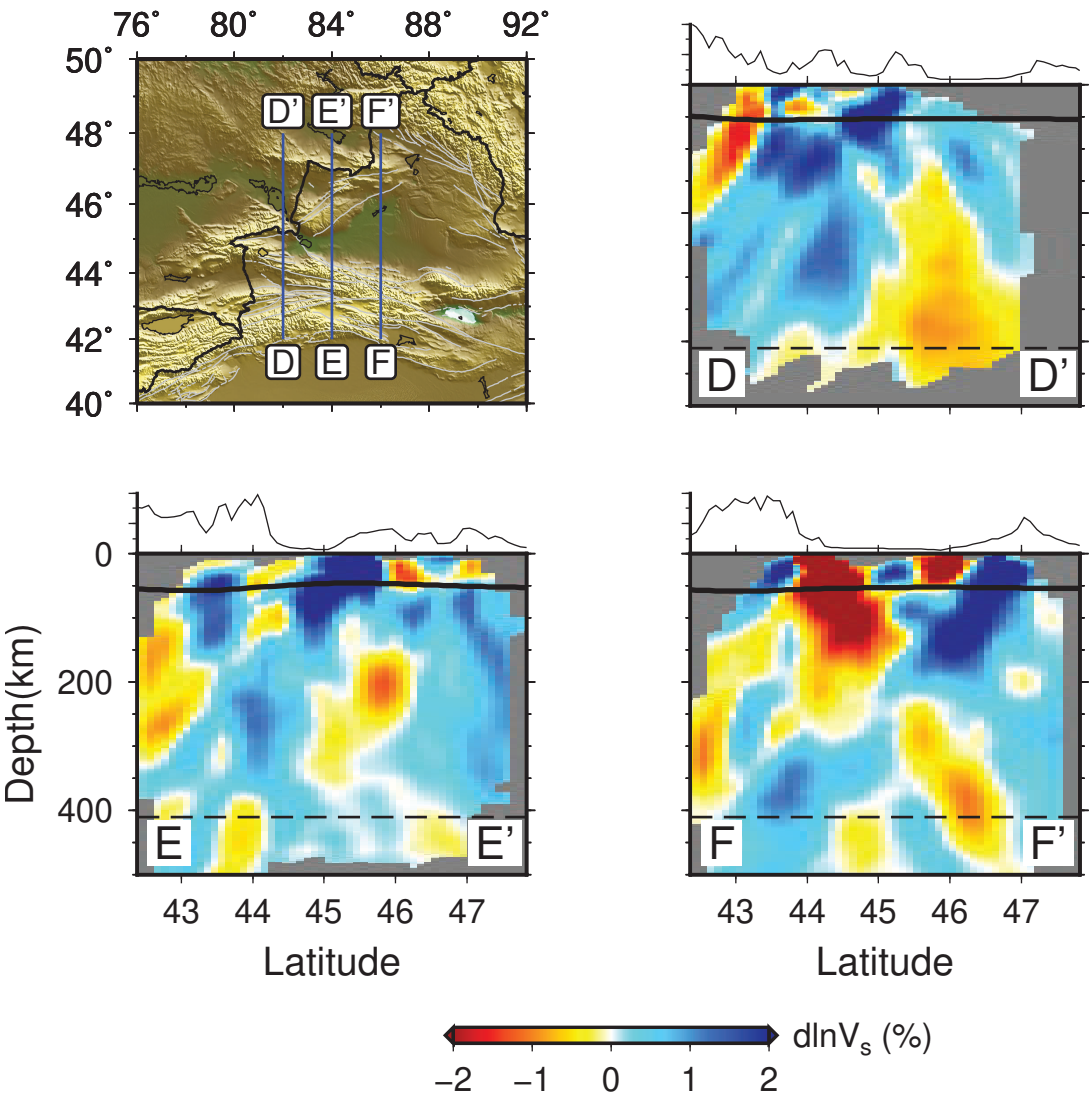

FIGURE 5.15: Vertical profiles of *Vs* along DD', EE' and FF'.

6

Conclusions and Outlooks

Seismic tomography is an important tool that not only provides information on the composition of the Earth's interior but also helps to understand the tectonics. The main aim of this thesis is to build high-resolution seismic velocity models of the Junggar terrain, northwestern China and then understand its tectonic evolutions.

Based on two seismic arrays deployed in the Junggar terrain from 2013 to 2017, high-resolution shear wave velocity models of the crust and upper mantle are constructed by using ambient noise tomography (ANT) (chapter 3 and 4), the two-plane surface wave tomography (TPWT) (chapter 4) and the body wave traveltime finite-frequency tomography (chapter 5) techniques. The combination of ANT and TPWT methods shows a great advantage in producing the high-resolution crustal and uppermost mantle velocity model, while the teleseismic body wave traveltime tomography, as a complement, provides constraints on the deeper structures. By incorporating regional structure geology, geochemistry and geodynamics, our 3D velocity models provide important clues on the tectonic evolution of the Junggar terrain and help constrain the subduction-collision-accretion history in this region as summarized below.

6.1 Conclusions

In chapter 3, seismic data from 31 temporary stations deployed in the western Junggar region in 2013 are utilized for receiver function and ambient noise tomography analyses. The Moho depth beneath each station is determined via the H-κ stacking method, while the Moho variations along three profiles are acquired by the CCP stacking technique. For the seismic stations located in the Junggar basin, neighborhood algorithm (NA) is introduced to estimate the thickness of the sedimentary layer. Our results reveal that the Moho depths vary significantly from 41 to 52 km with an average of 46 km across the western Junggar region, while the sediments thickness in the western Junggar basin varies from 1 km to over 8 km. The most prominent feature of the Moho variation is the depression in the juncture zone between the Zaire mountains and the western Junggar basin. This depression is probably associated with the paleo-subduction interface according to our interpretation. Apart from the Moho depths, the crustal shear wave velocity (*Vs*) structures are also generated by the ANT method. The velocity model reveals strong vertical variations of *Vs* beneath the Junggar Basin with the high-velocity middle/lower crust underlying the low-velocity upper crust. The high-velocity body in the middle/lower crust (> ~20 km) extends and dips northwestward into the Zaire mountains. By comparing the magnitudes of this high velocity body with the calculated shear velocity of averaged global middle/lower crust and various metamorphic facies of MORB, the northwestward dipping high-velocity body is interpreted as remnants of the Paleozoic oceanic slab. The regions of Zaire mountains and western Junggar basin are further interpreted as a well-preserved subduction system which have had developed before the Carboniferous and failed in the late Paleozoic. The failure of the subduction of Junggar oceanic slab in the late Paleozoic is possibly related to the oroclinal bending processes in the final stage during the formation of the CAOB. This well-preserved ancient subduction system is also supported by MT imaging [Xu et al., 2016].

In chapter 4, in order to image the deeper structures and trace the possible trapped fossil slabs in the Junggar region, a regional broadband seismic array consisting 49 stations were deployed in the Junggar region, Northwest China from Jul 2016 to Aug 2017. High-resolution *Vs* structures of crust and uppermost mantle in the Junggar terrain are produced by the combination of ANT and TPWT techniques. Compared to the *Vs* model in chapter 3, this new velocity model reveals velocity structures at a larger area and with greater depths. The new *Vs* model indicates that the entire Junggar basin is underlain by high velocity anomalies

in the middle/lower crust in correspondence with the previous results in chapter 3. In the upper mantle, nearly flat high velocities (> 4.7 km/s) are observed in the uppermost mantle (< ~120 km) beneath the Junggar basin. In the western margin of Junggar basin, this uppermost mantle high velocity body slightly dips towards northwest and disappears at depths over 150 km. By examining the geometrical shape of the high velocities and comparing the inverted geotherm with the predicted temperature from the half-space cooling (HSC) model, this high velocity body is interpreted as the remnant of the Junggar oceanic lithosphere. We discuss several mechanisms from the dynamics, viscosity and regional tectonics to explain the survival of this remnant slab in the uppermost mantle. According to the geometry of the high velocity body in the western margin of Junggar basin, we conclude that the last subduction scenario of the Junggar ocean in the western Junggar (WJ) is with the polarity of northwest. The lack of continuous high velocity anomaly beneath WJ in the upper mantle indicates that this fossil subducted slab may have already broken off when the subduction failed.

In chapter 5, a 3D *Vs* model of the whole upper mantle in the Junggar terrain is constructed by body wave traveltime finite-frequency tomography based on data from the same seismic array in chapter 4. The body wave traveltime tomography provides extra constraints on deeper structures (> 200 km) compared to the surface wave tomography alone. The velocity model from the body wave tomography shows some similar features in the lower crust and uppermost mantle as the surface wave tomography. A high velocity anomaly beneath WJ and the western margin of the Junggar basin at depths shallower than 150 km is imaged and interpreted as the remnant of the Paleozoic subduction oceanic slab. A high velocity anomaly is also observed beneath WJ at a depth of ~400 km, which is considered either as the trapped and stagnant ancient subducted slabs or a downwelling limb within a small-scale upper mantle convection system beneath WJ. Overlying the high velocity bodies beneath WJ, low velocities with magnitude of -1% to -2% are imaged between 150 km to 350 km. We relate these low velocities to the upwelling asthenospheric upper mantle which was possibly triggered by the opening of the slab window or the subsidence of the detached oceanic slab beneath WJ.

By investigating the subsurface velocity structures in the Junggar terrain of NW China using different types of seismic tomography techniques, the relevant tectonics and evolution are discussed in this thesis. The new high-resolution 3D velocity models in the Junggar terrain

undoubtedly provide vital constraints on the debated evolutionary models in this region. The existence of possible fossil oceanic slabs in the Junggar terrain are crucial indicators to unveil the mysterious evolution history in the Junggar region. More importantly, the Junggar region, with its unique evolutionary history allowing the preservation of the ancient tectonic activities, provides a nature laboratory to study the fossil subductions and related dynamics.

6.2 Outlooks

In this thesis, I build a shear wave velocity model of the crust and upper mantle of the Junggar terrain using surface wave and body wave tomography. For surface wave tomography utilizing the fundamental Rayleigh waves, the resolution at depths greater than ~250 km dramatically decreases. For body wave traveltime tomography, the subvertical distribution of teleseismic body wave ray paths in the shallower depths result in a very poor sensitivity for shallower structures. Therefore, the complementary sensitivity of teleseismic body wave traveltimes and surface waves give rise to the idea of joint inversion combining these two datasets. Through the joint inversion scheme, we can generate a velocity model with structures at all depths can be better constrained. A joint model provides a more comprehensive view on the velocity structure in the Junggar terrain and may help to better understand the tectonics in this region. Thus, the joint inversion of body wave traveltimes and surface wave phase velocity will be the first task in the future study.

Radial and azimuthal anisotropies are another two important characteristics that are highly associated with tectonics and dynamics. In general, both the radial and azimuthal anisotropy can be interpreted as the lattice-preferred orientations of certain minerals such as mica, and/or orientated structures like the layered sedimentary stratum, and/or shallow parallel microfractures. Information on the anisotropy is important as it can provide constraints on the structures that are closely associated with deformation. In my seismic tomography of this thesis, anisotropy effects are ignored and the output velocity models are assumed isotropic. The lack of the anisotropic models in the Junggar region may limit our understanding of the tectonic deformation in this region. Therefore, future works will use all the three-component seismic data to invert for radially and azimuthally anisotropic models.

In recent years, a new tomography method called ‘adjoint tomography’ has attracted the attention of many seismologists. This method employs full 3D numerical simulations in

forward modeling and shows a huge advantage in imaging structures with strong velocity contrasts [Liu and Gu, 2012]. By introducing the adjoint tomography into traditional ANT, several improvements are obvious: 1) no need to measure phase or group velocities, which eliminate the errors introduced by the dispersion measurements; 2) accurate 3D kernels are introduced to replace the conventional ray theory based tomography; 3) directly invert for the *Vs* structures instead of the two-step inversion scheme in traditional ANT. The application of the adjoint tomography on the seismic dataset in Junggar region will be carried out in the future aiming for a more accurate velocity model.

References

Abers, G. A. and Hacker, B. R. (2016). A MATLAB toolbox and Excel workbook for calculating the densities, seismic wave speeds, and major element composition of minerals and rocks at pressure and temperature. *Geochemistry, Geophysics, Geosystems*, 17(2):616–624.

Afonso, J., Fullea, J., Griffin, W., Yang, Y., Jones, A., Connolly, J., and O'Reilly, S. (2013a). 3-D multiobservable probabilistic inversion for the compositional and thermal structure of the lithosphere and upper mantle. I: A priori petrological information and geophysical observables. *Journal of Geophysical Research: Solid Earth*, 118(5):2586–2617.

Afonso, J. C., Fullea, J., Yang, Y., Connolly, J. A. D., and Jones, A. G. (2013b). 3-D multi-observable probabilistic inversion for the compositional and thermal structure of the lithosphere and upper mantle. II: General methodology and resolution analysis. *Journal of Geophysical Research: Solid Earth*, 118(4):1650–1676.

Afonso, J. C., Rawlinson, N., Yang, Y., Schutt, D. L., Jones, A. G., Fullea, J., and Griffin, W. L. (2016). 3-D multiobservable probabilistic inversion for the compositional and thermal structure of the lithosphere and upper mantle: III. Thermochemical tomography in the Western-Central U.S. *Journal of Geophysical Research: Solid Earth*, 121(10):7337–7370.

Agostinetti, N. P. and Chiarabba, C. (2008). Seismic structure beneath Mt Vesuvius from receiver function analysis and local earthquakes tomography: evidences for location and geometry of the magma chamber. *Geophysical Journal International*, 175(3):1298–1308.

Agostinetti, N. P. and Malinverno, A. (2010). Receiver function inversion by trans-dimensional Monte Carlo sampling. *Geophysical Journal International*, 181(2):858–872.

Aki, K., Christoffersson, A., and Husebye, E. S. (1977). Determination of the three-dimensional seismic structure of the lithosphere. *Journal of Geophysical Research*, 82(2):277–296.

Aki, K. and Lee, W. (1976). Determination of three-dimensional velocity anomalies under a seismic array using first P arrival times from local earthquakes: 1. A homogeneous initial model. *Journal of Geophysical research*, 81(23):4381–4399.

Allen, M. B., Windley, B. F., and Zhang, C. (1993). Palaeozoic collisional tectonics and magmatism of the Chinese Tien Shan, central Asia. *Tectonophysics*, 220:89–115.

Alsina, D., Snieder, R., and Maupin, V. (1993). A test of the Great Circle Approximation in the analysis of surface waves. *Geophysical Research Letters*, 20(10):915–918.

Assous, S. and Boashash, B. (2012). Evaluation of the modified S-transform for time-frequency synchrony analysis and source localisation. *EURASIP Journal on Advances in Signal Processing*, 2012(1):49.

Battaile, C. C. and Srolovitz, D. J. (2002). Kinetic Monte Carlo simulation of chemical vapor deposition. *Annual Review of Materials Research*, 32(1):297–319.

Beaumont, M. A. (2010). Approximate Bayesian computation in evolution and ecology. *Annual review of ecology, evolution, and systematics*, 41:379–406.

Bell, S., Ruan, Y., and Forsyth, D. W. (2016). Ridge asymmetry and deep aqueous alteration at the trench observed from Rayleigh wave tomography of the Juan de Fuca plate. *Journal of Geophysical Research: Solid Earth*, 121(10):7298–7321.

Bensen, G., Ritzwoller, M., Barmin, M., Levshin, A., Lin, F., Moschetti, M., Shapiro, N., and Yang, Y. (2007). Processing seismic ambient noise data to obtain reliable broad-band surface wave dispersion measurements. *Geophysical Journal International*, 169(3):1239–1260.

Bijwaard, H., Spakman, W., and Engdahl, E. R. (1998). Closing the gap between regional and global travel time tomography. *Journal of Geophysical Research: Solid Earth*, 103(B12):30055–30078.

Bodin, T., Sambridge, M., Tkalčić, H., Arroucau, P., Gallagher, K., and Rawlinson, N. (2012). Transdimensional inversion of receiver functions and surface wave dispersion. *Journal of Geophysical Research: Solid Earth*, 117(B2).

Boys, R. J., Wilkinson, D. J., and Kirkwood, T. B. (2008). Bayesian inference for a discretely observed stochastic kinetic model. *Statistics and Computing*, 18(2):125–135.

Brocher, T. M. (2005). Empirical relations between elastic wavespeeds and density in the Earth's crust. *Bulletin of the seismological Society of America*, 95(6):2081–2092.

Buckman, S. and Aitchison, J. C. (2004). Tectonic evolution of Palaeozoic terranes in west Junggar, Xinjiang, NW China. *Geological Society, London, Special Publications*, 226(1):101–129.

Buslov, M. M., Saphonova, I. Y., Watanabe, T., Obut, O. T., Fujiwara, Y., Iwata, K., Semakov, N. N., Sugai, Y., Smirnova, L. V., and Kazansky, A. Y. (2001). Evolution of the Paleo-Asian Ocean (Altai-Sayan Region, Central Asia) and collision of possible Gondwana-derived terranes with the southern marginal part of the Siberian continent. *Geosciences Journal*, 5(3):203–224.

Cai, K., Sun, M., Yuan, C., Long, X., and Xiao, W. (2011). Geological framework and Paleozoic tectonic history of the Chinese Altai, NW China: a review. *Russian Geology and Geophysics*, 52(12):1619–1633.

Cai, K., Sun, M., Yuan, C., Xiao, W., Zhao, G., Long, X., and Wu, F. (2012). Carboniferous mantle-derived felsic intrusion in the Chinese Altai, NW China: Implications for geodynamic change of the accretionary orogenic belt. *Gondwana Research*, 22(2):681–698.

Calkins, J. A., Abers, G. A., Ekstrm, G., Creager, K. C., and Rondenay, S. (2011). Shallow structure of the Cascadia subduction zone beneath western Washington from spectral ambient noise correlation. *Journal of Geophysical Research: Solid Earth*, 116:1–20.

Campillo, M. and Paul, A. (2003). Long-range correlations in the diffuse seismic coda. *Science (New York, N.Y.)*, 299:547–549.

Cao, J., Wang, X., Sun, P., Zhang, Y., Tang, Y., Xiang, B., Lan, W., and Wu, M. (2012). Geochemistry and origins of natural gases in the central Junggar Basin, northwest China. *Organic Geochemistry*, 53:166–176.

Cao, M., Qin, K., Li, G., Jin, L., Evans, N. J., and Yang, X. (2014). Baogutu: An example of reduced porphyry Cu deposit in western Junggar. *Ore Geology Reviews*, 56:159–180.

Capon, J. (1970). Analysis of Rayleigh-wave multipath propagation at LASA*. *Bulletin of the Seismological Society of America*, 60(5):1701–1731.

Carroll, A. R., Yunhai, L., Graham, S. A., Xuchang, X., Hendrix, M. S., Jinchi, C., and McKnight, C. L. (1990). Junggar basin, northwest China: trapped Late Paleozoic ocean. *Tectonophysics*, 181(1-4):1–14.

Cawood, P. A. and Buchan, C. (2007). Linking accretionary orogenesis with supercontinent assembly. *Earth-Science Reviews*, 82(3):217–256.

Cawood, P. A., Kröner, A., Collins, W. J., Kusky, T. M., Mooney, W. D., and Windley, B. F. (2009). *Accretionary orogens through Earth history*. Geological Society of London.

Cawood, P. A., Leitch, E. C., Merle, R. E., and Nemchin, A. A. (2011). Orogenesis without collision: Stabilizing the Terra Australis accretionary orogen, eastern Australia. *GSA Bulletin*, 123(11-12):2240–2255.

Ceylan, S., Ni, J., Chen, J. Y., Zhang, Q., Tilmann, F., and Sandvol, E. (2012). Fragmented Indian plate and vertically coherent deformation beneath eastern Tibet. *Journal of Geophysical Research B: Solid Earth*, 117:1–11.

Charvet, J., Shu, L. S., and Laurent-Charvet, S. (2007). Paleozoic structural and geodynamic evolution of eastern Tianshan (NW China): welding of the Tarim and Junggar plates. *Episodes*, 30(3):162–186.

Chen, B. and Arakawa, Y. (2005). Elemental and Nd-Sr isotopic geochemistry of granitoids from the West Junggar foldbelt (NW China), with implications for Phanerozoic continental growth. *Geochimica et Cosmochimica Acta*, 69(5):1307–1320.

Chen, B. and Jahn, B.-m. (2004). Genesis of post-collisional granitoids and basement nature of the Junggar Terrane, NW China: Nd-Sr isotope and trace element evidence. *Journal of Asian Earth Sciences*, 23(5):691–703.

Chen, J. and King, S. D. (1998). The influence of temperature and depth dependent viscosity on geoid and topography profiles from models of mantle convection. *Physics of the earth and planetary interiors*, 106(1-2):75–92.

Chen, J.-F., Han, B.-F., Ji, J.-Q., Zhang, L., Xu, Z., He, G.-Q., and Wang, T. (2010). Zircon U–Pb ages and tectonic implications of Paleozoic plutons in northern West Junggar, North Xinjiang, China. *Lithos*, 115(1-4):137–152.

Chen, S., Pe-Piper, G., Piper, D. J., and Guo, Z. (2014). Ophiolitic mélanges in crustal-scale fault zones: Implications for the Late Palaeozoic tectonic evolution in West Junggar, China. *Tectonics*, 33(12):2419–2443.

Choulet, F., Faure, M., Cluzel, D., Chen, Y., Lin, W., and Wang, B. (2012). From oblique accretion to transpression in the evolution of the Altaid collage: new insights from West Junggar, northwestern China. *Gondwana Research*, 21(2-3):530–547.

Choulet, F., Faure, M., Cluzel, D., Chen, Y., Lin, W., Wang, B., and Xu, B. (2016). Toward a unified model of Altaids geodynamics: Insight from the Palaeozoic polycyclic evolution of West Junggar (NW China). *Science China Earth Sciences*, 59:25–57.

Coleman, R. G. (1989). Continental growth of northwest China. *Tectonics*, 8(3):621–635.

Condie, K. C. (2000). Episodic continental growth models: afterthoughts and extensions. *Tectonophysics*, 322(1):153–162.

Conrad, C. P. and Lithgow-Bertelloni, C. (2002). How Mantle Slabs Drive Plate Tectonics. *Science*, 298(5591):207–209.

Dagpunar, J. S. (2007). *Simulation and Monte Carlo: With applications in finance and MCMC*. John Wiley & Sons.

Dahlen, F., Hung, S.-H., and Nolet, G. (2000). Fréchet kernels for finite-frequency traveltimes-I. Theory. *Geophysical Journal International*, 141(1):157–174.

Dahlen, F. and Nolet, G. (2005). Comment on 'On sensitivity kernels for 'wave-equation' transmission tomography' by de Hoop and van der Hilst. *Geophysical Journal International*, 163(3):949–951.

Dahlen, F. and Tromp, J. (1998). *Theoretical global seismology*. Princeton university press.

De Hoop, M. V. and van Der Hilst, R. D. (2005). On sensitivity kernels for 'wave-equation' transmission tomography. *Geophysical Journal International*, 160(2):621–633.

Derode, A., Larose, E., Campillo, M., and Fink, M. (2003a). How to estimate the Green's function of a heterogeneous medium between two passive sensors? Application to acoustic waves. *Applied Physics Letters*, 83(15):3054–3056.

Derode, A., Larose, E., Tanter, M., De Rosny, J., Tourin, A., Campillo, M., and Fink, M. (2003b). Recovering the Green's function from field-field correlations in an open scattering medium (L). *The Journal of the Acoustical Society of America*, 113(6):2973–2976.

Du, J., Wong, M., and Zhu, H. (2007). Continuous and discrete inversion formulas for the Stockwell transform. *Integral Transforms and Special Functions*, 18(8):537–543.

Duijndam, A. (1988a). Bayesian estimation in seismic inversion. Part I: Principles. *Geophysical Prospecting*, 36(8):878–898.

Duijndam, A. (1988b). Bayesian estimation in seismic inversion. Part II: Uncertainty analysis. *Geophysical Prospecting*, 36(8):899–918.

Dumitru, T. A., Zhou, D., Chang, E. Z., Graham, S. A., Hendrix, M. S., Sobel, E. R., and Carroll, A. R. (2001). Uplift, exhumation, and deformation in the Chinese Tian Shan. *MEMOIRS-GEOLOGICAL SOCIETY OF AMERICA*, pages 71–100.

Dziewonski, A. M., Hager, B. H., and O'Connell, R. J. (1977). Large-scale heterogeneities in the lower mantle. *Journal of Geophysical Research*, 82(2):239–255.

Eizenhöfer, P. R., Zhao, G., Zhang, J., and Sun, M. (2014). Final closure of the Paleo-Asian Ocean along the Solonker Suture Zone: Constraints from geochronological and geochemical data of Permian volcanic and sedimentary rocks. *Tectonics*, 33(4):441–463.

Ekström, G. (2011). A global model of love and rayleigh surface wave dispersion and anisotropy, 25-250 s. *Geophysical Journal International*, 187(3):1668–1686.

Eraker, B. (2001). MCMC analysis of diffusion models with application to finance. *Journal of Business & Economic Statistics*, 19(2):177–191.

Feng, Y., Coleman, R. G., Tilton, G., and Xiao, X. (1989). Tectonic evolution of the west Junggar region, Xinjiang, China. *Tectonics*, 8(4):729–752.

Forsyth, D. W. and Li, A. (2005). Array analysis of two-dimensional variations in surface wave phase velocity and azimuthal anisotropy in the presence of multipathing interference. *Seismic Earth: Array Analysis of Broadband Seismograms*, pages 81–97.

Fu, Y. V., Gao, Y., Li, A., and Shi, Y. (2015). Lithospheric shear wave velocity and radial anisotropy beneath the northern part of North China from surface wave dispersion analysis. *Geochemistry, Geophysics, Geosystems*, 16(8):2619–2636.

Fukao, Y., Obayashi, M., Inoue, H., and Nenbai, M. (1992). Subducting slabs stagnant in the mantle transition zone. *Journal of Geophysical Research: Solid Earth*, 97(B4):4809–4822.

Fukao, Y., Obayashi, M., Nakakuki, T., and Group, D. S. P. (2009). Stagnant slab: a review. *Annual Review of Earth and Planetary Sciences*, 37:19–46.

Fukao, Y., Widiyantoro, S., and Obayashi, M. (2001). Stagnant slabs in the upper and lower mantle transition region. *Reviews of Geophysics*, 39(3):291–323.

Gao, J., Li, M., Xiao, X., Tang, Y., and He, G. (1998). Paleozoic tectonic evolution of the Tianshan Orogen, northwestern China. *Tectonophysics*, 287:213–231.

Gao, R., Hou, H. S., Cai, X. Y., Knapp, J. H., He, R. Z., Liu, J. K., Xiong, X. S., Guan, Y., Li, W. H., Zeng, L. S., and Roecker, S. W. (2013). Fine crustal structure beneath the junction of the southwest Tian Shan and Tarim Basin, NW China. *Lithosphere*, 5(4):382–392.

Gao, R., Xiao, L., Pirajno, F., Wang, G.-c., He, X.-x., Yang, G., and Yan, S.-w. (2014). Carboniferous–Permian extensive magmatism in the West Junggar, Xinjiang, northwestern China: its geochemistry, geochronology, and petrogenesis. *Lithos*, 204:125–143.

Gardner, G., Gardner, L., and Gregory, A. (1974). Formation velocity and density-The diagnostic basics for stratigraphic traps. *Geophysics*, 39(6):770–780.

Gelman, A., Roberts, G. O., Gilks, W. R., et al. (1996). Efficient Metropolis jumping rules. *Bayesian statistics*, 5(599-608):42.

Geng, H., Sun, M., Yuan, C., Xiao, W., Xian, W., Zhao, G., Zhang, L., Wong, K., and Wu, F. (2009). Geochemical, Sr–Nd and zircon U–Pb–Hf isotopic studies of Late Carboniferous magmatism in the West Junggar, Xinjiang: implications for ridge subduction? *Chemical Geology*, 266(3-4):364–389.

Gilks, W. R., Richardson, S., and Spiegelhalter, D. J. (1996). Introducing markov chain monte carlo. *Markov chain Monte Carlo in practice*, 1:19.

Gilks, W. R., Roberts, G. O., and Sahu, S. K. (1998). Adaptive markov chain monte carlo through regeneration. *Journal of the American statistical association*, 93(443):1045–1054.

Glen, R. (2013). Refining accretionary orogen models for the Tasmanides of eastern Australia. *Australian Journal of Earth Sciences*, 60(3):315–370.

Glen, R., Percival, I., and Quinn, C. (2009). Ordovician continental margin terranes in the Lachlan Orogen, Australia: implications for tectonics in an accretionary orogen along the east Gondwana margin. *Tectonics*, 28(6).

Glorie, S., De Grave, J., Buslov, M. M., Elburg, M. A., Stockli, D. F., Gerdes, A., and Van den haute, P. (2010). Multi-method chronometric constraints on the evolution of the Northern Kyrgyz Tien Shan granitoids (Central Asian Orogenic Belt): From emplacement to exhumation. *Journal of Asian Earth Sciences*, 38(3):131–146.

Golightly, A. and Wilkinson, D. J. (2005). Bayesian inference for stochastic kinetic models using a diffusion approximation. *Biometrics*, 61(3):781–788.

Golightly, A. and Wilkinson, D. J. (2006). Bayesian sequential inference for stochastic kinetic biochemical network models. *Journal of Computational Biology*, 13(3):838–851.

Gorbatov, A., Widiyantoro, S., Fukao, Y., and Gordeev, E. (2000). Signature of remnant slabs in the North Pacific from P-wave tomography. *Geophysical Journal International*, 142(1):27–36. 10.1046/j.1365-246x.2000.00122.x.

Green, P. J. and Mira, A. (2001). Delayed rejection in reversible jump Metropolis–Hastings. *Biometrika*, 88(4):1035–1053.

Greyserman, A., Jones, D. H., and Strawderman, W. E. (2006). Portfolio selection using hierarchical Bayesian analysis and MCMC methods. *Journal of Banking & Finance*, 30(2):669–678.

Groos, J. C., Bussat, S., and Ritter, J. R. R. (2012). Performance of different processing schemes in seismic noise cross-correlations. *Geophysical Journal International*, 188:498–512.

Gu, P., Li, Y., Zhang, B., Tong, L., and Wang, J. (2009). LA-ICP-MS zircon U-Pb dating of gabbro in the Darbut ophiolite, western Junggar, China. *Acta Petrologica Sinica*, 25(6):1364–1372.

Guo, Z., Afonso, J. C., Qashqai, M. T., Yang, Y., and Chen, Y. J. (2016a). Thermochemical structure of the North China Craton from multi-observable probabilistic inversion: Extent and causes of cratonic lithosphere modification. *Gondwana Research*, 37:252–265.

Guo, Z., Chen, Y. J., Ning, J., Yang, Y., Afonso, J. C., and Tang, Y. (2016b). Seismic evidence of on-going sublithosphere upper mantle convection for intra-plate volcanism in Northeast China. *Earth and Planetary Science Letters*, 433:31–43.

Guo, Z., Wang, K., Yang, Y., Tang, Y., John Chen, Y., and Hung, S.-H. (2018). The Origin and Mantle Dynamics of Quaternary Intraplate Volcanism in Northeast China From Joint Inversion of Surface Wave and Body Wave. *Journal of Geophysical Research: Solid Earth*, 123(3):2410–2425.

Gurnis, M. and Hager, B. H. (1988). Controls of the structure of subducted slabs. *Nature*, 335(6188):317.

Haario, H., Laine, M., Mira, A., and Saksman, E. (2006). DRAM: efficient adaptive MCMC. *Statistics and computing*, 16(4):339–354.

Haario, H., Saksman, E., and Tamminen, J. (1999). Adaptive proposal distribution for random walk Metropolis algorithm. *Computational Statistics*, 14(3):375–396.

Haario, H., Saksman, E., Tamminen, J., et al. (2001). An adaptive Metropolis algorithm. *Bernoulli*, 7(2):223–242.

Hacker, B. R., Abers, G. A., and Peacock, S. M. (2003). Subduction factory 1. Theoretical mineralogy, densities, seismic wave speeds, and H2O contents. *Journal of Geophysical Research: Solid Earth*, 108(B1).

Hall, R. (2009). The Eurasian SE Asian margin as a modern example of an accretionary orogen. *Geological Society, London, Special Publications*, 318(1):351.

Han, B., Ji, J., Song, B., Chen, L., and Zhang, L. (2006). Late Paleozoic vertical growth of continental crust around the Junggar Basin, Xinjiang, China (Part I): timing of post-collisional plutonism. *Acta Petrologica Sinica*, 22(5):1077–1086.

Han, B.-f., Wang, S.-g., Jahn, B.-m., Hong, D.-w., Kagami, H., and Sun, Y.-l. (1997). Depleted-mantle source for the Ulungur River A-type granites from North Xinjiang, China: geochemistry and Nd-Sr isotopic evidence, and implications for Phanerozoic crustal growth. *Chemical Geology*, 138(3):135–159.

Han, Y. and Zhao, G. (2017). Final amalgamation of the Tianshan and Junggar orogenic collage in the southwestern Central Asian Orogenic Belt: Constraints on the closure of the Paleo-Asian Ocean. *Earth-Science Reviews*.

Haskell, N. (1964). Radiation pattern of surface waves from point sources in a multi-layered medium. *Bulletin of the Seismological Society of America*, 54(1):377–393.

Hastings, W. K. (1970). Monte Carlo sampling methods using Markov chains and their applications. *Biometrika*, 57(1):97–109.

He, D.-F., Li, D., Fan, C., and Yang, X.-F. (2013). Geochronology, geochemistry and tectonostratigraphy of Carboniferous strata of the deepest Well Moshen-1 in the Junggar Basin, northwest China: Insights into the continental growth of Central Asia. *Gondwana Research*, 24(2):560–577.

He, G., Liu, J., Zhang, Y., and Xu, X. (2007). Keramay ophiolitic mélange formed during early Paleozoic in western Junggar basin. *Acta Petrologica Sinica*, 23(7):1573–1576.

Hetényi, G. and Bus, Z. (2007). Shear wave velocity and crustal thickness in the Pannonian Basin from receiver function inversions at four permanent stations in Hungary. *Journal of Seismology*, 11(4):405–414.

Hung, S.-H., Chen, W.-P., and Chiao, L.-Y. (2011). A data-adaptive, multiscale approach of finite-frequency, traveltime tomography with special reference to P and S wave data from central Tibet. *Journal of Geophysical Research: Solid Earth*, 116(B6).

Hung, S.-H., Chen, W.-P., Chiao, L.-Y., and Tseng, T.-L. (2010). First multi-scale, finite-frequency tomography illuminates 3-D anatomy of the Tibetan plateau. *Geophysical Research Letters*, 37(6).

Hung, S. H., Dahlen, F. A., and Nolet, G. (2002). Fréchet kernels for finite-frequency traveltimes-II. Examples. *Geophysical Journal International*, 141(1):175–203.

Hung, S.-H., Shen, Y., and Chiao, L.-Y. (2004). Imaging seismic velocity structure beneath the Iceland hot spot: A finite frequency approach. *Journal of Geophysical Research: Solid Earth*, 109(B8).

Husen, S. and Kissling, E. (2001). Local earthquake tomography between rays and waves: fat ray tomography. *Physics of the earth and Planetary Interiors*, 125(1-4):171–191.

Isozaki, Y. (1996). Anatomy and genesis of a subduction-related orogen: A new view of geotectonic subdivision and evolution of the Japanese Islands. *Island Arc*, 5(3):289–320.

Isozaki, Y., Aoki, K., Nakama, T., and Yanai, S. (2010). New insight into a subduction-related orogen: A reappraisal of the geotectonic framework and evolution of the Japanese Islands. *Gondwana Research*, 18(1):82–105.

Jahn, B.-m. (2000). Massive granitoid generation in Central Asia: Nd isotope evidence and implication for continental growth in the Phanerozoic. *Episodes*, 23:82–92.

Jahn, B.-M. (2010). Accretionary orogen and evolution of the Japanese Islands: Implications from a Sr-Nd isotopic study of the Phanerozoic granitoids from SW Japan. *American Journal of Science*, 310(10):1210–1249.

Jiang, C., Schmandt, B., Hansen, S. M., Dougherty, S. L., Clayton, R. W., Farrell, J., and Lin, F.-C. (2018). Rayleigh and S wave tomography constraints on subduction termination and lithospheric foundering in central California. *Earth and Planetary Science Letters*, 488:14–26.

Jiang, C., Yang, Y., and Zheng, Y. (2014). Penetration of mid-crustal low velocity zone across the Kunlun Fault in the NE Tibetan Plateau revealed by ambient noise tomography. *Earth and Planetary Science Letters*, 406:81–92.

Jiang, X. D., Li, Z. X., and Li, H. B. (2013). Uplift of the West Kunlun Range, northern Tibetan Plateau, dominated by brittle thickening of the upper crust. *Geology*, 41(4):439–442.

Jiang, Y., Sun, M., Zhao, G., Yuan, C., Xiao, W., Xia, X., Long, X., and Wu, F. (2010). The ~390 Ma high-T metamorphic event in the Chinese Altai: A consequence of ridge-subduction? *American Journal of Science*, 310(10):1421–1452.

Jolivet, M., Dominguez, S., Charreau, J., Chen, Y., Li, Y., and Wang, Q. (2010). Mesozoic and Cenozoic tectonic history of the central Chinese Tian Shan: Reactivated tectonic structures and active deformation. *Tectonics*, 29(6).

Jones, A. G. (1993). Electromagnetic images of modern and ancient subduction zones. *Tectonophysics*, 219(1-3):29–45.

Jones, A. G., Afonso, J. C., and Fullea, J. (2017). Geochemical and geophysical constrains on the dynamic topography of the Southern African Plateau. *Geochemistry Geophysics Geosystems*, 18(10):3556–3575. Fm8vc Times Cited:2 Cited References Count:65.

Kemp, A., Hawkesworth, C., Collins, W., Gray, C., Blevin, P., et al. (2009). Isotopic evidence for rapid continental growth in an extensional accretionary orogen: The Tasmanides, eastern Australia. *Earth and Planetary Science Letters*, 284(3-4):455–466.

Kennett, B., Sambridge, M., and Williamson, P. (1988). Subspace methods for large inverse problems with multiple parameter classes. *Geophysical Journal International*, 94(2):237–247.

Kennett, B. L. N., Engdahl, E. R., and Buland, R. (1995). Constraints on seismic velocities in the Earth from traveltimes. *Geophysical Journal International*, 122(1):108–124.

Khain, E. V., Bibikova, E. V., Kröner, A., Zhuravlev, D. Z., Sklyarov, E. V., Fedotova, A. A., and Kravchenko-Berezhnoy, I. R. (2002). The most ancient ophiolite of the Central Asian fold belt: U-Pb and Pb-Pb zircon ages for the Dunzhugur Complex, Eastern Sayan, Siberia, and geodynamic implications. *Earth and Planetary Science Letters*, 199(3):311–325.

Khan, A., Boschi, L., and Connolly, J. (2009). On mantle chemical and thermal heterogeneities and anisotropy as mapped by inversion of global surface wave data. *Journal of Geophysical Research: Solid Earth*, 114(B9).

Kikuchi, M. and Kanamori, H. (1982). Inversion of complex body waves. *Bulletin of the Seismological Society of America*, 72(2):491–506.

King, S. D., Frost, D. J., and Rubie, D. C. (2015). Why cold slabs stagnate in the transition zone. *Geology*, 43(3):231–234. 10.1130/G36320.1.

Kinoshita, O. (2002). Possible manifestations of slab window magmatisms in Cretaceous southwest Japan. *Tectonophysics*, 344(1):1–13.

Kolstrup, M. L., Hung, S.-H., and Maupin, V. (2015). Multiscale, finite-frequency P and S tomography of the upper mantle in the southwestern Fennoscandian Shield. *Geophysical Journal International*, 202(1):190–218.

Korn, R., Korn, E., and Kroisandt, G. (2010). *Monte Carlo methods and models in finance and insurance*. CRC press.

Kröner, A., Hegner, E., Lehmann, B., Heinhorst, J., Wingate, M., Liu, D., and Ermelov, P. (2008). Palaeozoic arc magmatism in the Central Asian Orogenic Belt of Kazakhstan: SHRIMP zircon ages and whole-rock Nd isotopic systematics. *Journal of Asian Earth Sciences*, 32(2-4):118–130.

Kröner, A., Windley, B., Badarch, G., Tomurtogoo, O., Hegner, E., Jahn, B., Gruschka, S., Khain, E., Demoux, A., and Wingate, M. (2007). Accretionary growth and crust formation in the Central Asian Orogenic Belt and comparison with the Arabian-Nubian shield. *Memoirs-Geological Society of America*, 200:181.

Lanz, E., Maurer, H., and Green, A. (1998). Refraction tomography over a buried waste disposal site. *GEOPHYSICS*, 63(4):1414–1433.

Laske, G. (1995). Global observation of off-great-circle propagation of Long-Period surface waves. *Geophysical Journal International*, 123(1):245–259.

Laske, G., Masters, G., Ma, Z., and Pasyanos, M. (2013). Update on CRUST1.0 - A 1-degree global model of Earth's crust. In *Geophys. Res. Abstr.*, volume 15, page 2658.

Lee, S. v. d. and Nolet, G. (1997). Upper mantle S velocity structure of North America. *Journal of Geophysical Research: Solid Earth*, 102(B10):22815–22838.

Levander, A., Schmandt, B., Miller, M., Liu, K., Karlstrom, K., Crow, R., Lee, C.-T., and Humphreys, E. (2011). Continuing Colorado plateau uplift by delamination-style convective lithospheric downwelling. *Nature*, 472(7344):461.

Levshin, A. and Ritzwoller, M. (2001). Automated detection, extraction, and measurement of regional surface waves. In *Monitoring the Comprehensive Nuclear-Test-Ban Treaty: Surface Waves*, pages 1531–1545. Springer.

Li, A. and Burke, K. (2006). Upper mantle structure of southern Africa from Rayleigh wave tomography. *Journal of Geophysical Research: Solid Earth*, 111(B10).

Li, D. and Castagna, J. (2013). Modified S-transform in time-frequency analysis of seismic data. In *SEG Technical Program Expanded Abstracts 2013*, pages 4629–4634. Society of Exploration Geophysicists.

Li, D., He, D., and Fan, C. (2015). Geochronology and Sr–Nd–Hf isotopic composition of the granites, enclaves, and dikes in the Karamay area, NW China: Insights into late Carboniferous crustal growth of West Junggar. *Geoscience Frontiers*, 6(2):153–173.

Li, D., He, D., and Tang, Y. (2016). Reconstructing multiple arc-basin systems in the Altai-Junggar area (NW China): Implications for the architecture and evolution of the western Central Asian Orogenic Belt. *Journal of Asian Earth Sciences*, 121:84–107.

Li, G., Niu, F., Yang, Y., and Xie, J. (2018). An investigation of time-frequency domain phase-weighted stacking and its application to phase-velocity extraction from ambient noise's empirical Green's functions. *Geophysical Journal International*, 212(2):1143–1156.

Li, H., Su, W., Wang, C.-Y., and Huang, Z. (2009). Ambient noise Rayleigh wave tomography in western Sichuan and eastern Tibet. *Earth and Planetary Science Letters*, 282(1-4):201–211.

Li, J., He, G., Xu, X., Li, H., Sun, G., Yang, T., Gao, L., and Zhu, Z. (2006). Crustal tectonic framework of northern Xinjiang and adjacent regions and its formation. *Acta Geologica Sinica*, 80(1):148–168.

Li, J., Wang, X., Wang, X., and Yuen, D. A. (2013). P and SH velocity structure in the upper mantle beneath Northeast China: Evidence for a stagnant slab in hydrous mantle transition zone. *Earth and Planetary Science Letters*, 367:71–81.

Li, Y., Gao, M., and Wu, Q. (2014). Crustal thickness map of the Chinese mainland from teleseismic receiver functions. *Tectonophysics*, 611:51–60.

Ligorria, J. P. and Ammon, C. J. (1999). Iterative deconvolution and receiver-function estimation. *Bulletin of the seismological Society of America*, 89(5):1395–1400.

Lin, F. C., Moschetti, M. P., and Ritzwoller, M. H. (2008). Surface wave tomography of the western United States from ambient seismic noise: Rayleigh and Love wave phase velocity maps. *Geophysical Journal International*, 173:281–298.

Liu, B., Han, B.-F., Xu, Z., Ren, R., Zhang, J.-R., Zhou, J., Su, L., and Li, Q.-L. (2016). The Cambrian initiation of intra-oceanic subduction in the southern Paleo-Asian Ocean: Further evidence from the Barleik subduction-related metamorphic complex in the West Junggar region, NW China. *Journal of Asian Earth Sciences*, 123:1–21.

Liu, Q. and Gu, Y. J. (2012). Seismic imaging: From classical to adjoint tomography. *Tectonophysics*, 566-567:31–66.

Lobkis, O. I. and Weaver, R. L. (2001). On the emergence of the Green's function in the correlations of a diffuse field. *The Journal of the Acoustical Society of America*, 110(6):3011–3017.

Lou, X., van der Lee, S., and Lloyd, S. (2013). AIMBAT: A Python/Matplotlib Tool for Measuring Teleseismic Arrival Times. *Seismological Research Letters*, 84(1):85–93.

Luo, Y., Yang, Y., Xu, Y., Xu, H., Zhao, K., and Wang, K. (2015). On the limitations of interstation distances in ambient noise tomography. *Geophysical Journal International*, 201(2):652–661.

Ma, C., Xiao, W., Windley, B. F., Zhao, G., Han, C., Zhang, J., Luo, J., and Li, C. (2012). Tracing a subducted ridge–transform system in a late Carboniferous accretionary prism of the southern Altaids: orthogonal sanukitoid dyke swarms in Western Junggar, NW China. *Lithos*, 140:152–165.

Ma, D., He, D., Li, D., Tang, J., and Liu, Z. (2015). Kinematics of syn-tectonic unconformities and implications for the tectonic evolution of the Hala'alat Mountains at the northwestern margin of the Junggar Basin, Central Asian Orogenic Belt. *Geoscience Frontiers*, 6(2):247–264.

Malve, O., Laine, M., and Haario, H. (2005). Estimation of winter respiration rates and prediction of oxygen regime in a lake using Bayesian inference. *Ecological Modelling*, 182(2):183–197.

Malve, O., Laine, M., Haario, H., Kirkkala, T., and Sarvala, J. (2007). Bayesian modelling of algal mass occurrences - using adaptive MCMC methods with a lake water quality model. *Environmental Modelling & Software*, 22(7):966–977.

Marquardt, H. and Miyagi, L. (2015). Slab stagnation in the shallow lower mantle linked to an increase in mantle viscosity. *Nature Geoscience*, 8:311.

Marquering, H., Dahlen, F., and Nolet, G. (1999). Three-dimensional sensitivity kernels for finite-frequency traveltimes: the banana-doughnut paradox. *Geophysical Journal International*, 137(3):805–815.

Masters, G., Barmine, M., and Kientz, S. (2007). Mineos user's manual. *Computational Infrastructure for Geodynamics*.

McFADDEN, P. D., Cook, J., and Forster, L. (1999). Decomposition of gear vibration signals by the generalised S transform. *Mechanical systems and signal processing*, 13(5):691–707.

Metropolis, N., Rosenbluth, A. W., Rosenbluth, M. N., Teller, A. H., and Teller, E. (1953). Equation of state calculations by fast computing machines. *The journal of chemical physics*, 21(6):1087–1092.

Mira, A. et al. (2001). On Metropolis-Hastings algorithms with delayed rejection. *Metron*, 59(3-4):231–241.

Molnar, S., Dosso, S. E., and Cassidy, J. F. (2010). Bayesian inversion of microtremor array dispersion data in southwestern British Columbia. *Geophysical Journal International*, 183(2):923–940.

Montelli, R., Nolet, G., Dahlen, F., Masters, G., Engdahl, E. R., and Hung, S.-H. (2004). Finite-frequency tomography reveals a variety of plumes in the mantle. *Science*, 303(5656):338–343.

Mooney, W. (2010). 11 Crust and Lithospheric Structure–Global Crustal Structure. *Seismology and Structure of the Earth: Treatise on Geophysics*, 1:361.

Moschetti, M., Ritzwoller, M., Lin, F., and Yang, Y. (2010). Seismic evidence for widespread western-US deep-crustal deformation caused by extension. *Nature*, 464(7290):885.

Moschetti, M., Ritzwoller, M., and Shapiro, N. (2007). Surface wave tomography of the western United States from ambient seismic noise: Rayleigh wave group velocity maps. *Geochemistry, Geophysics, Geosystems*, 8(8).

Mosegaard, K. and Tarantola, A. (1995). Monte Carlo sampling of solutions to inverse problems. *Journal of Geophysical Research: Solid Earth*, 100(B7):12431–12447.

Nakanishi, I. and Anderson, D. L. (1982). Worldwide distribution of group velocity of mantle Rayleigh waves as determined by spherical harmonic inversion. *Bulletin of the Seismological Society of America*, 72(4):1185–1194.

Nakanishi, I. and Anderson, D. L. (1983). Measurement of mantle wave velocities and inversion for lateral heterogeneity and anisotropy: 1. Analysis of Great Circle Phase Velocities. *Journal of Geophysical Research: Solid Earth*, 88(B12):10267–10283.

Nataf, H. C., Nakanishi, I., and Anderson, D. L. (1984). Anisotropy and shear-velocity heterogeneities in the upper mantle. *Geophysical Research Letters*, 11(2):109–112.

Nataf, H.-C., Nakanishi, I., and Anderson, D. L. (1986). Measurements of mantle wave velocities and inversion for lateral heterogeneities and anisotropy: 3. Inversion. *Journal of Geophysical Research: Solid Earth*, 91(B7):7261–7307.

Nylander, J. A., Wilgenbusch, J. C., Warren, D. L., and Swofford, D. L. (2007). AWTY (are we there yet?): a system for graphical exploration of MCMC convergence in Bayesian phylogenetics. *Bioinformatics*, 24(4):581–583.

Obrebski, M., Allen, R. M., Pollitz, F., and Hung, S.-H. (2011). Lithosphere-asthenosphere interaction beneath the western united states from the joint inversion of body-wave traveltimes and surface-wave phase velocities. *Geophysical Journal International*, 185(2):1003–1021.

Obrebski, M., Allen, R. M., Xue, M., and Hung, S.-H. (2010). Slab-plume interaction beneath the Pacific Northwest. *Geophysical Research Letters*, 37(14).

O'Reilly, S. Y. and Griffin, W. (2013). Moho vs crust–mantle boundary: evolution of an idea. *Tectonophysics*, 609:535–546.

Osborne, M. R. (1969). On shooting methods for boundary value problems. *Journal of mathematical analysis and applications*, 27(2):417–433.

Ouyang, L., Li, H., Lü, Q., Yang, Y., Li, X., Jiang, G., Zhang, G., Shi, D., Zheng, D., Sun, S., Tan, J., and Zhou, M. (2014). Crustal and uppermost mantle velocity structure and its relationship with the formation of ore districts in the Middle-Lower Yangtze River region. *Earth and Planetary Science Letters*, 408:378–389.

Paige, C. C. and Saunders, M. A. (1982). LSQR: An Algorithm for Sparse Linear Equations and Sparse Least Squares. *ACM Trans. Math. Softw.*, 8(1):43–71.

Palomeras, I., Thurner, S., Levander, A., Liu, K., Villaseñor, A., Carbonell, R., and Harnafi, M. (2014). Finite-frequency Rayleigh wave tomography of the western Mediterranean: Mapping its lithospheric structure. *Geochemistry, Geophysics, Geosystems*, 15(1):140–160.

Porritt, R. W., Allen, R. M., Boyarko, D. C., and Brudzinski, M. R. (2011). Investigation of Cascadia segmentation with ambient noise tomography. *Earth and Planetary Science Letters*, 309(1):67–76.

Press, W. H., Teukolsky, S. A., Vetterling, W. T., and Flannery, B. P. (2007). *Numerical recipes 3rd edition: The art of scientific computing*. Cambridge university press.

Rao, S., Hu, S.-B., Zhu, C.-Q., Tang, X.-Y., Li, W.-W., and Wang, J.-Y. (2013). Characteristics of Heat Flow and Lithospheric Thermal Structure in the Junggar Basin, Northwestern China. *Chinese Journal of Geophysics*, 56(5):661–673.

Rawlinson, N., Pozgay, S., and Fishwick, S. (2010). Seismic tomography: A window into deep Earth. *Physics of the Earth and Planetary Interiors*, 178:101–135.

Rawlinson, N. and Sambridge, M. (2005). The fast marching method: an effective tool for tomographic imaging and tracking multiple phases in complex layered media. *Exploration Geophysics*, 36(4):341–350.

Rawlinson, N., Sambridge, M., et al. (2003). Seismic traveltime tomography of the crust and lithosphere. *Advances in Geophysics*, 46:81–199.

Roberts, G. O., Gelman, A., Gilks, W. R., et al. (1997). Weak convergence and optimal scaling of random walk Metropolis algorithms. *The annals of applied probability*, 7(1):110–120.

Roux, P., Sabra, K. G., Kuperman, W. A., and Roux, A. (2005). Ambient noise cross correlation in free space: Theoretical approach. *The Journal of the Acoustical Society of America*, 117(1):79–84.

Rudnick, R. L. (1995). Making continental crust. *Nature*, 378:571.

Rudnick, R. L. and Gao, S. (2003). Composition of the continental crust. *Treatise on geochemistry*, 3:659.

Sabra, K. G., Gerstoft, P., Roux, P., Kuperman, W., and Fehler, M. C. (2005a). Extracting time-domain Green's function estimates from ambient seismic noise. *Geophysical Research Letters*, 32(3).

Sabra, K. G., Gerstoft, P., Roux, P., Kuperman, W., and Fehler, M. C. (2005b). Surface wave tomography from microseisms in Southern California. *Geophysical Research Letters*, 32(14).

Saleeby, J. B. (1983). Accretionary tectonics of the North American cordillera. *Annual Review of Earth and Planetary Sciences*, 11(1):45–73.

Sambridge, M. (1999a). Geophysical inversion with a neighbourhood algorithm - I. Searching a parameter space. *Geophysical Journal International*, 138(2):479–494.

Sambridge, M. (1999b). Geophysical inversion with a neighbourhood algorithm - II. Appraising the ensemble. *Geophysical Journal International*, 138(3):727–746.

Saygin, E. and Kennett, B. L. N. (2010). Ambient seismic noise tomography of Australian continent. *Tectonophysics*, 481:116–125.

Schimmel, M. and Gallart, J. (2005). The inverse S-transform in filters with time-frequency localization. *IEEE Transactions on signal processing*, 53(11):4417–4422.

Schimmel, M. and Gallart, J. (2007). Frequency-dependent phase coherence for noise suppression in seismic array data. *Journal of Geophysical Research: Solid Earth*, 112(B4).

Schimmel, M. and Paulssen, H. (1997). Noise reduction and detection of weak, coherent signals through phase-weighted stacks. *Geophysical Journal International*, 130(2):497–505.

Schimmel, M., Stutzmann, E., and Gallart, J. (2011). Using instantaneous phase coherence for signal extraction from ambient noise data at a local to a global scale. *Geophysical Journal International*, 184(1):494–506.

Şengör, A. M. C. and Natal'In, B. A. (1996). Turkic-type orogeny and its role in the making of the continental crust. *Annual Review of Earth and Planetary Sciences*, 24(1):263–337.

Şengör, A. M. C., Natal'In, B. A., and Burtman, V. (1993). Evolution of the Altaid tectonic collage and Palaeozoic crustal growth in Eurasia. *Nature*, 364(6435):299.

Şengör, A. M. C., Natal'in, B. A., Sunal, G., and van der Voo, R. (2013). The Tectonics of the Altaids: Crustal Growth During the Construction of the Continental Lithosphere of Central Asia Between ~750 and ~130 Ma Ago. *Annual Review of Earth and Planetary Sciences*, 46(1):439–494.

Shan, B., Afonso, J. C., Yang, Y., Grose, C. J., Zheng, Y., Xiong, X., and Zhou, L. (2014). The thermochemical structure of the lithosphere and upper mantle beneath south China: Results from multiobservable probabilistic inversion. *Journal of Geophysical Research: Solid Earth*, 119(11):8417–8441.

Shan, B., Xiong, X., Zhao, K. F., Xie, Z. J., Zheng, Y., and Zhou, L. (2017). Crustal and upper-mantle structure of South China from Rayleigh wave tomography. *Geophysical Journal International*, 208(3):1643–1654.

Shapiro, N. and Ritzwoller, M. (2002). Monte-Carlo inversion for a global shear-velocity model of the crust and upper mantle. *Geophysical Journal International*, 151(1):88–105.

Shen, P., Pan, H., Shen, Y., Yan, Y., and Zhong, S. (2015). Main deposit styles and associated tectonics of the West Junggar region, NW China. *Geoscience Frontiers*, 6(2):175–190.

Shen, P., Shen, Y., Liu, T., Meng, L., Dai, H., and Yang, Y. (2009). Geochemical signature of porphyries in the Baogutu porphyry copper belt, western Junggar, NW China. *Gondwana Research*, 16(2):227–242.

Shen, W., Ritzwoller, M. H., Schulte-Pelkum, V., and Lin, F. C. (2013). Joint inversion of surface wave dispersion and receiver functions: A Bayesian monte-Carlo approach. *Geophysical Journal International*, 192:807–836.

Smith, M. L. and Dahlen, F. (1973). The azimuthal dependence of Love and Rayleigh wave propagation in a slightly anisotropic medium. *Journal of Geophysical Research*, 78(17):3321–3333.

Smithies, R. H., Van Kranendonk, M. J., and Champion, D. C. (2007). The Mesoarchean emergence of modern-style subduction. *Gondwana Research*, 11(1):50–68.

Snieder, R. (2004). Extracting the Green's function from the correlation of coda waves: A derivation based on stationary phase. *Physical Review E*, 69(4):046610.

Snieder, R. (2006). The theory of coda wave interferometry. *Pure and Applied geophysics*, 163(2-3):455–473.

Snieder, R. and Nolet, G. (1987). Linearized scattering of surface-waves on a spherical Earth. *JOURNAL OF GEOPHYSICS-ZEITSCHRIFT FUR GEOPHYSIK*, 61(1):55–63.

Socco, L. V. and Boiero, D. (2008). Improved Monte Carlo inversion of surface wave data. *Geophysical Prospecting*, 56(3):357–371.

Sol, S., Thomson, C. J., Kendall, J. M., White, D., VanDecar, J. C., and Asudeh, I. (2002). Seismic tomographic images of the cratonic upper mantle beneath the Western Superior Province of the Canadian Shield-a remnant Archean slab? *Physics of the Earth and Planetary Interiors*, 134(1):53–69.

Stern, R. J. (2005). Evidence from ophiolites, blueschists, and ultrahigh-pressure metamorphic terranes that the modern episode of subduction tectonics began in Neoproterozoic time. *Geology*, 33(7):557–560.

Stockwell, R. G., Mansinha, L., and Lowe, R. (1996). Localization of the complex spectrum: the S transform. *IEEE transactions on signal processing*, 44(4):998–1001.

Su, Y., Tang, H., Hou, G., and Liu, C. (2006). Geochemistry of aluminous A-type granites along Darabut tectonic belt in West Junggar, Xinjiang. *Geochimica*, 35(1):55–67.

Sun, M., Yuan, C., Xiao, W., Long, X., Xia, X., Zhao, G., Lin, S., Wu, F., and Kröner, A. (2008). Zircon U-Pb and Hf isotopic study of gneissic rocks from the Chinese Altai: Progressive accretionary history in the early to middle Palaeozoic. *Chemical Geology*, 247(3):352–383.

Tang, G., Wang, Q., Wyman, D. A., Li, Z.-X., Zhao, Z.-H., Jia, X.-H., and Jiang, Z.-Q. (2010). Ridge subduction and crustal growth in the Central Asian Orogenic Belt: evidence from Late Carboniferous adakites and high-Mg diorites in the western Junggar region, northern Xinjiang (west China). *Chemical Geology*, 277(3):281–300.

Tang, G.-J., Wang, Q., Wyman, D. A., Li, Z.-X., Xu, Y.-G., and Zhao, Z.-H. (2012a). Recycling oceanic crust for continental crustal growth: Sr-Nd-Hf isotope evidence from granitoids in the western Junggar region, NW China. *Lithos*, 128-131:73–83.

Tang, G.-J., Wang, Q., Wyman, D. A., Li, Z.-X., Zhao, Z.-H., and Yang, Y.-H. (2012b). Late Carboniferous high ϵNd(t)-ϵHf(t) granitoids, enclaves and dikes in western Junggar, NW China: Ridge-subduction-related magmatism and crustal growth. *Lithos*, 140-141:86–102.

Tanimoto, T. and Anderson, D. L. (1984). Mapping convection in the mantle. *Geophysical Research Letters*, 11(4):287–290.

Tarantola, A. and Valette, B. (1982). Generalized nonlinear inverse problems solved using the least squares criterion. *Reviews of Geophysics*, 20(2):219–232.

Thorkelson, D. J. (1996). Subduction of diverging plates and the principles of slab window formation. *Tectonophysics*, 255(1):47–63.

Thurber, C. H. (1983). Earthquake locations and three-dimensional crustal structure in the Coyote Lake area, central California. *Journal of Geophysical Research: Solid Earth*, 88(B10):8226–8236.

Tong, P., Zhao, D., and Yang, D. (2011). Tomography of the 1995 Kobe earthquake area: comparison of finite-frequency and ray approaches. *Geophysical Journal International*, 187(1):278–302.

Tork Qashqai, M., Carlos Afonso, J., and Yang, Y. (2016). The crustal structure of the Arizona Transition Zone and southern Colorado Plateau from multiobservable probabilistic inversion. *Geochemistry, Geophysics, Geosystems*, 17(11):4308–4332.

Trampert, J. and Spetzler, J. (2006). Surface wave tomography: finite-frequency effects lost in the null space. *Geophysical Journal International*, 164(2):394–400.

Trampert, J. and Woodhouse, J. (1996). High resolution global phase velocity distributions. *Geophysical research letters*, 23(1):21–24.

Trampert, J. and Woodhouse, J. H. (1995). Global phase velocity maps of Love and Rayleigh waves between 40 and 150 seconds. *Geophysical Journal International*, 122(2):675–690.

Um, J. and Thurber, C. (1987). A fast algorithm for two-point seismic ray tracing. *Bulletin of the Seismological Society of America*, 77(3):972–986.

van der Hilst, R. D., Widiyantoro, S., and Engdahl, E. R. (1997). Evidence for deep mantle circulation from global tomography. *Nature*, 386:578.

van der Hist, R., Engdahl, R., Spakman, W., and Nolet, G. (1991). Tomographic imaging of subducted lithosphere below northwest Pacific island arcs. *Nature*, 353(6339):37–43.

Van der Voo, R., Spakman, W., and Bijwaard, H. (1999). Mesozoic subducted slabs under Siberia. *Nature*, 397(6716):246–249.

Van Manen, D.-J. (2006). *Time-reversal and Interferometry with applications to forward modeling of wave propagation and a chapter on receiver functions*. PhD thesis, University of Edinburgh.

van Mierlo, W. L., Langenhorst, F., Frost, D. J., and Rubie, D. C. (2013). Stagnation of subducting slabs in the transition zone due to slow diffusion in majoritic garnet. *Nature Geoscience*, 6:400.

Vandecar, J. C. and Crosson, R. S. (1990). Determination of teleseismic relative phase arrival times using multi-channel cross-correlation and least-squares. *Bulletin of the Seismological Society of America*, 80(1):150–169. Cl678 Times Cited:396 Cited References Count:20.

Villagómez, D. R., Toomey, D. R., Hooft, E. E., and Solomon, S. C. (2007). Upper mantle structure beneath the Galápagos Archipelago from surface wave tomography. *Journal of Geophysical Research: Solid Earth*, 112(B7).

Vinnik, L. P., Reigber, C., Aleshin, I. M., Kosarev, G. L., Kaban, M. K., Oreshin, S. I., and Roecker, S. W. (2004). Receiver function tomography of the central Tien Shan. *Earth and Planetary Science Letters*, 225(1-2):131–146.

von Blanckenburg, F. and Davies, J. H. (1995). Slab breakoff: A model for syncollisional magmatism and tectonics in the Alps. *Tectonics*, 14(1):120–131.

Wagner, L., Forsyth, D. W., Fouch, M. J., and James, D. E. (2010). Detailed three-dimensional shear wave velocity structure of the northwestern United States from Rayleigh wave tomography. *Earth and Planetary Science Letters*, 299(3):273–284.

Wang, T., Hong, D.-w., Jahn, B.-m., Tong, Y., Wang, Y.-b., Han, B.-f., and Wang, X.-x. (2006). Timing, petrogenesis, and setting of Paleozoic synorogenic intrusions from the Altai Mountains, Northwest China: implications for the tectonic evolution of an accretionary orogen. *The Journal of Geology*, 114(6):735–751.

Wang, Y., Forsyth, D. W., Rau, C. J., Carriero, N., Schmandt, B., Gaherty, J. B., and Savage, B. (2013). Fossil slabs attached to unsubducted fragments of the Farallon plate. *Proc Natl Acad Sci U S A*, 110(14):5342–6.

Wang, Y., Forsyth, D. W., and Savage, B. (2009). Convective upwelling in the mantle beneath the Gulf of California. *Nature*, 462(7272):499.

Wang, Z., Sun, S., Li, J., Hou, Q., Qin, K., Xiao, W., and Hao, J. (2003). Paleozoic tectonic evolution of the northern Xinjiang, China: Geochemical and geochronological constraints from the ophiolites. *Tectonics*, 22(2).

Wannamaker, P. E., Caldwell, T. G., Jiracek, G. R., Maris, V., Hill, G. J., Ogawa, Y., Bibby, H. M., Bennie, S. L., and Heise, W. (2009). Fluid and deformation regime of an advancing subduction system at Marlborough, New Zealand. *Nature*, 460(7256):733.

Wapenaar, K. and Fokkema, J. (2006). Green's function representations for seismic interferometry. *Geophysics*, 71(4):SI33–SI46.

Wapenaar, K., Fokkema, J., and Snieder, R. (2005). Retrieving the Green's function in an open system by cross correlation: A comparison of approaches (L). *The Journal of the Acoustical Society of America*, 118(5):2783–2786.

Watson, M. P., Hayward, A. B., Parkinson, D. N., and Zhang, Z. M. (1987). Plate tectonic history, basin development and petroleum source rock deposition onshore China. *Marine and Petroleum Geology*, 4(3):205–225.

Weaver, R. L. and Lobkis, O. I. (2001). Ultrasonics without a source: Thermal fluctuation correlations at MHz frequencies. *Physical Review Letters*, 87(13):134301.

Weaver, R. L. and Lobkis, O. I. (2004). Diffuse fields in open systems and the emergence of the Green's function (L). *The Journal of the Acoustical Society of America*, 116(5):2731–2734.

Weaver, R. L. and Lobkis, O. I. (2006). Diffuse fields in ultrasonics and seismology. *Geophysics*, 71(4):SI5–SI9.

Wielandt, E. (1993). Propagation and structural interpretation of non-plane waves. *Geophysical Journal International*, 113(1):45–53.

Windley, B., xa, F, Kr, xf, ner, A., Guo, J., Qu, G., Li, Y., and Zhang, C. (2002). Neoproterozoic to Paleozoic Geology of the Altai Orogen, NW China: New Zircon Age Data and Tectonic Evolution. *The Journal of Geology*, 110(6):719–737.

Windley, B. F., Alexeiev, D., Xiao, W., Kröner, A., and Badarch, G. (2007). Tectonic models for accretion of the Central Asian Orogenic Belt. *Journal of the Geological Society*, 164(1):31–47.

Windley, B. F. and Xiao, W. (2018). Ridge subduction and slab windows in the Central Asian Orogenic Belt: Tectonic implications for the evolution of an accretionary orogen. *Gondwana Research*, 61:73–87.

Woodhouse, J. H. and Dziewonski, A. M. (1984). Mapping the upper mantle: Three-imensional modeling of Earth structure by inversion of seismic waveforms. *Journal of Geophysical Research: Solid Earth*, 89(B7):5953–5986.

Wortel, M. J. R. and Spakman, W. (2000). Subduction and Slab Detachment in the Mediterranean-Carpathian Region. *Science*, 290:1910–1917.

Wu, S., Huang, R., Xu, Y., Yang, Y., Jiang, X., and Zhu, L. (2018). Seismological Evidence for a Remnant Oceanic Slab in the Western Junggar, Northwest China. *Journal of Geophysical Research-Solid Earth*, 123(5):4157–4170.

XBGMR (1993). Regional geology of xinjiang uygur autonomy region.

Xiang, K., Li, Y., XU, L., Zhang, H., and Tong, L. (2013). Discussing the Application of "Tailegula Formation" in Baogutu-Hatu Region, West Junggar, XinJiang. *Xinjiang Geology*, 31:148–152.

Xiao, W., Han, C., Yuan, C., Sun, M., Lin, S., Chen, H., Li, Z., Li, J., and Sun, S. (2008). Middle Cambrian to Permian subduction-related accretionary orogenesis of Northern Xinjiang, NW China: implications for the tectonic evolution of central Asia. *Journal of Asian Earth Sciences*, 32(2-4):102–117.

Xiao, W., Huang, B., Han, C., Sun, S., and Li, J. (2010). A review of the western part of the Altaids: A key to understanding the architecture of accretionary orogens. *Gondwana Research*, 18(2):253–273.

Xiao, W. and Santosh, M. (2014). The western Central Asian Orogenic Belt: A window to accretionary orogenesis and continental growth. *Gondwana Research*, 25(4):1429–1444.

Xiao, W., Sun, M., and Santosh, M. (2015a). Continental reconstruction and metallogeny of the Circum-Junggar areas and termination of the southern Central Asian Orogenic Belt. *Geoscience Frontiers*, 6(2):137–140.

Xiao, W., Windley, B. F., Sun, S., Li, J., Huang, B., Han, C., Yuan, C., Sun, M., and Chen, H. (2015b). A Tale of Amalgamation of Three Permo-Triassic Collage Systems in Central Asia: Oroclines, Sutures, and Terminal Accretion. *Annual Review of Earth and Planetary Sciences*, 43:477–507.

Xiao, W. J., Windley, B. F., Huang, B. C., Han, C. M., Yuan, C., Chen, H. L., Sun, M., Sun, S., and Li, J. L. (2009). End-Permian to mid-Triassic termination of the accretionary processes of the southern Altaids: implications for the geodynamic evolution, Phanerozoic continental growth, and metallogeny of Central Asia. *International Journal of Earth Sciences*, 98(6):1189–1217.

Xu, S., Zheng, G., Zheng, J., Zhou, S., and Shi, P. (2017). Mantle-derived helium in foreland basins in Xinjiang, Northwest China. *Tectonophysics*, 694:319–331.

Xu, X., He, G., Li, H., Ding, T., Liu, X., and Mei, S. (2006). Basic characteristics of the Karamay ophiolitic mélange, Xinjiang, and its zircon SHRIMP dating. *Geology in China*, 33(3):470–475.

Xu, Y., Yang, B., Zhang, S., Liu, Y., Zhu, L., Huang, R., Chen, C., Li, Y., and Luo, Y. (2016). Magnetotelluric imaging of a fossil paleozoic intraoceanic subduction zone in western Junggar, NW China. *Journal of Geophysical Research: Solid Earth*, 121(6):4103–4117.

Yakubchuk, A. (2002). The Baikalide-Altaid, Transbaikal-Mongolian and North Pacific orogenic collages: similarity and diversity of structural patterns and metallogenic zoning. *Geological Society, London, Special Publications*, 204(1):273–297.

Yakubchuk, A. (2004). Architecture and mineral deposit settings of the Altaid orogenic collage: a revised model. *Journal of Asian Earth Sciences*, 23(5):761–779.

Yamanaka, Y. and Kikuchi, M. (2004). Asperity map along the subduction zone in northeastern Japan inferred from regional seismic data. *Journal of Geophysical Research: Solid Earth*, 109(B7).

Yan, W., Wang, G., Li, L., Zhang, L., Yu, J., Yang, G., and Chen, X. (2015). Deformation analyses and their geological implications of Carboniferous-Permian tectonic transformation period in northwest margin of Junggar basin. *Diqiu Kexue-Zhongguo Dizhi Daxue Xuebao/Earth Science-Journal of China University of Geosciences*, 40(3):504–520.

Yang, G., Li, Y., Gu, P., Yang, B., Tong, L., and Zhang, H. (2012a). Geochronological and geochemical study of the Darbut Ophiolitic Complex in the West Junggar (NW China): implications for petrogenesis and tectonic evolution. *Gondwana Research*, 21(4):1037–1049.

Yang, G., Li, Y., Santosh, M., Yang, B., Yan, J., Zhang, B., and Tong, L. (2012b). Geochronology and geochemistry of basaltic rocks from the Sartuohai ophiolitic mélange, NW China: Implications for a Devonian mantle plume within the Junggar Ocean. *Journal of Asian Earth Sciences*, 59:141–155.

Yang, T., Shen, Y., van der Lee, S., Solomon, S. C., and Hung, S.-H. (2006). Upper mantle structure beneath the Azores hotspot from finite-frequency seismic tomography. *Earth and Planetary Science Letters*, 250(1-2):11–26.

Yang, X.-F., He, D.-F., Wang, Q.-C., and Tang, Y. (2012c). Tectonostratigraphic evolution of the Carboniferous arc-related basin in the East Junggar Basin, northwest China: Insights into its link with the subduction process. *Gondwana Research*, 22(3):1030–1046.

Yang, Y. and Forsyth, D. W. (2006a). Rayleigh wave phase velocities, small-scale convection, and azimuthal anisotropy beneath southern California. *Journal of Geophysical Research: Solid Earth*, 111.

Yang, Y. and Forsyth, D. W. (2006b). Regional tomographic inversion of the amplitude and phase of Rayleigh waves with 2-D sensitivity kernels. *Geophysical Journal International*, 166:1148–1160.

Yang, Y., Li, A., and Ritzwoller, M. H. (2008). Crustal and uppermost mantle structure in southern africa revealed from ambient noise and teleseismic tomography. *Geophysical Journal International*, 174:235–248.

Yang, Y., Ritzwoller, M. H., and Jones, C. H. (2011a). Crustal structure determined from ambient noise tomography near the magmatic centers of the Coso region, southeastern California. *Geochemistry, Geophysics, Geosystems*, 12:1–20.

Yang, Y., Ritzwoller, M. H., Levshin, A. L., and Shapiro, N. M. (2007). Ambient noise Rayleigh wave tomography across Europe. *Geophysical Journal International*, 168:259–274.

Yang, Y., Shen, W., and Ritzwoller, M. H. (2011b). Surface wave tomography on a large-scale seismic array combining ambient noise and teleseismic earthquake data. *Earthquake Science*, 24(1):55–64.

Yao, H., Beghein, C., and Van Der Hilst, R. D. (2008). Surface wave array tomography in SE Tibet from ambient seismic noise and two-station analysis - II. Crustal and upper-mantle structure. *Geophysical Journal International*, 173(1):205–219.

Yao, H., van Der Hilst, R. D., and De Hoop, M. V. (2006). Surface-wave array tomography in SE Tibet from ambient seismic noise and two-station analysis-I. Phase velocity maps. *Geophysical Journal International*, 166(2):732–744.

Yao, H., Xu, G., Zhu, L., and Xiao, X. (2005). Mantle structure from inter-station Rayleigh wave dispersion and its tectonic implication in western China and neighboring regions. *Physics of the Earth and Planetary Interiors*, 148(1):39–54.

Yin, J., Chen, W., Xiao, W., Yuan, C., Sun, M., Tang, G., Yu, S., Long, X., Cai, K., Geng, H., Zhang, Y., and Liu, X. (2015). Petrogenesis of Early-Permian sanukitoids from West Junggar, Northwest China: Implications for Late Paleozoic crustal growth in Central Asia. *Tectonophysics*, 662:385–397.

Yin, J., Long, X., Yuan, C., Sun, M., Zhao, G., and Geng, H. (2013). A Late Carboniferous–Early Permian slab window in the West Junggar of NW China: Geochronological and geochemical evidence from mafic to intermediate dikes. *Lithos*, 175:146–162.

Yin, J., Yuan, C., Sun, M., Long, X., Zhao, G., Wong, K. P., Geng, H., and Cai, K. (2010). Late Carboniferous high-Mg dioritic dikes in Western Junggar, NW China: Geochemical features, petrogenesis and tectonic implications. *Gondwana Research*, 17:145–152.

Yu, X., Yang, S.-F., Chen, H.-L., Chen, Z.-Q., Li, Z.-L., Batt, G. E., and Li, Y.-Q. (2011). Permian flood basalts from the Tarim Basin, Northwest China: SHRIMP zircon U–Pb dating and geochemical characteristics. *Gondwana Research*, 20(2-3):485–497.

Yuan, C., Sun, M., Xiao, W., Li, X., Chen, H., Lin, S., Xia, X., and Long, X. (2007). Accretionary orogenesis of the Chinese Altai: Insights from Paleozoic granitoids. *Chemical Geology*, 242(1):22–39.

Zhang, C. and Huang, X. (1992). The ages and tectonic settings of ophiolites in West Junggar, Xinjiang. *Geological review*, 38(6):509–524.

Zhang, C.-L., Li, Z.-X., Li, X.-H., Xu, Y.-G., Zhou, G., and Ye, H.-M. (2010). A Permian large igneous province in Tarim and Central Asian orogenic belt, NW China: Results of a ca. 275 Ma mantle plume? *Bulletin*, 122(11-12):2020–2040.

Zhang, H., Thurber, C. H., Shelly, D., Ide, S., Beroza, G. C., and Hasegawa, A. (2004). High-resolution subducting-slab structure beneath northern Honshu, Japan, revealed by double-difference tomography. *Geology*, 32(4):361–364.

Zhang, J. and Toksöz, M. (1998). Nonlinear refraction traveltime tomography. *GEOPHYSICS*, 63(5):1726–1737.

Zhang, J., Xiao, W., Han, C., Ao, S., Yuan, C., Sun, M., Geng, H., Zhao, G., Guo, Q., and Ma, C. (2011a). Kinematics and age constraints of deformation in a Late Carboniferous accretionary complex in Western Junggar, NW China. *Gondwana Research*, 19(4):958–974.

Zhang, J., Xiao, W., Han, C., Mao, Q., Ao, S., Guo, Q., and Ma, C. (2011b). A Devonian to Carboniferous intra-oceanic subduction system in Western Junggar, NW China. *Lithos*, 125(1-2):592–606.

Zhang, S., Xu, Y., Jiang, L., Yang, B., Liu, Y., Griffin, W., Luo, Y., Huang, R., Zhou, Y., and Zhang, L. (2017). Electrical structures in the northwest margin of the Junggar basin: Implications for its late Paleozoic geodynamics. *Tectonophysics*, 717:473–483.

Zhang, Z. M., Liou, J. G., and Coleman, R. G. (1984). An Outline of the Plate-Tectonics of China. *Geological Society of America Bulletin*, 95(3):295–312.

Zhao, D. (2004). Global tomographic images of mantle plumes and subducting slabs: insight into deep Earth dynamics. *Physics of the Earth and Planetary Interiors*, 146(1-2):3–34.

Zhao, D., Hasegawa, A., and Horiuchi, S. (1992). Tomographic imaging of P and S wave velocity structure beneath northeastern Japan. *Journal of Geophysical Research: Solid Earth*, 97(B13):19909–19928.

Zhao, D., Tian, Y., Lei, J., Liu, L., and Zheng, S. (2009). Seismic image and origin of the Changbai intraplate volcano in East Asia: role of big mantle wedge above the stagnant Pacific slab. *Physics of the Earth and Planetary Interiors*, 173(3-4):197–206.

Zhao, J., Liu, G., Lu, Z., Zhang, X., and Zhao, G. (2003). Lithospheric structure and dynamic processes of the Tianshan orogenic belt and the Junggar basin. *Tectonophysics*, 376(3-4):199–239.

Zheng, J., Sun, M., Zhao, G., Robinson, P. T., and Wang, F. (2007). Elemental and Sr-Nd-Pb isotopic geochemistry of Late Paleozoic volcanic rocks beneath the Junggar basin, NW China: Implications for the formation and evolution of the basin basement. *Journal of Asian Earth Sciences*, 29(5-6):778–794.

Zheng, S., Sun, X., Song, X., Yang, Y., and Ritzwoller, M. H. (2008). Surface wave tomography of China from ambient seismic noise correlation. *Geochemistry, Geophysics, Geosystems*, 9(5).

Zhou, Y., Dahlen, F., and Nolet, G. (2004). Three-dimensional sensitivity kernels for surface wave observables. *Geophysical Journal International*, 158(1):142–168.

Zhou, Y., Nolet, G., Dahlen, F., and Laske, G. (2006). Global upper-mantle structure from finite-frequency surface-wave tomography. *Journal of Geophysical Research: Solid Earth*, 111(B4).

Zhu, L. (2000). Crustal structure across the San Andreas Fault, southern California from teleseismic converted waves. *Earth and Planetary Science Letters*, 179(1):183–190.

Zhu, L. and Kanamori, H. (2000). Moho depth variation in southern California from teleseismic receiver functions. *Journal of Geophysical Research: Solid Earth*, 105(B2):2969–2980.